

TAILORING THE BENDING STIFFNESS OF ELASTOMERIC DUAL-MATRIX  
COMPOSITES

by

David Lewis Platt

A thesis submitted in conformity with the requirements  
for the degree of Master of Applied Science  
Graduate Department of Aerospace Science and Engineering  
University of Toronto

© Copyright 2016 by David Lewis Platt

# Abstract

Tailoring the Bending Stiffness of Elastomeric Dual-Matrix Composites

David Lewis Platt

Master of Applied Science

Graduate Department of Aerospace Science and Engineering

University of Toronto

2016

Aircraft structural design is becoming increasingly oriented towards multifunctional structures, which are capable of supporting large loads while exhibiting additional functional capabilities; morphing is an example. Composite materials, which are highly prevalent in aircraft today, provide the perfect testbed for such morphing technologies. Dual-matrix composites are being investigated by a number of researchers, with the primary application being deployable structures in space. This work investigates a more load-intensive application in aircraft cabin interiors. A morphing composite meal-tray table prototype is fabricated and tested. The macromechanics of dual-matrix laminates are investigated, with the focus being the tailoring of the bending stiffness of such laminates. The cross-section anticlastic deflections of  $\pm 45^\circ$  layups, due to Poisson ratios close to unity, are shown to increase the bending stiffness of the laminate, resulting from an increased second moment of area. A predictive model for bending stiffness is constructed, compared with FEA and experiments, and its limitations in predicting woven-fabric composite behaviour are discussed.

## Acknowledgements

To my God and Saviour, Jesus Christ, I owe this all. You are my rock and my refuge, and only through your strength have I been able to achieve this. To you be all the glory and majesty forever.

I give my sincerest gratitude to Professor Craig Steeves, who has provided unending assistance in the research process. He has provided the ideal platform in which to conduct my research, giving enough freedom to allow me to take control of the project while providing invaluable guidance and support to help me along in my work.

I dedicate this work to my Mom, Margie, and my Dad, Barry. Without their copious emotional and financial support, I would not have been able to make it through this challenging stage of my life. Thank you for believing in me and supporting me in numerous ways to accomplish another one of my dreams.

A big thank you to Bombardier Aerospace for funding this research and their valuable input during the design process, and to Prof Jeff Xi of Ryerson University for coordinating the overall project.

Last, but not least, I pay tribute to my fellow colleagues and friends in the Advanced Aerospace Structures group as well as other UTIAS friends, who have not only provided help when I've needed it but also for their warm friendship, and for making my time at UTIAS incredibly enjoyable.

# Contents

<b>1</b>	<b>Introduction</b>	<b>1</b>
1.1	Motivation . . . . .	1
1.2	Thesis Outline . . . . .	2
<b>2</b>	<b>Literature Review</b>	<b>3</b>
2.1	Morphing Skins . . . . .	4
2.2	Stiffness Tailoring of Composites . . . . .	5
2.2.1	Stiffness Tailoring Using Underlying Structures . . . . .	5
2.2.2	Stiffness Tailoring of Composites by Multistability . . . . .	6
2.2.3	Flexible Matrix Composites . . . . .	9
2.2.4	Dual-Matrix Composites . . . . .	10
2.2.5	Fibre Tow Steering . . . . .	11
2.3	Anticlastic Effects in Beams Subjected to Bending . . . . .	13
2.3.1	Anticlastic Curvature Modelling . . . . .	13
2.3.2	Neutral Axis Definition . . . . .	14
<b>3</b>	<b>Manufacturing Process and Material Characterization</b>	<b>15</b>
3.1	Material Selection . . . . .	15
3.2	Dual-Matrix Fabrication . . . . .	16
3.2.1	Method . . . . .	16
3.2.2	Micrographs . . . . .	17
3.3	Composite Mechanical Properties . . . . .	17
3.3.1	Polyurethane Elastomer . . . . .	18
3.3.2	Carbon Fibre/Epoxy Laminate . . . . .	20
3.3.3	Carbon Fibre/Elastomer Laminate . . . . .	23
3.3.4	Laminate Density and Fibre Volume Fraction . . . . .	28
3.3.5	Abaqus Material Characterization . . . . .	28
<b>4</b>	<b>Anticlastic Bending</b>	<b>30</b>
4.1	Anticlastic Effects in Laminated Composite Beams . . . . .	30
4.1.1	Anticlastic Bending Governing Equation . . . . .	30
4.1.2	Model Verification . . . . .	32
4.1.3	Preliminary Experimental Investigation . . . . .	33
4.2	Finite Element Model . . . . .	38



4.2.1	Overview . . . . .	38
4.2.2	Boundary Conditions and Applied Loads . . . . .	38
4.2.3	Mesh Convergence and Element Selection . . . . .	38
4.2.4	Abaqus Limitations . . . . .	41
4.3	Increase in Bending Stiffness Due to Anticlastic Effects . . . . .	42
4.3.1	Bending Moment . . . . .	42
4.3.2	Shift of the Cross Section Neutral Axis . . . . .	44
4.3.3	Determination of the Second Moment of Area . . . . .	47
4.3.4	Bending Moment Verification and Increase in Bending Stiffness . . . . .	48
4.3.5	Effects on Bending Stiffness Due to Dual-Matrix Interaction . . . . .	49
4.4	Experiments . . . . .	55
4.4.1	Experimental Setup . . . . .	55
4.4.2	Results and Discussion . . . . .	57
4.4.3	Fibre Tow Buckling . . . . .	62
4.5	Large Deflection Modelling of a Beam . . . . .	64
4.5.1	Introduction . . . . .	64
4.5.2	Derivation of the Large Deflection Governing Equation . . . . .	64
4.5.3	Determination of the Beam Deflection . . . . .	65
4.5.4	Large Deflection Modelling of a Beam with Flexible Regions . . . . .	66
4.5.5	Model Verification . . . . .	67
4.5.6	Incorporating the Anticlastic Bending Model . . . . .	67
<b>5</b>	<b>Applications</b>	<b>69</b>
5.1	Composite Meal-Tray Table . . . . .	69
5.1.1	Design and Analysis . . . . .	69
5.1.2	Prototype Fabrication . . . . .	73
5.1.3	Prototype Testing . . . . .	74
5.2	Alternate Applications . . . . .	75
<b>6</b>	<b>Conclusions</b>	<b>78</b>
6.1	Recommendations . . . . .	80
	<b>Bibliography</b>	<b>80</b>
	<b>Appendices</b>	<b>84</b>
	<b>A Fourth-Order Runge-Kutta Numerical Integration</b>	<b>85</b>
	<b>B Test Apparatus Specifications</b>	<b>87</b>

# List of Tables

3.1	Measured material properties . . . . .	18
3.2	Reduction in measured Poisson ratio of an elastomer with surface adhesive of varying thickness . . . . .	20
4.1	Lamina material properties for theoretical model comparison with FE . . . . .	33
4.2	Convergence study details and simulation run times. . . . .	41
4.3	Material specifications of carbon fibre, elastomer, and lamina with a fibre volume fraction of 0.5 . . . . .	48
4.4	Dual-matrix interaction effects for different laminates . . . . .	50
4.5	Beam cross section and material properties for Abaqus verification of large-deflection beam model. . . . .	68
5.1	Section and material properties for large deflection modelling of the tray table prototype. . . . .	71

# List of Figures

2.1	Morphing aircraft designs through the years . . . . .	4
2.2	FlexSys Inc.’s FlexFoil morphing flap concept. The flap can achieve large deflections and support large aerodynamic loads. The internal structure depicted here is from the patent, and therefore not the final design. . . . .	5
2.3	Morphing kagome structure . . . . .	6
2.4	Multistable composite structures . . . . .	7
2.5	Multistable composite laminates . . . . .	8
2.6	$\pm 75^\circ$ flexible matrix composite out of-plane deflections for an applied pressure load . . . .	10
2.7	Folding Miura-ori structures using dual-matrix composites . . . . .	11
2.8	Bistable morphing flap using variable angle tows . . . . .	12
2.9	Anticlastic effect in a beam due to an applied moment . . . . .	14
3.1	Micrographs of dual-matrix composite layup . . . . .	18
3.2	Experimental apparatus for material characterization. . . . .	19
3.3	Laminate test samples for material property characterization . . . . .	19
3.4	Tensile testing data for Freeman 1040 polyurethane elastomer for the characterization of the stiffness and Poisson ratio. . . . .	21
3.5	FE model showing reduction in strain of an elastomer due to an adhesive on its surface. .	22
3.6	Tensile testing data for $[(0/90F)_4]$ carbon fibre/epoxy for the characterization of the stiffness and Poisson ratio. . . . .	24
3.7	Tensile testing data for $[(\pm 45F)_4]$ carbon fibre/epoxy for the characterization of the stiffness and Poisson ratio. . . . .	25
3.8	Compressive stress-strain results for carbon fibre/epoxy for two different layups. . . . .	26
3.9	Tensile stress-strain results for carbon fibre/elastomer laminates of two different layups. .	27
4.1	Schematic of the anticlastic deflection of the laminate cross-section . . . . .	31
4.2	Normalized anticlastic deflection for increasing longitudinal curvature for a 1 mm thick $[\pm 45]_S$ carbon-fibre reinforced epoxy laminate. . . . .	34
4.3	Normalized anticlastic deflection for increasing longitudinal curvature for a 1 mm thick $[\pm 45]_S$ carbon-fibre reinforced elastomer laminate. . . . .	35
4.4	Dual-matrix laminate showing the elastomeric resin boundaries . . . . .	36
4.5	Bending stiffness comparison between narrow and wide dual-matrix laminates . . . . .	36
4.6	Bending stiffness comparison between a 10 mm wide dual-matrix laminate and a 20 mm wide laminate with a slit along its centre line . . . . .	37

4.7	Anticlastic effect clearly demonstrated for large curvature in a 20 mm wide dual-matrix laminate with a slit. . . . .	37
4.8	Zero-rotation boundary condition ( $UR2 = 0$ ) applied to the edge at which the anticlastic deflections are extracted . . . . .	39
4.9	Fixed boundary condition applied to the centre node on the opposite edge of the laminate	39
4.10	Applied rotation ( $UR2$ ) to right-hand edge to induce a constant curvature in the laminate	40
4.11	Mesh convergence for reaction and section internal moment for shell elements with full integration (S4) and reduced (S4R) integration . . . . .	40
4.12	Abaqus output for through-thickness logarithmic strains of a $[(\pm 45)_2]_S$ elastomeric laminate	43
4.13	Neutral axis comparison between Abaqus (plane of zero strain) and the model (geometric neutral axis) for 50 mm and 120 mm wide $[(\pm 45)_2]_S$ laminates. . . . .	45
4.14	Comparison of neutral axis location for increasing longitudinal curvature for 50 mm and 120 mm wide $[(\pm 45)_2]_S$ laminates . . . . .	46
4.15	Elemental area for an arbitrary cross section for determination of the second moment of area. . . . .	48
4.16	Applied bending moment required for increasing longitudinal curvature of a 30 mm wide, 2.1 mm thick laminate, with a $[(\pm 45)_2]_S$ layup. . . . .	51
4.17	Applied bending moment required for increasing longitudinal curvature of a 50 mm wide, 2.1 mm thick laminate, with a $[(\pm 45)_2]_S$ layup. . . . .	51
4.18	Applied bending moment required for increasing longitudinal curvature of a 120 mm wide, 2.1 mm thick laminate, with a $[(\pm 45)_2]_S$ layup. . . . .	52
4.19	Applied bending moment required for increasing longitudinal curvature of a 10 mm wide, 1 mm thick laminate, with a $[\pm 45]_S$ layup. . . . .	52
4.20	Applied bending moment required for increasing longitudinal curvature of a 20 mm wide, 1 mm thick laminate, with a $[\pm 45]_S$ layup. . . . .	53
4.21	Applied bending moment required for increasing longitudinal curvature of a 40 mm wide, 1 mm thick laminate, with a $[\pm 45]_S$ layup. . . . .	53
4.22	Normalized bending stiffness for increasing longitudinal curvature for 1 mm thick, $[\pm 45]_S$ laminates of different widths . . . . .	54
4.23	Normalized bending stiffness for increasing longitudinal curvature for 2.1 mm thick, $[(\pm 45)_2]_S$ laminates of different widths . . . . .	54
4.24	Experimental setup for four-point bending tests of elastomeric laminates . . . . .	56
4.25	Schematic showing the loading on the test sample during experiments . . . . .	56
4.26	Anticlastic curvature comparison between analytical model and experimental data for narrow laminates. The centreline is the longitudinal line running down the centre of the length of the laminate. . . . .	58
4.27	Anticlastic curvature comparison between analytical model and experimental data for wider laminates . . . . .	59
4.28	Bending moment for increasing longitudinal curvature for narrow laminates with $[(\pm 45F)_8]$ layup . . . . .	60
4.29	Bending moment for increasing longitudinal curvature for wide laminates with $[(\pm 45F)_8]$ layup . . . . .	61
4.30	Fibre-tow buckling of a $[(0/90F)_8]$ elastomeric laminate. . . . .	63

4.31	Straight cantilevered beam with an inclined follower load undergoing large deflection . . .	64
4.32	CAD representation of a dual-matrix laminate with three elastomeric matrix regions . . .	66
4.33	Large-deflection beam model verification using Abaqus FEA . . . . .	68
5.1	Bombardier conceptual drawing of morphing composite tray table . . . . .	70
5.2	Tray table prototype predicted deflection under its own weight . . . . .	71
5.3	Various mechanical stop concepts to prevent deflection of the tray table beyond the horizontal . . . . .	72
5.4	Free body diagram for sliding mechanical stop . . . . .	73
5.5	Vacuum bag curing of epoxy regions of the double hinge. The elastomer regions are previously cured using the same procedure. . . . .	74
5.6	Final tray table fabrication process, incorporating the hinges into the overall structure. The laminate is initially over-sized so that the final cutting can be done more accurately. . . . .	75
5.7	Layup of the overlap section . . . . .	76
5.8	Tray table final prototype assembly with 1 kg weight as a demonstration. . . . .	76
5.9	Prototype double hinge showing three slits in upper hinge and 1 slit in lower hinge for stiffness tailoring . . . . .	77
B.1	MTS 880 Material Test System calibration details . . . . .	87
B.2	Electronic Instrument Research LE-05 laser extensometer details . . . . .	87
B.3	Wyoming Test Fixtures Inc. compression test fixture details . . . . .	87

# Chapter 1

## Introduction

### 1.1 Motivation

Aviation has been at the forefront of technological advance for decades, with aerospace developments subsequently filtering into numerous other industries. Global aviation accounts for 12% of carbon dioxide emissions from transportation, and 2% of all human-induced carbon dioxide emissions [17]. Therefore, the demand for sustainable aviation is ever increasing, and as a result, mounting pressure is being placed on aircraft companies to develop innovative technologies that reduce the carbon footprint of aviation. Typically, the primary focus is on engine efficiency, given that engines are directly emitting harmful substances into the atmosphere. However, there is a myriad of other factors which also influence the efficiency of an aircraft, one of which is the structural weight. A reduction in an aircraft's weight improves its efficiency, prior to any changes made to the engine. Of course, the combined improvements in all aspects of the aircraft's design produce the greatest advancements in achieving sustainable aviation.

There are a number of ways to reduce the structural weight of an aircraft. Currently, the most prevalent design method is to use alternative materials, specifically fibre composites, which exhibit superior strength- and stiffness-to-weight properties. Previously, the manufacturing challenges surrounding composite materials made them a high-risk alternative as well as expensive compared to metals. However, the advancement of manufacturing techniques has allowed the industry to expediently produce reliable components at a relatively low cost. As a result, many new aircraft designs that are coming to fruition make substantial use of composites, specific examples of this being the Boeing 787 and Airbus A350, which have 50% [6] and 53% [2] composites by empty weight respectively. Composites also have superior design flexibility compared to most materials, allowing for stiffness tailoring through customization of the primary constituents (i.e. the fibres and matrix).

A combination of the transition to composite materials and the desire for morphing has resulted in recent research into morphing composites. The objective is to design a lightweight structure that is capable of achieving a desired shape change. There are various methods that are investigated by researchers, which are discussed in Chapter-2. This thesis investigates one particular method, which is dual-matrix composite structures, and certain phenomena associated with the morphing of such composites.

The benefit of morphing is the development of multi-functional structures comprised of fewer and smaller components than current designs. The structure itself achieves large deformations without compromising its load-carrying capability. This is a tremendously difficult design requirement, particularly

in the case of morphing skins (see Section-2.1). In addition, aircraft skins are required to be impervious, prohibiting the use of cut-outs to facilitate these deformations. Despite the many challenges, the aerospace industry is hopeful that morphing structures will offer a solution to the demand for reduced weight, aerodynamically improved surfaces, and reduced noise.

## 1.2 Thesis Outline

The objective of this work is to investigate the morphing of dual-matrix fibre composites, by means of stiffness tailoring. Research has been conducted previously by a number of authors who have investigated the use of flexible resin material in place of epoxy resin, which is more commonly used in conventional laminates. Chapter-2 discusses this research in more detail and also delves into the literature pertinent to it. Other forms of stiffness tailoring are also presented in order to provide sufficient background to this work. The principles of anticlastic bending are also introduced to build a foundation for later chapters which explore the application of the anticlastic theory.

Chapter-3 discusses the manufacturing process of a dual-matrix laminate, including material selection. Various experimental results for different laminate layup configurations and resin materials are presented, and the mechanical properties thereof are determined. Due to the large number of variables in the composite fabrication process, it is essential to determine the properties experimentally as opposed to relying on the theoretical predictions of classical lamination theory, especially given the novelty of using a high-strain compliant elastomeric resin.

The mechanical properties are then used in the investigation of the anticlastic curvature due to Poisson effects. Chapter-4 presents the governing equations and theoretical model of the anticlastic phenomenon in composites, with verification using Abaqus finite element analysis (FEA) software. The increase in the bending stiffness of composite laminates, due to anticlastic effects, is investigated. A minor shift in the cross-section neutral axis is observed and further investigated. Experimental validation is attempted using woven-fabric elastomeric composites. The results are presented in Section-4.4, showing that the analytical model does not provide accurate results, since it assumes unidirectional lamina.

This research is applied to a morphing composite meal-tray table for Bombardier Aerospace commercial aircraft. The design, analysis and manufacture of the prototype is detailed in Chapter-5. Some other applications are briefly discussed for possible future development.

Finally, Chapter-6 concludes this work and provides recommendations for future development of the dual-matrix technology for morphing applications.

## Chapter 2

# Literature Review

There has been a significant increase in the research of morphing structures in the last few years, yet the concept of morphing structures in aerospace is not novel. The 1903 Wright Flyer, for example, used twist morphing for roll control [5]; this was relatively easy to achieve because of the flexibility of the wings, which were made of wood and fabric. Due to the combination of increasing safety demands and more structurally demanding roles for aircraft, subsequent designs had much greater stiffness and therefore less freedom to morph. Consequently, some of the first designs of morphing aircraft typically utilized heavy mechanical systems to achieve a desired configuration change of the aircraft with little deformation of the structural components themselves. These designs certainly achieved their intended purpose by providing beneficial morphing characteristics; however, more recent designs have shown a move toward lighter systems resulting from the morphing of materials and structures. Figure-2.1 shows a timeline of various morphing designs in aviation, each design morphing one or more of the geometric parameters of the aircraft. It can be seen here that prior to 1985, almost all the designs achieved large changes in geometry by mechanical morphing mechanisms, but the introduction of the Mission Adaptive Wing (MAW) on NASA's F-111 testbed demonstrated the potential for relatively small geometric changes (camber in this instance) including deformation of the outer structure, that is, the skin. Since then, research in this field has been primarily focused on the challenge of designing a structure and skin combination which is stiff enough for effective load carrying yet compliant enough to allow for deformation. Subsequent sections of this chapter discuss the various techniques that researchers have investigated in order to tackle this problem.

The most recent development in this field is the morphing of high-lift devices. The benefits of flap morphing (or more generally, camber morphing) are lighter structures, improved aerodynamics, and reduced noise emission, all of which subsequently yield an improved fuel efficiency. As of 2015, camber morphing is much closer to reaching commercial insertion with NASA flight testing a morphing flap concept known as FlexFoil. Srihar Kota, the founder of FlexSys, Inc. and chief designer of the flap, claims that the flap is able to support up to 430% of the design limit load [33]. The flap is thus over-designed, resulting in a structure that is heavier than necessary. Therefore, optimization of the design will most likely achieve a significant weight saving compared to a conventional flap. Figure-2.2 shows a demonstration of the flap as well as the internal structure; the structure depicted here is from the patent and is thus not the final design.






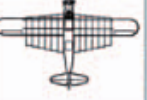




















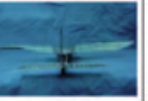



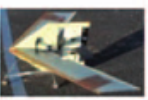
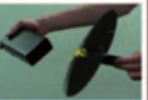


1903	1931	1931	1932	1937	1947	1951
						
Wright Flyer <i>Twist</i>	Pterodactyl IV <i>Sweep</i>	MAK-10 <i>Span</i>	IS-1 <i>Bi-to monoplane</i>	LIG-7 <i>Chord</i>	MAK-123 <i>Span</i>	X 5 <i>Sweep</i>
1952	1964	1964	1966	1967	1967	1969
						
XF10F <i>Sweep</i>	F 111 <i>Sweep</i>	XB 70 <i>Span bending</i>	Su 17 IG <i>Sweep</i>	MIG 23 <i>Sweep</i>	SU 24 <i>Sweep</i>	Tu 22 M <i>Sweep</i>
1970	1972	1974	1974	1979	1981	1985
						
F 14 <i>Sweep</i>	FS 29 <i>Span</i>	B 1 <i>Sweep</i>	Tornado <i>Sweep</i>	AD 1 <i>Obliquing</i>	Tu 160 <i>Sweep</i>	AFTI/F 111 <i>M.A.W.</i>
1993	1994	2001	2002	2003	2004	2005
						
FLYRT <i>Span</i>	MOTHRA <i>Camber</i>	AAL <i>Pitch</i>	F/A 18 <i>A.A.W.</i>	Virginia Tech <i>Span</i>	Univ. of Florida <i>Twist</i>	Univ. of Florida <i>Gull</i>
2006	2006	2007	2007	2007	2008	2010
						
MFX 1 <i>Sweep &amp; Span</i>	Univ. of Florida <i>Sweep</i>	Virginia Tech <i>Camber</i>	Univ. of Florida <i>Folding</i>	MFX 2 <i>Sweep &amp; span</i>	Delft Univ. <i>Sweep</i>	Virignia tech <i>Camber</i>

Figure 2.1: Morphing aircraft designs through the years, showing different techniques for achieving specific types of morphing [5].

## 2.1 Morphing Skins

The most challenging design requirement of a morphing structure is a skin that exhibits both in-plane compliance and out-of-plane stiffness. There has been significant research in the development of skins suitable for morphing applications as highlighted by Thill *et al.* [41]. The design of a particular morphing skin will be determined by the desired mode of morphing. For instance, an area change of the skin requires it to be stretched, but typical aerospace materials such as aluminum are extremely stiff and exhibit positive Poisson ratios. Alternate solutions include elastomeric materials, auxetic materials, and composites.

Elastomers, such as silicone rubber, are materials capable of relatively large elastic strains (in excess

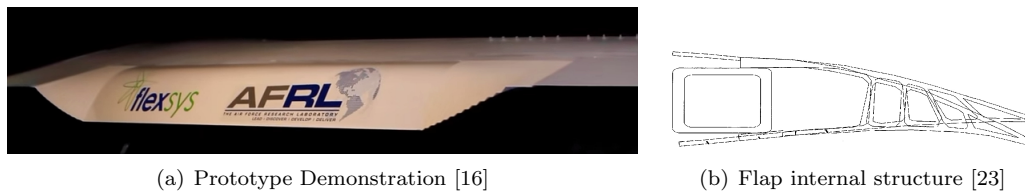


Figure 2.2: FlexSys Inc.'s FlexFoil morphing flap concept. The flap can achieve large deflections and support large aerodynamic loads. The internal structure depicted here is from the patent, and therefore not the final design.

of 400%) with high Poisson ratios, but they are not ideal for load carrying due to their high compliance. This gives rise to the design of elastomeric composites, which are particularly relevant to this work and are discussed in more detail in Section-2.2.3 and Section-2.2.4.

Auxetic materials are characterized by their negative Poisson ratio (i.e. stretching results in a perpendicular expansion). Alderson *et al.* [3] demonstrate two different designs of auxetic composites. The first design uses a unique laminate layup of ordinary unidirectional carbon epoxy prepreg. However, the auxetic effect is observed in the through-thickness direction which does not prove useful in preserving the width of a composite laminate when it undergoes axial deformation. The second design uses auxetic fibres in an epoxy resin. These fibres are useful for preventing fibre pullout since they are self-locking due to their expansion when the laminate is stretched. This is not so relevant to bending applications where fibre pullout is less likely to occur.

Composites with a Poisson ratio of zero (known as zero- $\nu$  composites) have also been considered. For example, some honeycomb cores consist of two mechanisms within the core, each having Poisson ratios of opposite sign. As a result, the hybrid core exhibits an overall zero Poisson ratio [34]. Furthermore, this design features high out-of-plane stiffness as with uniform honeycomb structures [41]. The Poisson effect in composites poses some challenges as well as benefits which are discussed in Chapter-4.

## 2.2 Stiffness Tailoring of Composites

Stiffness tailoring is innate to the design of composite materials. Composite laminate layups in general have in-plane stiffness tailoring, that is, the fibre orientation is designed to achieve desired mechanical properties in a particular direction. The stiffness tailoring of interest in this work is that of out-of-plane compared to in-plane stiffness. There are two opposing reasons for this, the first of which is that external aircraft structural components are subjected to large out-of-plane aerodynamic loads while in-plane deformation is desired. Secondly, certain morphing applications require low out-of-plane stiffness as with bending, but they still need to resist in-plane loads. The following sections present the literature pertaining to techniques for stiffness tailoring of composites including the use of underlying structures as well as unaided laminates.

### 2.2.1 Stiffness Tailoring Using Underlying Structures

One way to tailor the stiffness of a structure is by designing an underlying structure to which a compliant skin attaches. The structure provides out-of-plane stiffness and in-plane compliance while the skin is flexible enough to deform yet provide a smooth aerodynamic surface. One example of such a design is a

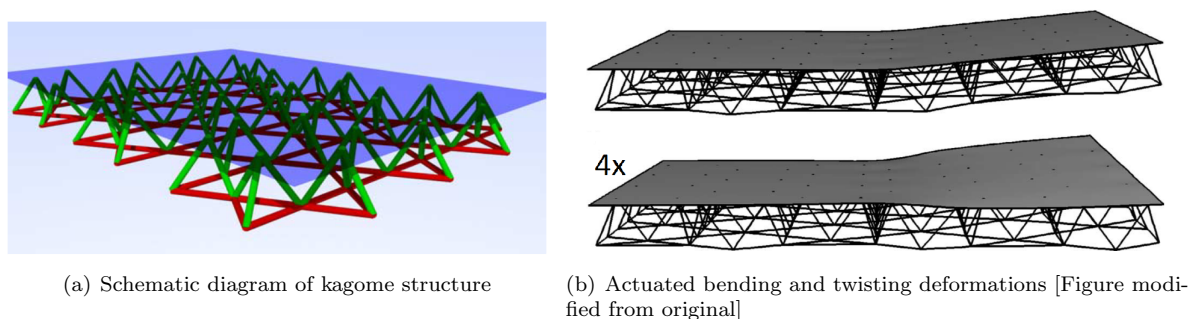


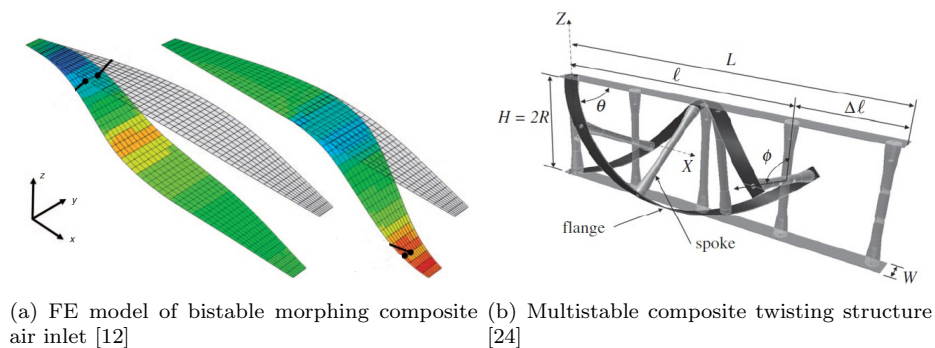
Figure 2.3: Morphing kagome structure [13]. Equivalent or differential actuation results in bending or twisting morphing respectively. The deformations are small due to actuator limitations.

kagome plane and flexible skin separated by a truss-like tetrahedral core. Lucato *et al.* [13] demonstrate this design, which is capable of bending and twisting using embedded linear actuators. Figure-2.3 shows a schematic diagram of the structure as well as the resulting morphing deformation. The authors empirically demonstrate that the structure can morph as desired under a significant load (more than 30 N tip load in a cantilevered setup). They also suggest that the structure would be able to withstand a 294 N load if the structure were not actuator limited. This load-carrying capability is impressive given that the stainless steel core members have a 0.75 x 1.5 mm cross section with a length of 51 mm, resulting in a lightweight structure; see [13] for a detailed analysis of the strength-to-weight capabilities of the structure. Despite its favourable strength-to-weight properties, the structure's deformation is small, as seen in Figure-2.3(b). A corrugated composite structure with elastomeric skin is another alternative [44]. This design consists of carbon-fibre reinforced polymer (CFRP) rods along each fold of the corrugated structure. These rods, combined with an increase in second moment of area due to the corrugation, provide the desired out-of-plane bending stiffness as well as zero- $\nu$  properties. This design proves problematic when large deformations occur and the corrugated structure becomes flattened, thereby reducing the bending stiffness as the deformation increases.

The advantage of these systems is that the skin is not of great concern, since the structure can be designed in such a way that the skin is a highly compliant face sheet, providing the necessary aerodynamic surface. The drawback however, is their increased mass, due to the additional structure. Therefore, the resulting objective is to design a morphing skin that can support large loads without an underlying structure.

### 2.2.2 Stiffness Tailoring of Composites by Multistability

Multistability has been suggested as a possible solution for morphing skins as the skin can exhibit different stable configurations tailored for a given application. The basic principle behind multistability is the minimization of total potential energy (Rayleigh-Ritz method) and is employed by numerous authors. This method is used to obtain the local potential energy minima, each corresponding to a unique stable state of a multistable composite laminate. Emphasis must be placed on the term "local", since a stable state of a laminate can be in a relatively high strain energy state. This results in rapid snap-through when the laminate is acted upon by an external force, thereby increasing the potential energy above its local minimum. It is common for non-symmetric composite laminates to exhibit multistability, but it can also be achieved in a structure comprised of multiple components.



(a) FE model of bistable morphing composite air inlet [12] (b) Multistable composite twisting structure [24]

Figure 2.4: Multistable composite structures. The morphing air inlet is designed for two stable states (inlet closed or open) by tailoring the bending stiffness along its length. The twist morphing structure has three stable states with the intermediate state (darker configuration in the figure) being the minimum strain energy state. The other states are stable only due to the design of the structure’s geometry.

### Multistable Composite Structures

This approach uses monostable and/or multistable composite materials, having increased strain energy due to mechanical deformation, as the driving component for the morphing. Daynes *et al.* [12] demonstrate a morphing composite air inlet, whereby a flat, monostable composite laminate is deformed into a sigmoidal shape with its ends rigidly fixed. In this design, the bending stiffness of the laminate is tailored in the regions that experience large curvature changes by varying the width and thickness of the laminate along its length. The resulting structure is bistable with each stable state corresponding to the open and closed positions of the air inlet respectively, as shown in Figure-2.4(a). This concept introduces the idea of stiffness tailoring by folding, which is further discussed in Section-2.2.4.

Similarly, a multistable twisting composite structure is introduced by Lachenal *et al.* [24], where two composite flanges are separated by rigid spokes. The two flanges are initially curved and thus pre-stressed when flattened and attached to the spokes, as shown in Figure-2.4(b). The structure is tristable; however, two of the stable states are in a state of high strain energy which correspond to local potential energy minima. These states are “stable” only because of the presence of the spokes. A small external input results in snap-through to the intermediate primary stable state. Much like the underlying structures, the extra components add weight to the design, thus limiting the benefit of using such a structure. Another disadvantage of multistability in general is the difficulty in controlling the transition between stable states. This snap-through is typically very rapid and a large amount of energy is transferred from the system. The number of different configurations is limited to the number of stable states, which would not be useful for a control surface, for example. Therefore, the applications in aircraft design for multistable systems are limited.

### Multistable Composite Laminates

Multistability in unsymmetric composite laminates occurs during the curing process due to the variation of thermal expansion of each ply in different directions resulting in out-of-plane deformations.  $[0_n/90_n]$  laminates assume a bistable cylindrical curvature configuration (i.e. zero Gaussian curvature), with the transition being a twisting mode due to uniform heating, as demonstrated by Eckstein *et al.* [14] in Figure-2.5(a).

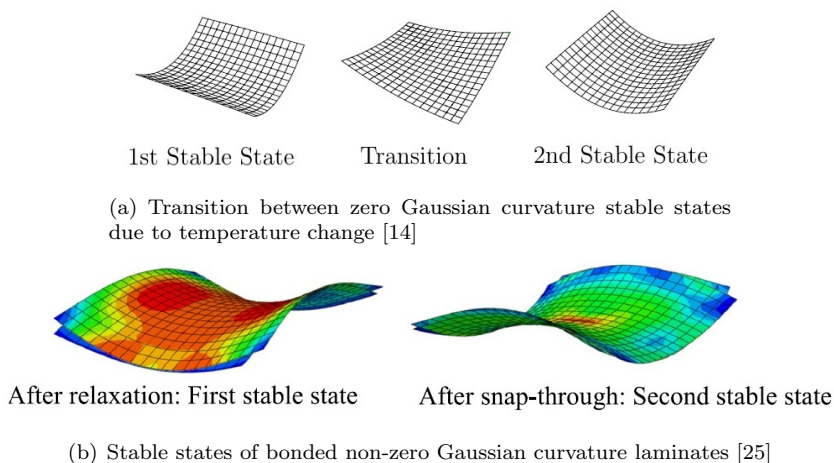


Figure 2.5: Multistable composite laminates. They either exhibit a more useful zero Gaussian curvature (left), even during transition (snap-through), or non-zero Gaussian curvature (right) which is an awkward saddle shape.

Lee *et al.* investigated the bonding of two monostable saddle-shape (non-zero Gaussian curvature) laminates to attain bistability. The two original laminates are mirrored and then flattened and bonded. The two stable states, as seen in Figure-2.5(b), thus correspond to the stable state of each original laminate. The application of this saddle-shape morphing in aerospace is not as useful as cylindrically curved laminates, due to its awkward shape which makes attachment to other structural components challenging. Schultz *et al.* [40] apply the same idea of joining two laminates in order to achieve a bistable twisting airfoil. The challenges facing this design are the difficulty of achieving a suitable airfoil shape as well as the rapid snap-through effects. A simple example of bending morphing is that of Bowen *et al.* [7] where a cantilevered composite beam is stable in the raised state and can snap through to its deflected stable state by shape memory alloy (SMA) actuation.

There is also some research into hybrid composite laminates which include an isotropic material ply (usually metallic) offering the benefit of increased out-of-plane stiffness. A brief analysis on the effects on a laminate of the variation of certain parameters of a steel ply can be found in [9]. Compared to a traditional laminate, the stable curvatures of the hybrid laminate are not affected while the snap-through load is increased more than tenfold.

Even though these multistable laminates are lightweight, compared to multistable composite structures, the resulting shapes are often impractical. Thus, the potential applications are even more limited than multistable structures.

### Stiffness Tailoring Using Prestress

The use of multistable laminates in adaptive structures is troublesome due to low stiffness and relatively small shape changes [11]. An alternative multistable design is achieved via prestress of specific plies of the laminate. During the curing process, the fibres in the outer plies are prestressed and then released once cured. Through-thickness residual stresses develop and cause the laminate to deform resulting in multiple stable states. As mentioned previously, multistability in unsymmetric laminates results in irregular shapes that are often impractical for implementation in adaptive structures. More practical shapes, such as non-Gaussian bending, are achievable with symmetric bistable laminates. An application



of this is aircraft control surface deflection and is demonstrated by Daynes *et al.* [10] using a bistable flap for a helicopter rotor blade.

The challenges surrounding prestress as a viable option for stiffness tailoring are the manufacturing constraints and the resulting induced state of stress. Manufacturing such structures is complex and therefore can be costly, since extra tooling is required and the process requires significant quality control. The induced state of stress may be problematic if the intended application is a critical component. In-flight loads could cause premature failure of the structure, so it would need to be over-designed, thereby increasing its weight.

### 2.2.3 Flexible Matrix Composites

As mentioned previously, elastomers are materials capable of large elastic strains, but they are not ideal for load carrying [22]. A flexible matrix composite (FMC) is a possible solution to this problem; the fibres provide the required strength while the elastomeric matrix provides increased strain capability. Murray *et al.* [30] propose a one-dimensional morphing laminate whereby the stiffness of the composite laminate is tailored by aligning the fibres predominantly in one direction within a high-strain matrix. Fibre orientation has a significant impact on the stiffness of the FMC and in this case the orientation is chosen so as to maximize the difference in perpendicular elastic moduli. The matrix-dominated direction is aligned with the desired morphing direction. The out-of-plane stiffness is relatively low, but one can use pre-tension in the fibre-dominated direction to induce high out-of-plane stiffness while still being able to stretch the laminate in the matrix-dominated direction.

Murray *et al.* conduct empirical validation of out-of-plane deflections of a  $\pm 75^\circ$  laminate for varying applied loads and pre-tension values. They also investigate the effects of fibre and matrix elastic moduli as well as the size of the composite laminate. The authors focus on one-dimensional morphing, which has certain applications in aircraft, but many applications require two- or three-dimensional morphing, such as a morphing flap. In such applications, fibre pre-tension is challenging to implement, so it is useful to consider the effects of the other parameters without pre-tension. Figure-2.6 shows the effects of fibre and matrix moduli on the out-of-plane deflections of the laminate. It can be seen that the compliance is primarily affected by the fibre elastic modulus rather than that of the matrix, assuming that a relatively low elastic modulus matrix is employed.

Maqueda *et al.* [26] characterize the mechanical properties of a silicone-based, high-strain composite material. They conduct their analysis on unidirectional laminates only, not considering angle-ply laminates. Nonetheless, this investigation provides useful information regarding the expected material properties of elastomeric composites. It is found that the rule of mixtures provides accurate predictions for tensile and bending properties, but predictions of the compressive properties are highly inaccurate, over-predicting the elastic modulus by a factor of 3. The authors cite two potential sources of error, namely the initial waviness of the fibres, and non-uniform loading in the compression experiment setup. They also suggest the possibility that the rule of mixtures is inadequate for predicting the compressive properties of composites of this type, but they remain unconvinced. The authors also observe fibre microbuckling in the compression experiments, which is investigated in great detail by Jiménez [21]. In this current work,  $[(\pm 45F)_n]$  layups are primarily used, where F denotes a plain-weave fabric, so fibre microbuckling is less of a concern.

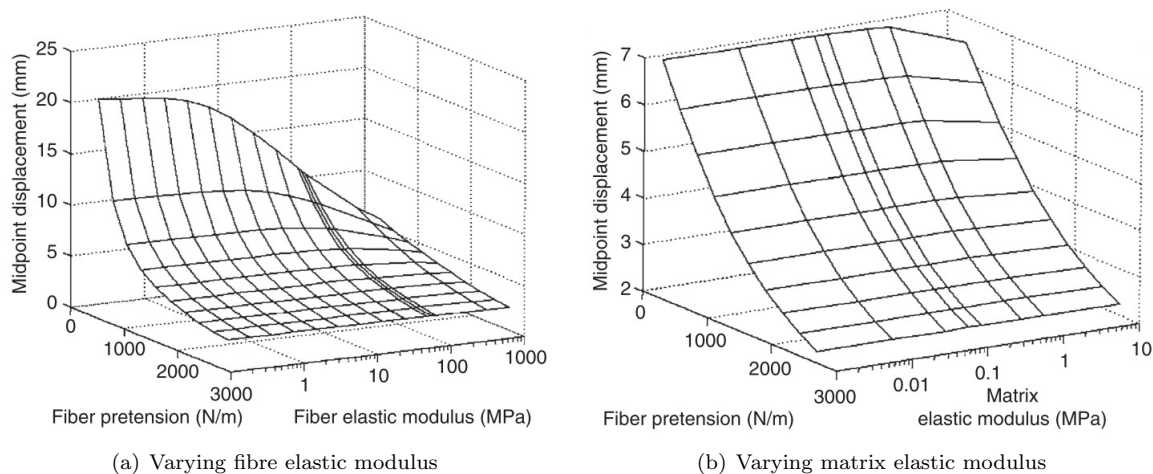
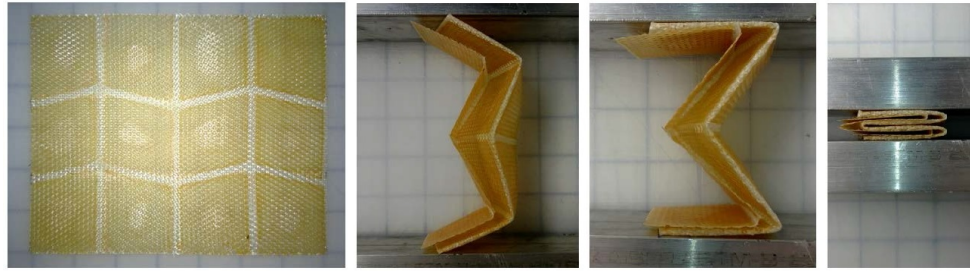


Figure 2.6:  $\pm 75^\circ$  flexible matrix composite out-of-plane deflections for an applied pressure load of 1.20 kPa for varying fibre pretension along with fibre and matrix elastic moduli [30]. The fibre elastic modulus has a greater impact on the stiffness of the laminate compared to the matrix elastic modulus.

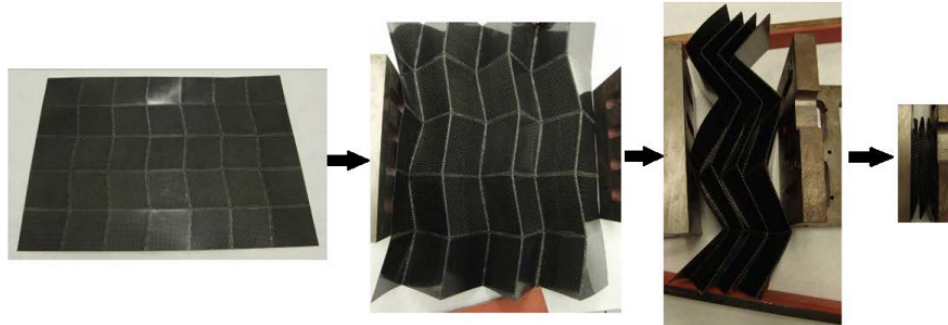
## 2.2.4 Dual-Matrix Composites

A traditional fibre-epoxy laminate can be combined with the aforementioned FMC, resulting in what is known as a dual-matrix composite. The term *dual-matrix composite* typically refers to the silicon-carbide (C/SiC) type which is a resilient ceramic with increased ductility [32]. However, the dual-matrix composite referred to here is on the macroscale where multiple matrix materials with different properties are used in discrete regions to tailor the stiffness in those regions. The literature available for this field of research is somewhat limited given the relative novelty of this technology, but some interesting work has been conducted by researchers and companies to produce as well as investigate dual-matrix composites. Compared to the aforementioned stiffness tailoring techniques, dual-matrix composites are arguably the most practical for morphing applications, given their compactness, low weight, relative ease to manufacture, and superior stiffness tailoring capability. For this reason, dual-matrix composites are chosen for further investigation in this work.

Jiménez [21] presents a folding Miura-ori design with a silicone/epoxy dual-matrix composite, and this is further extrapolated to a deployable space antenna for CubeSats [39]. The panels of the structure are traditional glass-fibre reinforced polymer (GFRP) with epoxy resin as the matrix material, while the fold lines have a silicone-based matrix. The elastomeric silicone permits large curvature changes with folds close to  $180^\circ$  being demonstrated, as shown in Figure-2.7(a). The damage tolerance of this material is exceptional, given that the flexible resin is capable of high strains well exceeding unity. This particular laminate is fabricated using UV-cure silicone but this processing path can be limiting, since it requires translucent fibres such as glass. Since weight is a dominant driving factor for aircraft design, engineers preferentially utilize carbon fibre over glass fibre, which has lower stiffness- and strength-to-weight ratios. However, glass fibre and other fibre types are still used as they have some beneficial properties depending on the application. Carbon fibre dual-matrix composites therefore require matrix materials which have alternative curing processes. L'Garde Inc. have developed dual-matrix composites using carbon fibre as seen in Figure-2.7(b). The manufacturing process for the carbon fibre laminate



(a) Glass fibre Miura-ori pattern [21]



(b) Carbon fibre Miura-ori pattern [26]

Figure 2.7: Folding Miura-ori structures using dual-matrix composites. Both the glass fibre and carbon fibre designs exhibit large curvatures with almost  $180^\circ$  folds, thereby demonstrating the high strain capability of the silicone regions.

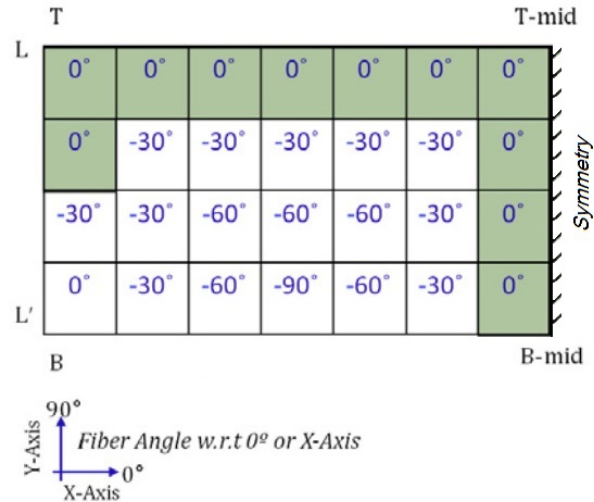
is proprietary information, so a novel manufacturing technique is used in this work and is detailed in Chapter-3.

### 2.2.5 Fibre Tow Steering

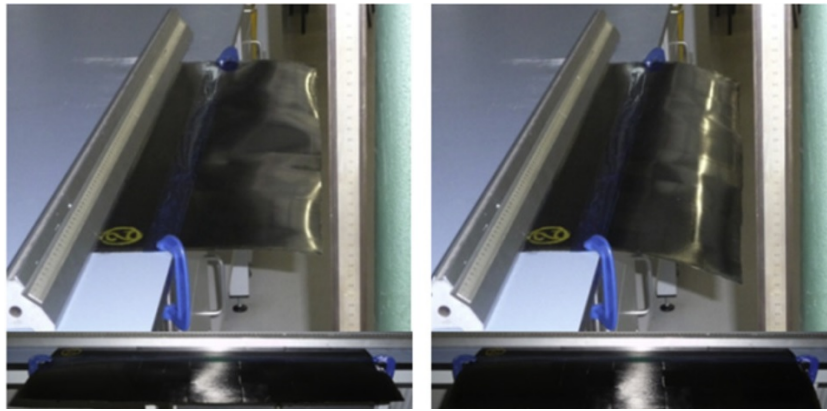
Panesar and Weaver [35] investigate the use of fibre tow steering to design a bistable morphing flap. One advantage of tow steering is that the fibre angles, and hence mechanical property directivity, can be altered within a ply without the need for discontinuous fibres. Another benefit is that the ply can be integrated more easily with the surrounding structure. In this case, the authors use fibre-orientation optimization to create a morphing flap that is integrated into the wing skin. The fibre alignment at the joint between the wing and the flap matches that of the wing structure while at the trailing edge of the flap, the angles are vastly different (up to  $90^\circ$ ) to suit the desired morphing shape. The top two plies of the flap laminate have variable angle tows (VATs) while the bottom two plies have  $0^\circ$  fibre orientation thereby inducing bistability in the laminate. Figure-2.8(a) shows an example of one of the results of the optimization process; the authors limited the angle variation between elements to  $30^\circ$  to ensure practical fibre rotations which can actually be fabricated.

The testing of the flap yielded trailing edge deflections of greater than 50 mm for a 700 x 200 mm flap. Although the results of this investigation demonstrate the feasibility of a bistable flap using VAT, the retracted shape of the laminate is aerodynamically problematic due to non-zero curvature which varies along the span of the flap as seen in Figure-2.8(b). This is typical of bistable laminates which often exhibit non-zero curvature in their stable configurations, thus a flat bistable laminate is





(a) Fibre angles resulting from optimization process



(b) Demonstration of morphing flap

Figure 2.8: Bistable morphing flap using variable angle tows [35]. The flap achieves the desired morphing deformation, but it exhibits a non-flat surface in the undeflected position.

not easily achievable. To the author's best knowledge, there are no flat bistable laminate designs. Furthermore, this particular bistable morphing flap design has only two discrete flap positions so there is no control over the intermediate deflection of the flap. Multistable designs with three or more stable states would be more beneficial but more challenging to design and optimize. The authors do not consider aerodynamic loads which would have a significant effect on the deflection of the flap. Nonetheless, this design provides a basis for potential morphing flap designs using VAT technology and with the rapid development of composite manufacturing techniques, complex designs are becoming increasingly feasible. VAT techniques are potentially useful for dual-matrix laminates in that the compliance of the flexible region can be additionally tailored whilst maintaining continuous fibre paths.

The benefits of fibre tow steering are substantial but the drawback to this technology is the manufacturing complexity. Specialized machinery is required, resulting in an expensive fabrication process.

## 2.3 Anticlastic Effects in Beams Subjected to Bending

### 2.3.1 Anticlastic Curvature Modelling

The bending of a plate or beam is typically accompanied by an anticlastic curvature in the orthogonal direction to the axis of applied curvature as shown in Figure-2.9. The deformed shape of the cross section due to the anticlastic effect has been investigated thoroughly with some of the first work being conducted by Ashwell [4], who models this behaviour in isotropic plates. Pomeroy [37] expands on the previous work of Ashwell by investigating the impact of this phenomenon on a beam's cross-sectional second moment of area. This work provides valuable insight into the transition between narrow beam theory and wide beam theory. When a principal curvature is induced in a narrow beam by an applied moment,  $M$ , the transverse anticlastic curvature is defined by

$$\kappa_y = -\nu\kappa_x, \quad (2.1)$$

where  $\nu$  is the Poisson ratio. Thus, the transverse curvature is constant and a linear function of the principal curvature. Wider beams, however, have a non-linear relationship between the perpendicular curvatures. Pomeroy uses the assumption made by previous authors that the anticlastic curvature can be represented by a beam on an elastic foundation. The author derives an expression for the curvature of a wide beam and shows that the curvature near the edges of the cross-section follows the narrow beam theory whilst the curvature elsewhere is

$$\kappa_y = \frac{d^2w}{dy^2}, \quad (2.2)$$

where  $w$  is the deflection in the  $z$ -direction. The theoretical derivations and assumptions made therein are applicable to materials that have a Poisson ratio no greater than 0.5. Even though this work serves as a foundation for understanding the effects of anticlastic bending, the expressions obtained cannot be applied to composite analysis where it is common to encounter Poisson ratios in excess of 0.5. For example, the author expresses  $w$  in terms of ordinary and hyperbolic trigonometric functions of argument,  $ay$ , where  $y$  is a position along the width of the cross section and

$$a = \left[ \frac{kdl(1 - \nu^2)}{4EI} \right]^{1/4}. \quad (2.3)$$

The important term in Equation (2.3) is  $(1 - \nu^2)$  while the undefined parameters are not important for this discussion. Evidently, for a Poisson ratio of close to unity (which is possible for certain composite layups, particularly  $\pm 45^\circ$ ),  $a$  approaches zero resulting in an undefined function for  $w$ . Nonetheless, Pomeroy's work is useful for understanding anticlastic effects in beams, especially the transition from narrow beam to wide beam behaviour.

Pao [36], and Hyer and Bhavani [20], extend the theory to composite laminated plates. The authors derive theoretical models to predict the deformed shape of the plate cross-section for an induced longitudinal radius of curvature,  $R$ . This radius of curvature can be related to the applied moment,  $M$ , if the bending stiffness of the plate or beam is known. This theoretical model forms the foundation of this work and is presented in detail in Chapter-4.

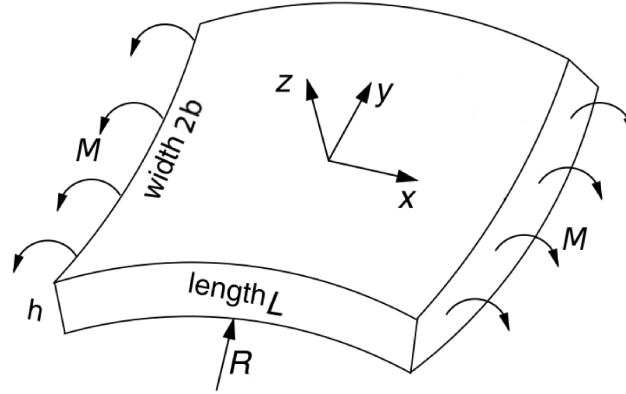


Figure 2.9: Anticlastic effect in a beam due to an applied moment [Modified from original source [42]]

### 2.3.2 Neutral Axis Definition

The geometric neutral axis of a cross section may not necessarily be the actual neutral axis when a beam or plate is subjected to a bending moment. The geometric neutral axis,  $\bar{z}$ , is calculated by discretization of the arbitrary cross section into  $N$  infinitesimal elements of area  $A_i$  and distance  $z_i$  from a reference axis, and evaluating the expression

$$\bar{z} = \frac{\sum_{i=1}^N A_i z_i}{\sum_{i=1}^N A_i}. \quad (2.4)$$

Equation-2.4 assumes that the location of the neutral axis is entirely a function of the cross-section geometry, that is, the neutral axis coincides with the centroid. In addition, this theory assumes that the beam is a straight beam. It is well documented in the literature that the neutral axis does not coincide with the centroid for curved beams [18]. This also applies to beams undergoing large curvatures, where the beam can no longer be assumed to be straight.

The well-known definition of the actual neutral axis is the axis at which the bending stress, and likewise the strain, is zero. However, this does not provide an indication of its location without knowing the stress distribution. Another definition is that the sum of moments about the neutral axis, from the compressive and tensile regions, must equal the bending moment in the beam. In addition, the sum of forces must equate to zero (for pure bending load cases) to ensure equilibrium. For relatively thick sections of a material which exhibits identical compressive and tensile elastic properties, the geometric neutral axis will generally coincide with the actual neutral axis. Most composite applications employ thin laminates, so the anticlastic effects have a greater impact on the location of the neutral axis and, as a result, the second moment of area (Section-4.3 investigates this in more detail). Furthermore, the elastic properties of certain materials can differ significantly in tension and compression (see Section-3.3). The combination of small thickness and relatively large shift in neutral axis compounds the increase in the second moment of area of the beam's cross section.

## Chapter 3

# Manufacturing Process and Material Characterization

The manufacturing process of a dual-matrix laminate poses some unique challenges. First, the selected matrix materials need to be mutually compatible, as well as compatible with the fibres. In addition, the interface between the matrix materials needs to be free of voids, as well as having minimal overlap. If there is significant overlap or excessive voids, the flexible region can be compromised and the effectiveness of the dual-matrix is reduced. Furthermore, predicting the mechanical behaviour of the flexible region becomes challenging, if not impossible.

This chapter details the manufacturing procedure of the dual-matrix laminates fabricated for this work. Carbon fibre reinforced epoxy and carbon fibre reinforced elastomer are mechanically tested in tension and compression to characterize their material properties.

### 3.1 Material Selection

There are various types of fibres commonly used in composites, but for typical applications there are essentially two choices, namely glass or carbon fibres. The only benefit of glass compared to carbon in this particular application is its translucency. As with the UV-cure silicone used in the dual-matrix laminate designed by Jiménez [21], glass fibres are essential to allow the matrix to cure completely. However, carbon fibre has superior stiffness, strength and density properties, thereby allowing for enhanced efficiency of the whole structure. Since the primary application of this research is related to cabin interiors, aesthetics also play a role in the choice of materials, and carbon fibre is widely regarded as more aesthetically appealing than fibreglass. Therefore, carbon fibre is chosen even though the use of non-UV curing elastomeric resin becomes necessary. Plain-weave carbon fibre fabric is used in this work because of its superior workability compared to unidirectional tape. Unidirectional tape is typically supplied in thin strips (only a few inches wide), so the allowable laminate dimensions are limited, especially for an angle-ply layup, whereas woven fabric is usually supplied in large rolls of a few feet wide. Unidirectional plies are also more susceptible to fibre misalignment during hand lay-up, as the fibres are dragged in the direction in which the resin is applied. Unidirectional carbon fibre prepreg is often used to prevent this, but this is not suitable for dual-matrix applications. In this application, plain-weave fabric is advantageous over other weave patterns, since the fibre tow length for each undulation of the weave is as small

as possible, which has greater resistance to fibre-tow buckling (see Section-3.3.3). The specifications of the plain-weave fabric supplied by Freeman Manufacturing are 3K tows (warp and fill) with a 12 x 12 (ends x picks) construction and a weight of 5.7 oz./sq.yd.

Two matrix materials with significantly different elastic moduli are essential to ensure that there is a large enough disparity in the bending stiffness of each region of the laminate. Traditional epoxy (Araldite LY 8601 / Aradur 8602 System) is used in the rigid section and polyurethane elastomer (Freeman 1040) is used for the compliant section. The latter is chosen by comparing a number of elastomers including silicone-based materials. Freeman Manufacturing supplies polyurethane elastomers at a relatively inexpensive cost compared to silicone-based resins. Two elastomers are compared, namely Freeman 1040 and 1050. The 1040 elastomer is specified as an overnight-cure flexible elastomer while the 1050 is an overnight-cure semi-rigid elastomer. Freeman 1040 is preferred due to its higher compliance. This elastomer also has a rapid gel time of 28 minutes, which is advantageous for isolating the elastomeric resin, preventing excessive seepage of the resin outside the intended area of application when curing. Similarly, UV-cure elastomeric resins are beneficial for isolating the compliant regions of a laminate, but the opacity of carbon fibre inhibits the curing of the resin between plies, as mentioned previously.

## 3.2 Dual-Matrix Fabrication

### 3.2.1 Method

A two-stage fabrication process is employed for the manufacture of the dual-matrix laminate. This procedure is demonstrated in Chapter-5 with the manufacturing of a tray table prototype.

#### Stage One

1. Measure and cut all the necessary peel plies, plastic films, breather ply and carbon fibre fabric plies.
2. Place a thin plastic film on the mould (or flat plate), as well as a peel ply on top of the plastic film. Alternatively, one can use a release agent instead of the peel ply for a higher quality surface finish.
3. Demarcate the isolated area on the peel ply to which the elastomeric resin will be applied.
4. For the desired fibre volume fraction, measure out the appropriate quantities of polyurethane hardener and resin, according to the manufacturer's specification (ratio of 10:1 respectively for Freeman 1040). Mix them well. It is a good idea to prepare 150% of the required resin to allow for losses during vacuum cure. Special note: once this step is reached, subsequent steps need to be conducted quickly before the elastomer gels.
5. Apply a proportionate amount of elastomeric resin to the designated area on the peel ply.
6. Place the first pre-cut fibre ply in the desired orientation on the wet resin. Special note: Due to the high viscosity of the elastomeric resin, the layup has to be done ply by ply or, at most, two plies at a time to ensure sufficient resin penetration.
7. Apply elastomeric resin on the fibre ply being careful not to damage the fibres nor allow the resin to escape outside the defined boundary.

8. Repeat steps 6 and 7 for all the plies making sure to use all the resin.
9. Cover the wet laminate with another peel ply, followed by a breather ply.
10. Place a vacuum pipe close to, but not on top of, the laminate and cover with another plastic sheet. This second plastic sheet needs to have double sided tape along its edges to ensure a vacuum seal.
11. Turn on the vacuum system and ensure that the vacuum quality is adequate.
12. Leave to cure for a minimum of 16 hours.

### Stage Two

For the second stage of the process, repeat stage one with epoxy resin in the remaining dry sections. Ensure that the epoxy closes the gap between the sections (the elastomeric resin acts as a dam), but be careful not to induce overlapping of the resins. Leave the vacuum bagged laminate to cure for 24 hours.

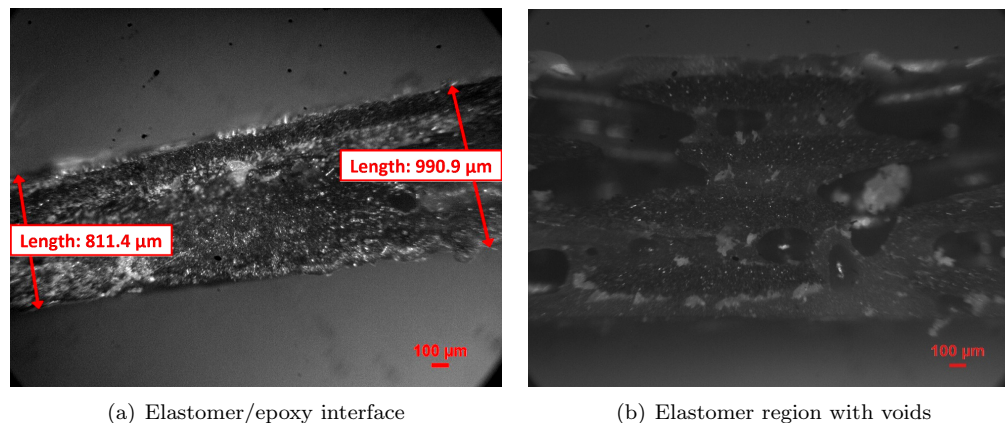
Due to the peel ply, the surface finish of the laminate is relatively rough and aesthetically undesirable. Certain applications may require a better surface finish, as with this work for instance, given that the primary application is a tray table in a commercial aircraft. In order to obtain a smoother surface finish with a more appealing carbon fibre appearance, one can replace the bottom peel ply with a release agent. In this work, Huntsman Renlease<sup>®</sup> 76 US is used.

### 3.2.2 Micrographs

Micrographs are taken of the elastomer/epoxy interface as well as the carbon fibre/elastomer layup. Figure-3.1(a) shows this interface for a  $[(\pm 45F)_4]$  laminate. It can be seen that there are very few voids, providing a high quality continuous matrix. Another observation is that the elastomer region is thicker than the epoxy region by approximately 180  $\mu\text{m}$ . The manufacturing process revealed a prominent difference in the viscosity of the two resins. As a result, less of the excess elastomeric resin is expelled during the vacuum seal, compared to the epoxy resin. Furthermore, the quick gel time of the elastomer resin has a significant effect on the final laminate thickness, as well as the quality. For example, Figure-3.1(b) shows a section of a  $[(\pm 45F)_8]$  laminate where the gel time is exceeded during manufacturing. The vacuum cannot induce sufficient pressure on the laminate to expel these voids, and the result is a poor quality layup. The lesson learnt from this is that for laminates with many plies, it is essential that the gel time is not exceeded before the vacuum is applied to ensure sufficient cure quality.

## 3.3 Composite Mechanical Properties

All tensile and compressive testing discussed in the following sections is conducted using a MTS 880 Material Test System with a 100 kN load cell. An Electronic Instrument Research LE-05 laser extensometer is used for strain measurements. Figure-3.2 shows the different tension and compression setups. The tensile specimens are gripped using mechanical grips while the compression specimens are fixed in a Wyoming Test Fixtures Inc. compression test fixture to ensure accurate alignment (See Appendix-B for the apparatus details). The material properties obtained through testing are summarized in Table-3.1. Subsequent sections explain these results in more detail.



(a) Elastomer/epoxy interface

(b) Elastomer region with voids

Figure 3.1: Micrographs of dual-matrix composite layup. The interface between the matrix materials shows good penetration of resin with few voids. The thicker elastomer laminate shows poor penetration quality with many voids, when the gel time of the resin is exceeded during hand lay-up.

Table 3.1: Measured material properties

Parameter	Elastomer	CF/epoxy [(0/90F)]	CF/epoxy [±45F]	CF/elastomer [(0/90F)]	CF/elastomer [±45F]
$E_t$ (MPa)	2.47	45,300	11,900	21,000	38.0/117 <sup>1</sup>
$E_c$ (MPa)	–	73,500	7,920	–	–
$\nu_{xy}$	0.45–0.50	0.09	0.85	0.55	~1.0

The laminate samples used in the material characterization are nominally 20 mm wide and 1 mm thick for the tensile tests, and 20 mm wide and 1.6 mm thick for compression; the larger thickness delays the onset of buckling. The lengths of the specimens are also shorter compared to the tensile specimens, as seen in Figure-3.3. The laminates are prepared for testing by affixing aluminum tabs to the ends using heat-cure adhesive film. The tabs prevent damage to the fibres that would otherwise be caused by the mechanical grips. It is found that for higher temperatures, the adhesive cures well but the elastomer resin melts, causing irreparable damage to the samples. However, at lower temperatures the adhesive doesn't bond the parts effectively. A range of temperatures are investigated and presented by Ahmadi *et al.* [1] who find the optimal temperature to be 175°F, providing strong adhesive bondage with no damage to the laminate samples.

### 3.3.1 Polyurethane Elastomer

An elastomer test sample, supplied by Freeman Manufacturing & Supply Company, is tested in tension to acquire the mechanical properties of the elastomer. The results of this test are shown in Figure-3.4 where the same sample is tested at three different axial displacement rates. The average elastic modulus of the elastomer is 2.47 MPa which is shown to be independent of strain rate.

The Poisson ratio of the elastomer is difficult to measure experimentally; there are two techniques available to the author that are attempted. First, a strain gauge is affixed to the sample during tensile testing. These tests revealed unexpected results with an extremely low Poisson ratio which is uncharacteristic of an elastomer, for which a Poisson ratio close to 0.5 is expected. Cyanoacrylate adhesive is

<sup>1</sup>See Section-3.3.3

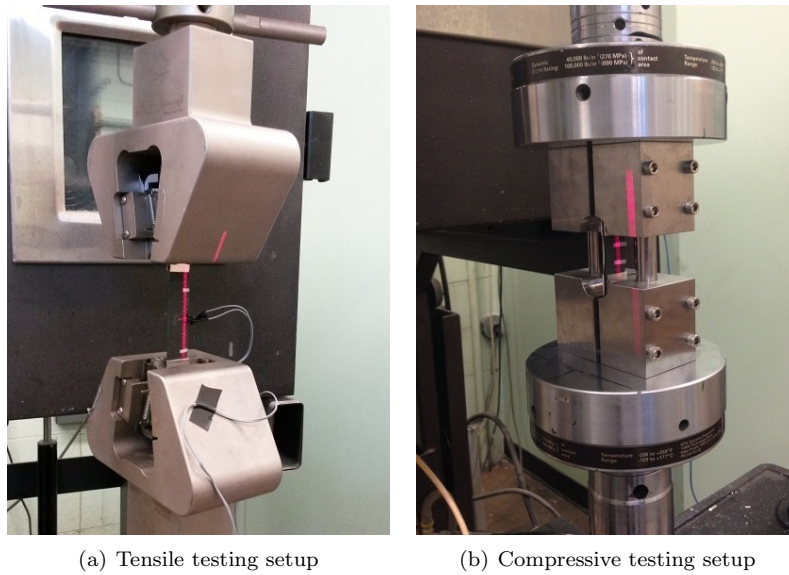


Figure 3.2: Experimental apparatus for material characterization.

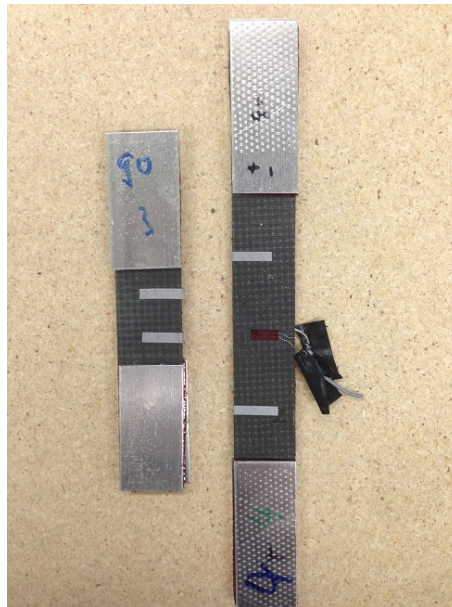


Figure 3.3: Laminate test samples for material property characterization in compression (left) and tension (right).



used to bond the strain gauge to the elastomer and a finite element (FE) analysis of the setup shows that the difference in elastic moduli of the two materials affects the strain at the point of interaction. In other words, as the elastomer contracts due to Poisson effects, the adhesive limits this contraction, thereby suggesting a lower strain than is truly experienced by the elastomer sample. While the elastic modulus of the adhesive used here is not explicitly published by manufacturer (Krazy Glue<sup>®</sup>), Mizrahi *et al.* show that the elastic modulus of Dermabond<sup>®</sup> cyanoacrylate medical adhesive is approximately 500 MPa [29]. The accuracy of the elastic modulus is unimportant as the purpose of this comparison is to demonstrate the effects of the different elastic moduli of the two materials, being in the region of two orders of magnitude. For the purpose of the FE simulation, 500 MPa is used as the elastic modulus for the adhesive. Figure-3.5 shows the results from the FEA; Abaqus outputs strain as logarithmic strain instead of engineering strain. For the purpose of visualization, the contour of the  $x$ -direction logarithmic strain,  $LE_{11}$ , is plotted to show that the strain in the region of adhesive application is lower than that at a distance from the adhesive, where the strain is relatively uniform. The engineering strain is manually calculated by extracting the relative  $x$ -displacement ( $U1$  in Abaqus) of points A and B in Figure-3.5, and dividing by the width of the adhesive region (5 mm). In the FE model, a  $y$ -displacement boundary condition of 5 mm is applied to the top of the sample, so the strain in the  $y$ -direction is known. Table-3.2 shows the results from the FEA, as well as from the experiments.

The second technique considered for measuring the Poisson ratio is speckle pattern image correlation, however, the paint used in this technique cracks when the sample is strained excessively, thereby nullifying the image correlation data. As a result, a value within the range of 0.45–0.5 is assumed sufficient.

### 3.3.2 Carbon Fibre/Epoxy Laminate

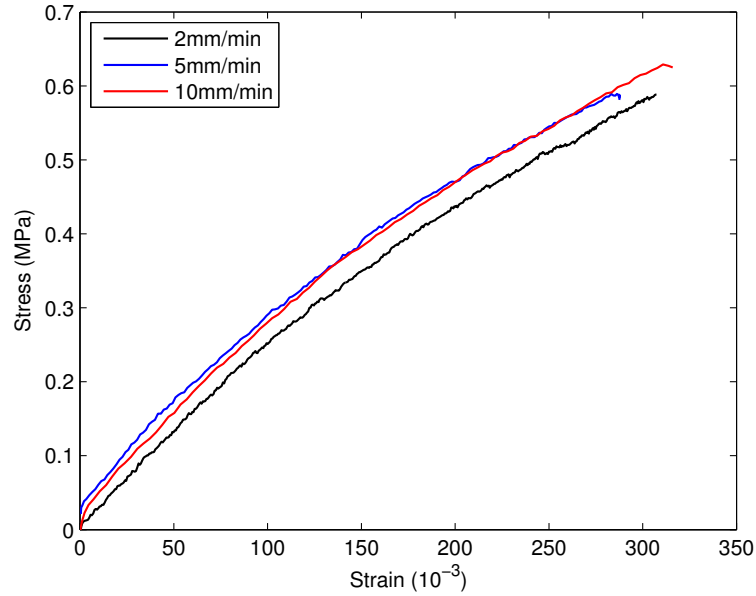
#### Tensile Testing

Two different layups are tested in tension, namely  $[(0/90F)_4]$  and  $[(\pm 45F)_4]$ . Figure-3.6 shows the results of the  $[(0/90F)_4]$  tensile test. The effective elastic modulus in the longitudinal direction is 45.3 GPa and the Poisson ratio is 0.090. The transverse strain results for Sample 2 are omitted because the strain gauge detached from the sample during testing. Nonetheless, the other two samples are in good agreement for the Poisson ratio. The elastic modulus correlates well with the predictions of classical lamination theory (CLT), which predicts a value of 43.7 GPa. There is a discrepancy in the Poisson ratio, with the theoretical prediction being 0.031. This is most likely a consequence of the theory applying to laminates of unidirectional plies specifically, while the samples have woven plies.

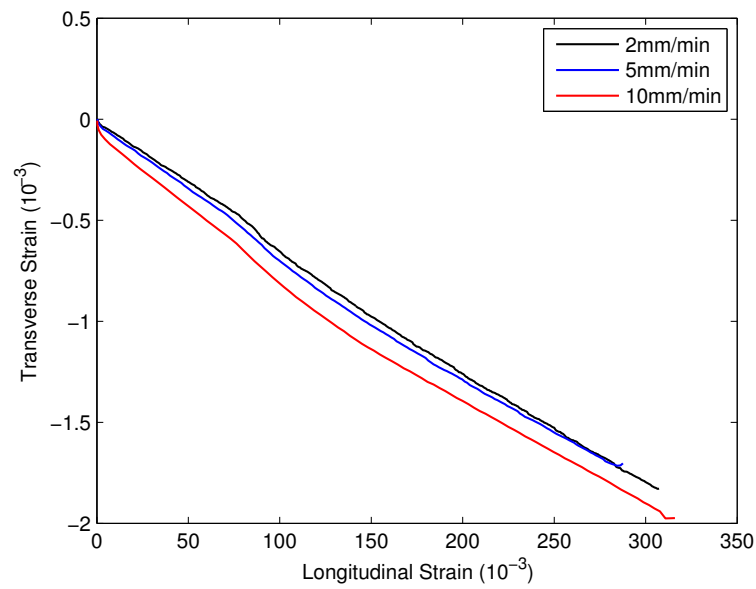
Figure-3.7 shows the results of the  $[(\pm 45F)_4]$  tensile test, and the measured elastic modulus is 11.9 GPa with a Poisson ratio of 0.85. CLT predicts an elastic modulus of 3.84 GPa and a Poisson ratio of 0.94. The elastic modulus of the epoxy is estimated to be around 500 MPa as suggested by Huveners *et al.* [19]. Once again, this discrepancy is expected due to the limitations of CLT, especially since

Table 3.2: Reduction in measured Poisson ratio of an elastomer with surface adhesive of varying thickness

Parameter	No adhesive	Adhesive (1 micron)	Adhesive (10 microns)	Experiments
$\epsilon_y$	0.152	0.152	0.152	N/A
$\epsilon_x$	0.0682	0.0461	0.0328	N/A
$\nu_{yx}$	0.450	0.304	0.217	0.0061



(a) Tensile stress-strain curve



(b) Transverse strain versus longitudinal strain

Figure 3.4: Tensile testing data for Freeman 1040 polyurethane elastomer for the characterization of the stiffness and Poisson ratio.

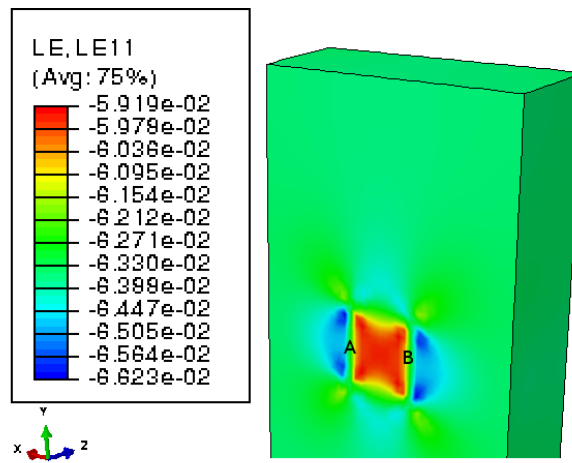


Figure 3.5: FE model showing reduction in strain of an elastomer due to an adhesive on its surface.

$[\pm 45]$  laminate properties are dominated by shear, which would behave differently for unidirectional plies versus woven plies, although the predicted Poisson ratio is reasonably close to the experimental results.

### Compressive Testing

The compression properties of carbon fibre/epoxy laminates are obtained experimentally through compression testing of 1.6mm thick laminates for both  $[(0/90F)_8]$  and  $[(\pm 45F)_8]$  layups. The results are shown in Figure-3.8 and the average measured Young's moduli for the  $[(0/90F)_8]$  and  $[(\pm 45F)_8]$  laminates are 73.5 GPa and 7.92 GPa, respectively. The latter value is calculated in the near linear region for strains less than 0.003.

### 3.3.3 Carbon Fibre/Elastomer Laminate

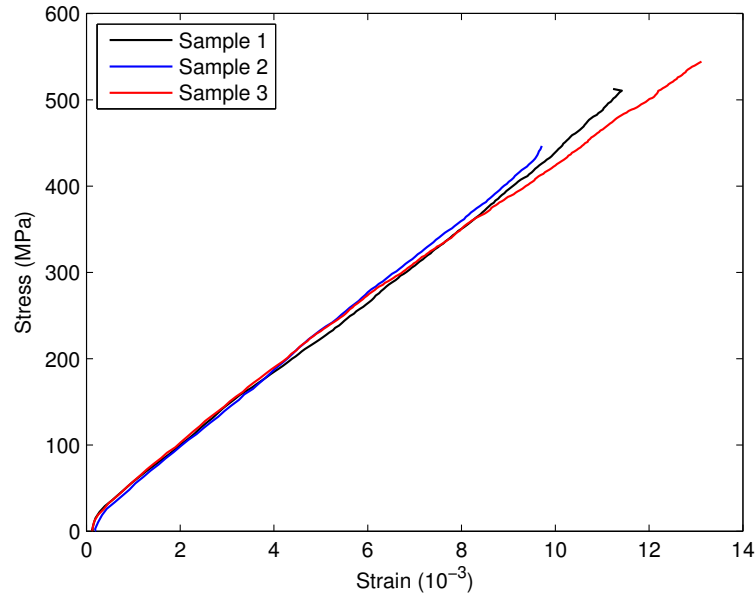
#### Tensile Testing

The tensile testing of the  $[(0/90F)_4]$  layup is difficult due to shearing between the aluminum tab adhesive and the sample. The mechanical grips provide sufficient clamping force for all other testing except for this case. The interface between the adhesive and elastomer does not have sufficient strength to overcome the large tensile force. Hydraulic clamps may be useful for this application but there is a risk of damaging the samples with excessive clamping force. Mejia-Ariza *et al.* [28] conduct experiments on carbon fibre reinforced elastomers, and they likewise find that the tabs shear off the samples during testing. They attempt to use hydraulic clamps but these crush the test samples.

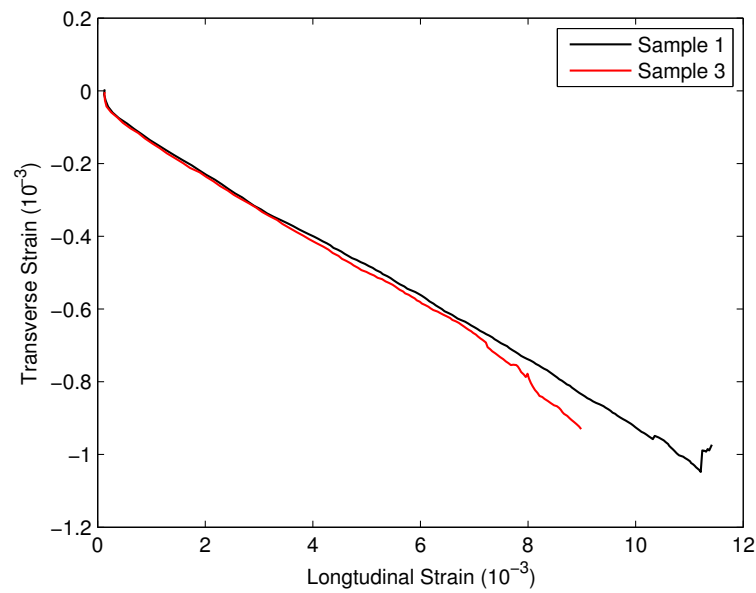
The key parameter desired from these tests is the effective Young's modulus of the laminate. This test setup provides sufficient data to determine this value to be approximately 21.0 GPa; the results of the tensile test are shown in Figure-3.9(a). The  $[(\pm 45F)_4]$  laminate exhibited interesting tensile properties with the stress-strain relationship being bilinear. The Young's moduli in these two linear regions are measured as 117 MPa and 38.0 MPa respectively. The first transition region begins at a strain of approximately 0.020 (stress  $\approx$  2.0 MPa) and ends at a strain of approximately 0.030 (stress  $\approx$  3.0 MPa).

#### Compressive Testing

It is desired to obtain the Young's modulus in compression for the elastomeric laminate, since it affects the bending behaviour of the laminate (this is discussed briefly in Section-4.3.2). Compression testing of thin elastomeric laminates proves to be difficult; carbon-fibre/elastomer tubes are more suitable for this purpose. Consequently, the thin  $[(0/90F)_8]$  laminate buckles under the load of the compression test fixture itself, making compressive testing with the MTS system impossible for these elastomeric laminates. Maqueda and Pellegrino [26] use unidirectional carbon-fibre/silicone rods as test samples. They show that the elastic modulus in compression is approximately one third of that predicted by the rule of mixtures. Theoretical predictions may not be applicable to elastomeric laminates in compression. The carbon fibre and elastomer in these authors' work have the same mechanical properties as those used in this work. As an estimate, one can use the relative values for the tensile and compressive elastic moduli. The ratio of the compressive modulus to the tensile modulus is approximately 0.47.

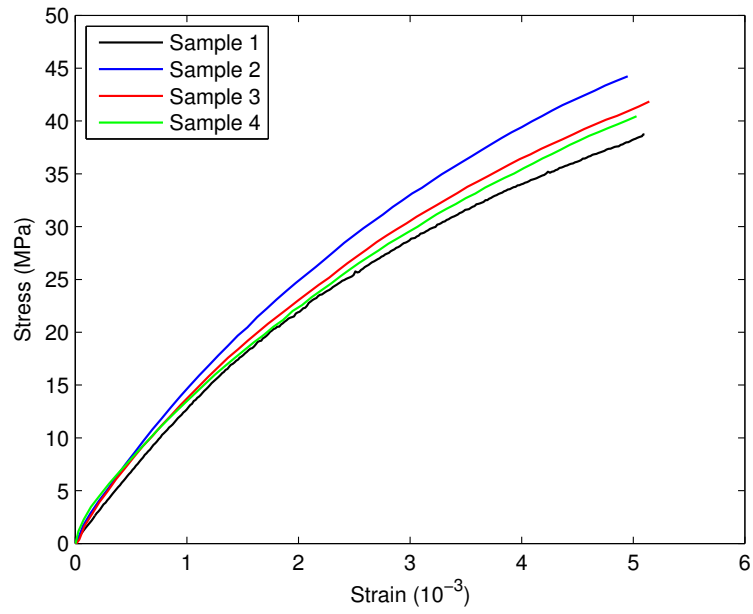


(a) Tensile stress-strain curve

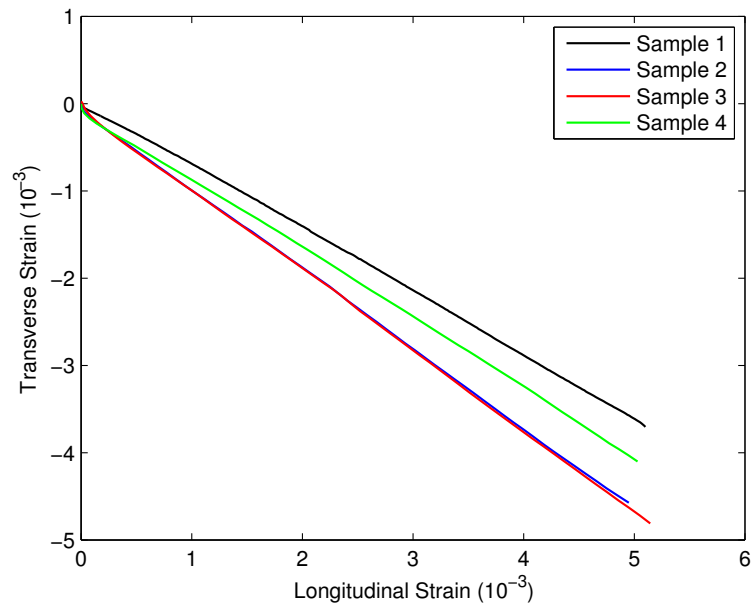


(b) Transverse strain versus longitudinal strain

Figure 3.6: Tensile testing data for  $[(0/90F)_4]$  carbon fibre/epoxy for the characterization of the stiffness and Poisson ratio.



(a) Tensile stress-strain curve



(b) Transverse strain versus longitudinal strain

Figure 3.7: Tensile testing data for  $[(\pm 45F)_4]$  carbon fibre/epoxy for the characterization of the stiffness and Poisson ratio.

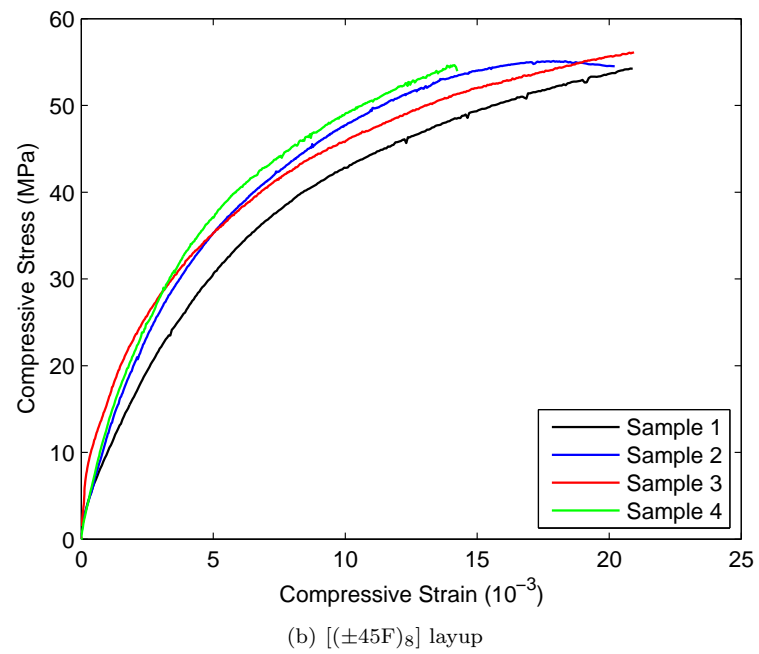
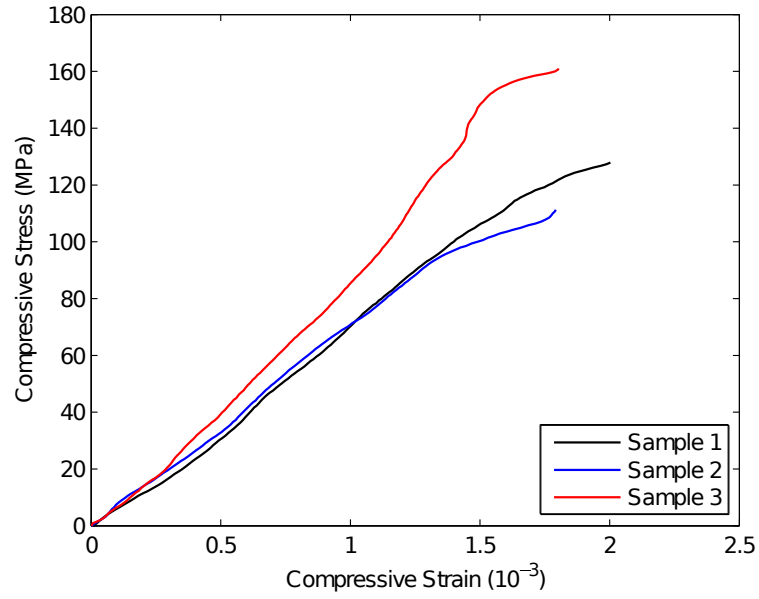


Figure 3.8: Compressive stress-strain results for carbon fibre/epoxy for two different layups.

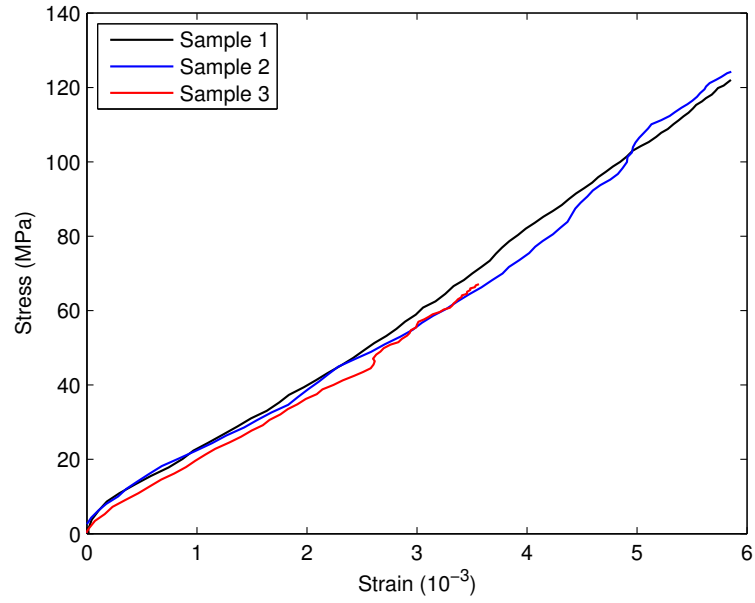
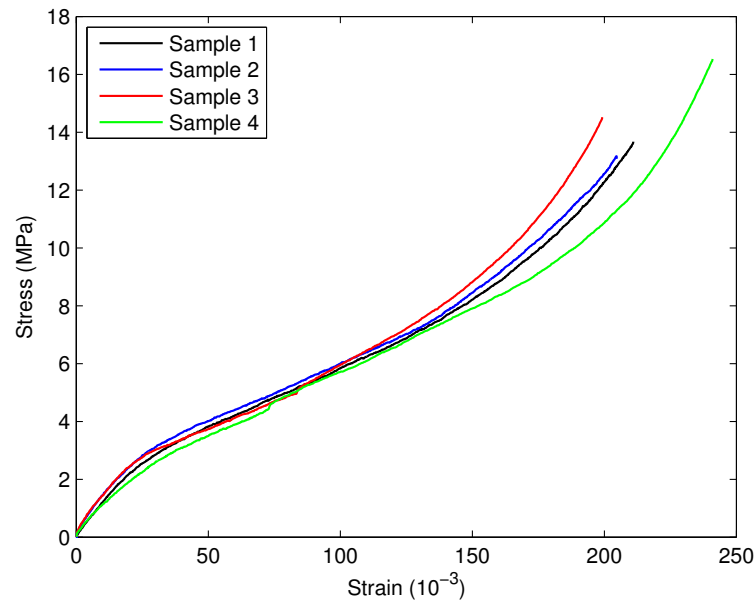
(a)  $[(0/90F)_4]$  layup(b)  $[(\pm 45F)_4]$  layup

Figure 3.9: Tensile stress-strain results for carbon fibre/elastomer laminates of two different layups.



### Flexural Testing

Testing elastomeric composites in bending is difficult because a high resolution is required for low forces, and the material test systems accessible by the author do not provide sufficient resolution for the thin laminates being investigated. The bending of these laminates is the main focus of this work, so an alternative setup is used and is presented in Section-4.4.1.

Four-point bending tests are, however, conducted on thicker [0/90] laminates to assess the onset of fibre-tow buckling. This investigation is relevant to, but not the focus of, this work. The complete analysis and results from these experiments can be found in [1].

Fibre-tow buckling is much more of a concern for a [0/90] laminate compared to [ $\pm 45$ ]. The former has a significantly higher elastic modulus, so for the same curvature the bending stress is much greater in the outer fibre tows, making them more susceptible to buckling. Secondly, the fibres are orientated in line with the direction of bending stress, whereas the [ $\pm 45$ ] fibre tows have a reduced effective end-load, which is a  $45^\circ$  component of the applied stress.

### 3.3.4 Laminate Density and Fibre Volume Fraction

The laminate fibre volume fraction,  $v_f$ , can be determined if the density of the laminate, matrix and fibres are all known. The expression for  $v_f$  is derived by starting with the sum of masses,

$$\begin{aligned} m_l &= m_f + m_m \\ &= \rho_f V_f + \rho_m V_m, \end{aligned} \quad (3.1)$$

where the  $l$ ,  $f$  and  $m$  subscripts denote the laminate, fibres, and matrix respectively. Equation (3.1) is divided by the volume of the laminate,  $V_l$ , to obtain

$$\begin{aligned} \rho_l &= \rho_f v_f + \rho_m v_m \\ &= \rho_f v_f + \rho_m (1 - v_f). \end{aligned} \quad (3.2)$$

Rearranging, the final expression is obtained as

$$v_f = \frac{\rho_l - \rho_m}{\rho_f - \rho_m}. \quad (3.3)$$

Five samples were measured and weighed, and the resulting average density of the elastomeric composite is  $1.31 \text{ g/cm}^3$ . The specified density of the elastomer is  $1.04 \text{ g/cm}^3$  with the average carbon fibre density being  $1.75 \text{ g/cm}^3$ . Therefore, the calculated fibre volume fraction is 0.38. A conservative value of 0.35 is assumed in the experimental validation in Section-4.4 to account for variations in fabrication quality and carbon fibre density.

### 3.3.5 Abaqus Material Characterization

To simulate the material behaviour accurately in Abaqus, one has to ensure that the specified material properties are in agreement with experimental data. This is not the case for a carbon fibre/elastomer laminate. It is found that CLT (which is used by Abaqus) severely underestimates the Young's modulus in the longitudinal direction,  $E_x$ , and likewise in the transverse direction, for a [ $\pm 45$ ] laminate. For such a laminate, the orthogonal in-plane elastic moduli are equivalent, so the material can be potentially

specified as isotropic. However, the limitation is that a Poisson ratio greater than 0.5 cannot be specified. Since the Poisson ratio plays a very important role in anticlastic bending effects, specifying a Poisson ratio of 0.5 is not acceptable.

Abaqus provides a material property option, known as Engineering Constants, whereby one can input directly the values for  $E_1$ ,  $E_2$ ,  $E_3$ ,  $\nu_{12}$ ,  $\nu_{13}$ ,  $\nu_{23}$ ,  $G_{12}$ ,  $G_{13}$  and  $G_{23}$ . In this case, a Poisson ratio greater than 0.5 can be specified. This option is a viable alternative, but the homogeneous nature of the material may result in inaccurate predictions of through-thickness properties. Therefore, effective elastic and shear moduli are specified for the elastomer to increase the longitudinal elastic modulus, while maintaining a high Poisson ratio close to unity. An effective elastic modulus of 14.5 MPa and effective shear modulus of 4.80 MPa for the elastomer are sufficient to achieve an overall laminate elastic modulus of  $E_x \approx 38.0$  MPa. As discussed in Section-3.3.3, the elastic modulus is bilinear, but for the purpose of the analytical investigation these linear material properties are used. There is also the option in Abaqus to input directly the stress-strain empirical data as given in Figure-3.9(b). The same issue arises with not being able to specify a Poisson ratio above 0.5. Since the transition between the two linear regions occurs at a relatively low stress, it is likely that bending stresses in excess of this are induced, when large curvatures are encountered.

Upon further investigation, it is interestingly found that the shear modulus of the matrix completely dominates  $E_x$  for a  $[\pm 45]$  laminate, according to CLT. The effective material properties can be tailored to match the properties determined from testing, since there are two layup configurations and only two variables that significantly affect  $E_x$ , namely  $E_f$  and  $G_m$ .

Section-4.2 discusses the finite element model in detail, as well as the implications of material characterization on the results of the analysis and their applicability to reality.

# Chapter 4

## Anticlastic Bending

### 4.1 Anticlastic Effects in Laminated Composite Beams

The anticlastic effect, as described in Section-2.3, causes an orthogonal curvature to the applied principal curvature in a beam or plate. This phenomenon is a result of the Poisson ratio, which is typically between zero and 0.5 for isotropic materials. This is because the shear modulus and bulk modulus must be positive to make physical sense. For example, a Poisson ratio greater than 0.5 would result in a negative bulk modulus. Since the bulk modulus is a measure of a material's resistance to volume changes when under uniform pressure, a negative value states that the material volume would increase under compression. Physically this is impossible, hence the Poisson ratio upper limit of 0.5. Note that this is only the case for isotropic materials, whereas orthotropic composite laminates can feature Poisson ratios in excess of 0.5. Therefore, an alternative anticlastic bending model is required, such as that presented by Hyer and Bhavani [20]. This chapter investigates this model and its applicability to the prediction of variable bending stiffness of composite laminates. The increase in bending stiffness in composite laminates due to anticlastic bending is yet to be characterized accurately, to the best knowledge of the author of this work. The anticlastic effect has a particularly significant impact on the effective bending stiffness of a dual-matrix laminate, which is further discussed in this chapter.

#### 4.1.1 Anticlastic Bending Governing Equation

The deflection in the  $z$ -direction of the plate's cross-section for a given longitudinal radius of curvature is governed by the fourth-order ordinary differential equation (ODE)

$$\frac{d^4 w(y)}{dy^4} + 4\beta^4 w(y) = 0, \quad (4.1)$$

where  $w$  is the displacement in the  $z$ -direction (see Figure-4.1), and

$$\beta^4 = \frac{3(1 - \nu^2)}{R_x^2 h^2}, \quad (4.2)$$

where  $\nu$  is the Poisson ratio,  $R_x$  is the longitudinal radius of curvature in the  $x$ -direction, and  $h$  is the thickness of the plate.

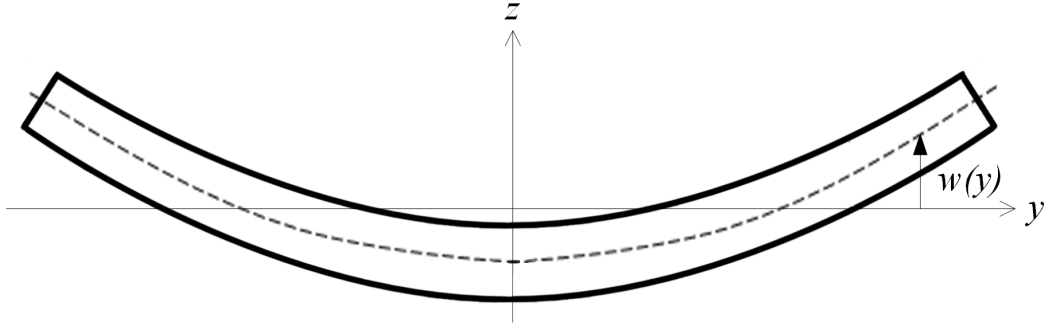


Figure 4.1: Schematic of the anticlastic deflection of the laminate cross-section, showing the  $z$ -direction deflection,  $w$ .

This governing equation presented here is in its simplest form and is only applicable to an isotropic plate. Before the theory can be applied to a composite plate it is important to define a number of variables. The well known system of equations for composite laminate analysis is given by

$$\begin{Bmatrix} N \\ M \end{Bmatrix} = \begin{bmatrix} A & B \\ B & D \end{bmatrix} \begin{Bmatrix} \epsilon \\ \kappa \end{Bmatrix}, \quad (4.3)$$

where the  $N$  and  $M$  vectors are the applied force and moment, per unit width, respectively,  $A$  is the extensional stiffness matrix,  $B$  is the coupling stiffness matrix,  $D$  is the bending stiffness matrix, and  $\epsilon$  and  $\kappa$  are the midplane strain and curvature vectors respectively. In the derivation in [20], Hyer and Bhavani present an inverted form of equation (4.3) as

$$\begin{Bmatrix} \epsilon \\ M \end{Bmatrix} = \begin{bmatrix} A^* & B^* \\ -(B^*)^T & D^* \end{bmatrix} \begin{Bmatrix} N \\ \kappa \end{Bmatrix}, \quad (4.4)$$

where

$$\begin{aligned} A^* &= A^{-1}, \\ B^* &= -A^{-1}B, \quad \text{and} \\ D^* &= D - BA^{-1}B. \end{aligned} \quad (4.5)$$

Pao [36] presents the modified governing equation for a composite plate as

$$\frac{d^4 W}{dY^4} - \left[ \frac{2B_{21}^* \lambda}{A_{22}^* D_{11}^* + B_{21}^{*2}} \right] \frac{d^2 W}{dY^2} + \frac{(h\lambda)^2}{A_{22}^* D_{11}^* + B_{21}^{*2}} W = 0, \quad (4.6)$$

where  $W = w/h$ ,  $Y = y/b$ , and

$$\lambda = \frac{b^2}{R_x h}. \quad (4.7)$$

where  $b$  is half the width of the plate. The general solution of equation (4.6) is

$$W = C_1 \sinh \alpha Y \sin \alpha Y + C_2 \cosh \alpha Y \cos \alpha Y, \quad (4.8)$$

where  $C_1$  and  $C_2$  are integration constants and

$$\alpha = \sqrt[4]{\frac{b^4}{4A_{22}^*D_{11}R_x^2}}, \quad (4.9)$$

which is obtained from [20]. The two integration constants are obtained by imposing the appropriate boundary conditions, namely that the internal bending moment and shear force at the edges of the plate (that is, at  $Y = \pm 1$ ) are zero. Substituting these boundary conditions into the appropriate derivatives of equation (4.8) yields

$$\begin{Bmatrix} C_1 \\ C_2 \end{Bmatrix} = [H]^{-1} \begin{Bmatrix} c\lambda \\ 0 \end{Bmatrix}, \quad (4.10)$$

where

$$\begin{aligned} H_{11} &= a\lambda \sinh \alpha \sin \alpha + 2\alpha^2 \cosh \alpha \cos \alpha, \\ H_{12} &= a\lambda \cosh \alpha \cos \alpha - 2\alpha^2 \sinh \alpha \sin \alpha, \\ H_{21} &= (-2\alpha^3 + a\alpha\lambda) \cosh \alpha \sin \alpha + (2\alpha^3 + a\alpha\lambda) \sinh \alpha \cos \alpha, \\ H_{22} &= (-2\alpha^3 + a\alpha\lambda) \sinh \alpha \cos \alpha - (2\alpha^3 + a\alpha\lambda) \cosh \alpha \sin \alpha, \end{aligned} \quad (4.11)$$

and

$$a = \frac{-B_{21}^*h}{A_{22}^*D_{11}^* + B_{21}^{*2}}, \quad c = \frac{-A_{22}^*D_{11}^*}{A_{22}^*D_{11}^* + B_{21}^{*2}}. \quad (4.12)$$

Now the integration constants are known and Equation (4.8) can be applied to a composite laminate under uniform bending, provided that the laminate properties (i.e. the  $A$ ,  $B$  and  $D$  matrices) are known. These can be calculated relatively easily using classical lamination theory, given that the layup configuration and ply properties are also known.

### 4.1.2 Model Verification

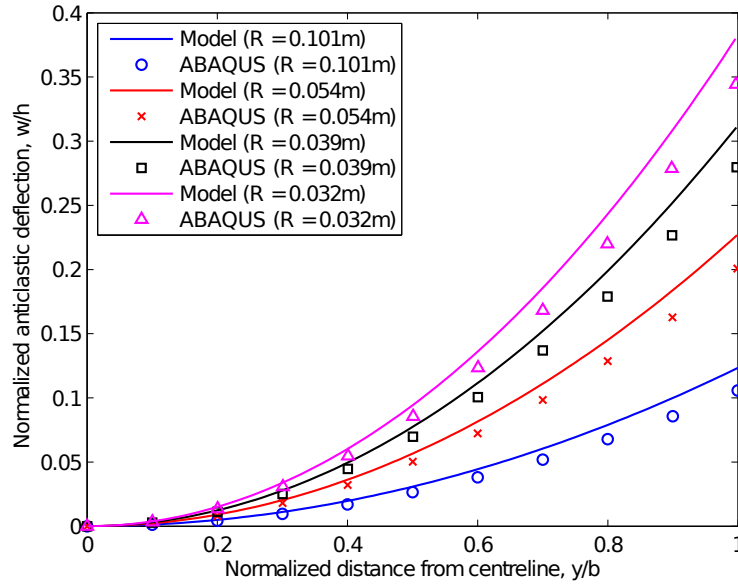
The applicability of the model is assessed by verifying the predicted anticlastic deflections of the laminate cross-section, using the commercial FEA package Abaqus/CAE (version 6.12). This section compares the anticlastic deflections from the model and from the FEM, for a range of applied curvatures. The FE model is a three-dimensional analysis utilizing shell elements with a cross-section comprised of a  $[\pm 45]_S$  composite layup with 0.25 mm lamina thickness and material properties as given in Table-4.1; Section-4.2 provides further details of the finite element model. The model exhibits close correlation to the FE results, especially for the wider laminate as shown in Figure-4.2 and Figure-4.3. The edge deflection of the narrow laminate differs from the FE results by around 10–15%. The wider laminate shows an error of approximately 10% for larger radii of curvature, while the error is less than 5% for smaller radii of curvature. The predicted deflections are less accurate when the width of the laminate is relatively small, which is most likely due to the interaction between the symmetric anticlastic deflections about the  $x - z$  plane. This theory is strengthened by the better correlation of the results for the two largest applied moments in Figure-4.2(b), where the laminate is relatively flat at its centreline (i.e. for  $Y = 0$ ), and therefore having negligible interaction between the symmetric deflections.

Table 4.1: Lamina material properties for theoretical model comparison with FE

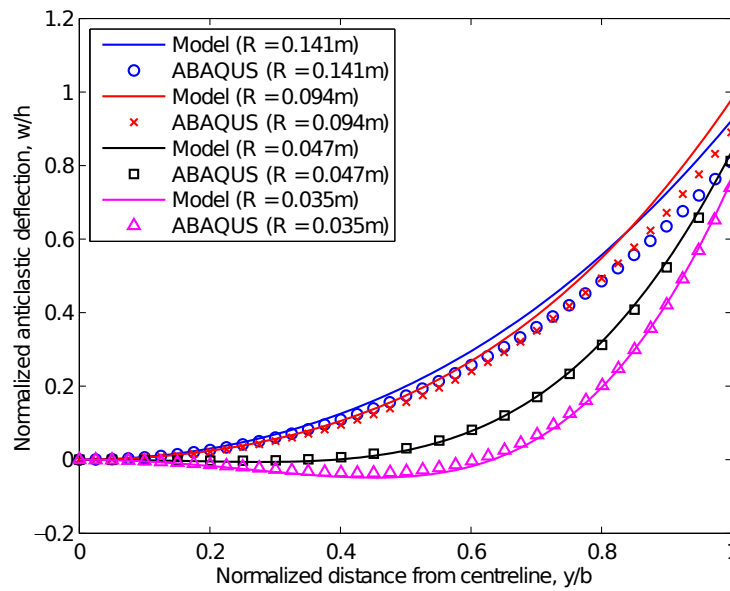
Parameter	Value
Thickness (mm)	0.25
$E_1$ (GPa)	116
$E_2$ (GPa)	4.17
$G_{12}$ (GPa)	1.59
$\nu_{12}$	0.285

### 4.1.3 Preliminary Experimental Investigation

A dual-matrix laminate is fabricated with the flexible matrix region at the midpoint along its length as seen in Figure-4.4. To demonstrate the effect of the anticlastic behaviour on the bending stiffness of a composite laminate, two dual-matrix strips of different widths are cantilevered, and the deflections compared. A 10 mm wide strip is cut out of the larger laminate as shown in Figure-4.5(a). Euler-Bernoulli beam theory suggests that the deflection of the cantilevered beam should be the same for both laminates since the ratio of the applied load (the laminate's own weight) to the second moment of area are equal for both laminates, but Figure-4.5(b) shows that the deflections differ significantly. For further analysis, a second sample is cut with a width of 20 mm, and a slit is made at the midpoint of the flexible-matrix region (see Figure-4.6(a)) to ensure that the width of each half of the flexible region is 10 mm for a fair comparison with the narrower sample. Figure-4.6(b) shows the bending stiffness comparison and it can be seen that the laminates exhibit the same deflection. This confirms that the effective bending stiffness of the laminate is highly dependent on its width, and hence the anticlastic deflection of the cross section. Figure-4.7 clearly shows the anticlastic effect occurring in the laminate for a large curvature.

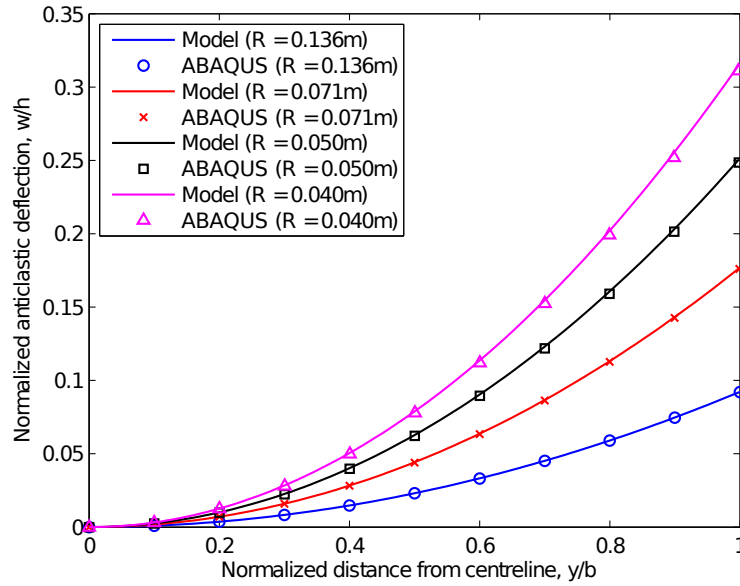


(a) Laminate width = 10 mm

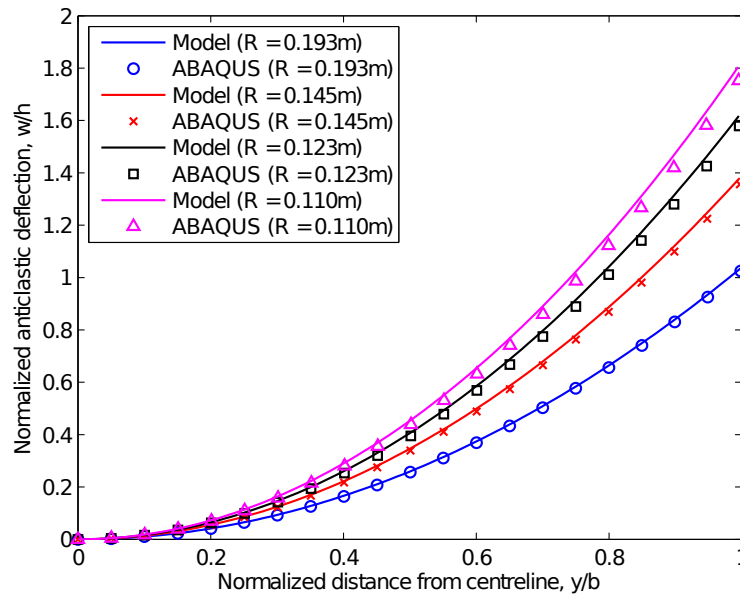


(b) Laminate width = 40 mm

Figure 4.2: Normalized anticlastic deflection for increasing longitudinal curvature for a 1 mm thick  $[\pm 45]_S$  carbon-fibre reinforced epoxy laminate.



(a) Laminate width = 10 mm



(b) Laminate width = 40 mm

Figure 4.3: Normalized anticlastic deflection for increasing longitudinal curvature for a 1 mm thick  $[\pm 45]_S$  carbon-fibre reinforced elastomer laminate.



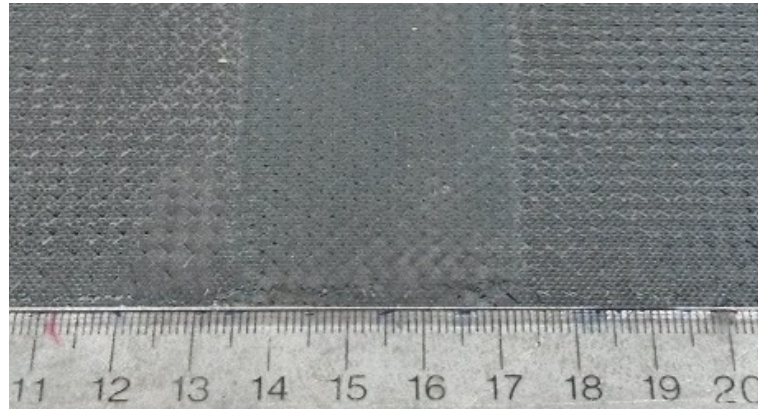


Figure 4.4: Dual-matrix laminate showing the elastomeric resin boundaries. The matrix to the left and right of the central elastomer region is epoxy.



(a) Top view



(b) Side view

Figure 4.5: Bending stiffness comparison between narrow and wide dual-matrix laminates. The thin laminate exhibits a significantly lower bending stiffness, even though the bending moment, per unit width, is identical for both laminates.



(a) Top view showing the slit



(b) Side view

Figure 4.6: Bending stiffness comparison between a 10 mm wide dual-matrix laminate and a 20 mm laminate with a slit along its centreline. The equivalent deflection provides evidence of anticlastic effects on bending stiffness.



Figure 4.7: Anticlastic effect clearly demonstrated for large curvature in a 20 mm wide dual-matrix laminate with a slit.

## 4.2 Finite Element Model

### 4.2.1 Overview

The Abaqus/Standard finite element model in this work is a three-dimensional (3D) shell analysis. Four-noded shell elements are chosen since they account for bending (which is the primary focus of this investigation) while allowing for simple management of cross section properties. The cross section is specified as a composite shell comprised of laminae of varying orientation. In addition, shell element thickness can be defined in the section properties, instead of being dependent on the 3D part itself. If 3D elements are used, the thickness needs to be discretized into multiple elements to accurately model the through-thickness behaviour. The thicknesses of the laminates being investigated are significantly smaller than the other two dimensions, thereby necessitating an excessively large number of elements and, as a result, high computational cost. Instead, shell elements with five integration points per lamina are employed. Reduced integration is chosen over full integration due to mesh-locking being encountered for full integration; this is discussed in Section-4.2.3.

### 4.2.2 Boundary Conditions and Applied Loads

Since the anticlastic curvature is the focus here, it is important to ensure that the extracted nodal deflections are not affected by any stress concentrations in the model. Initially, this is observed when a fixed translation boundary condition is applied to the edge centre node in Figure-4.8. The anticlastic deflections differ significantly to the theoretical predictions, but when the fixed boundary condition is moved to the opposite end of the geometry (see Figure-4.9), the theoretical predictions and Abaqus results are in close agreement.

To induce a bending moment in the shell, a rotation boundary condition is specified at the right-hand edge, as shown in Figure-4.10. The value of the rotation is incremented from  $\pi/8$  to  $\pi/2$  to achieve various radii of curvature, and the internal bending moment and anticlastic deflections are extracted.

### 4.2.3 Mesh Convergence and Element Selection

The shell model is beneficial in that it is virtually a 2D model (as far as computational cost is concerned), with the ability to capture the 3D behaviour of the laminate. As a result, the run times of the simulations are relatively low, so a fine mesh can be used without a significant time penalty. However, it is still valuable to conduct a mesh convergence study for assurance. This analysis is conducted for a 50 mm wide elastomeric laminate of  $[(\pm 45)_2]_S$  layup with an applied radius of curvature of approximately 0.2 m.

There are two ways to extract the internal bending moment in the shell. The first is to determine the reaction moment (RM) at the zero-rotation boundary condition in Figure-4.8, and the total reaction moment is obtained by summation of the nodal RM values along the edge. The second method is to extract the maximum section moment (SM), which is found at the centre of the plate. SM is a distinct value which, when multiplied by the width of the laminate, provides the internal bending moment in the plate. Realistically, these values should be equal but Abaqus yields different results, especially for full integration, as seen in the mesh convergence results in Figure-4.11. This is expected since SM is a unique value while RM is cumulative for all the nodes, so the errors at each node are compounded during summation. The two parameters show evidence of convergence for finer meshes.

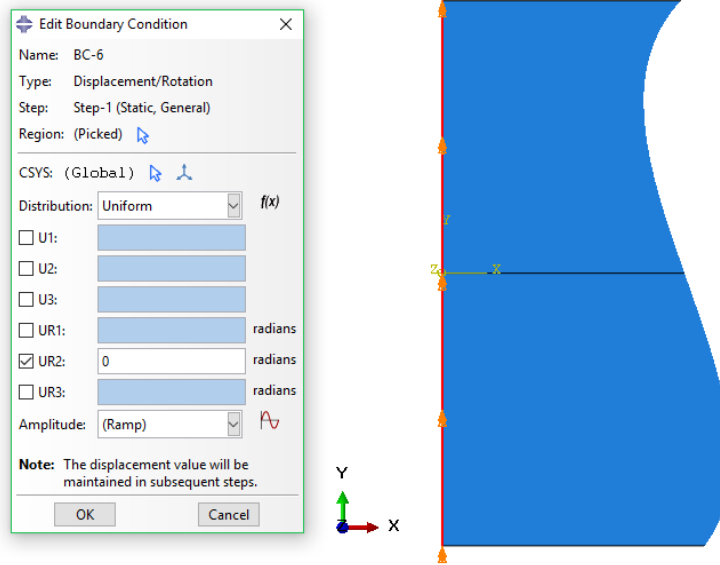


Figure 4.8: Zero-rotation boundary condition ( $UR2 = 0$ ) applied to the edge at which the anticlastic deflections are extracted. All other degrees of freedom must be unconstrained to ensure that the anticlastic deflections are free from influence.

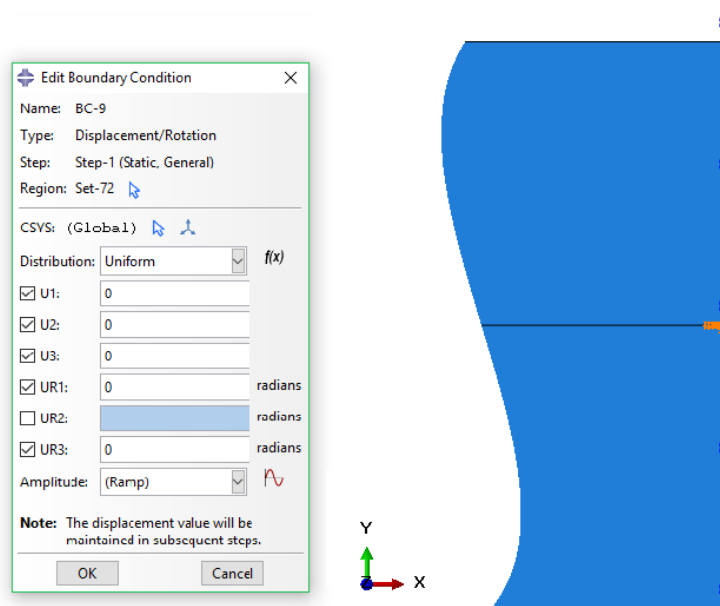


Figure 4.9: Fixed boundary condition applied to the centre node on the opposite edge of the laminate, allowing only UR2 rotation to facilitate the applied rotation for inducing curvature in the laminate.

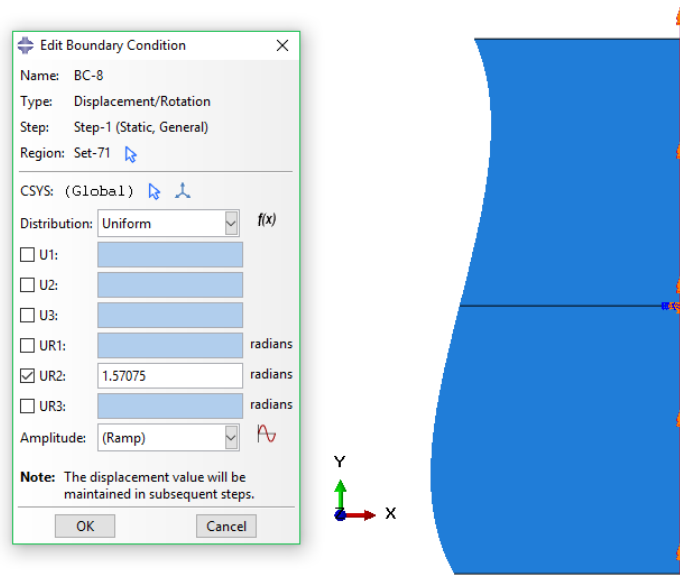


Figure 4.10: Applied rotation (UR2) to right-hand edge to induce a constant curvature in the laminate.

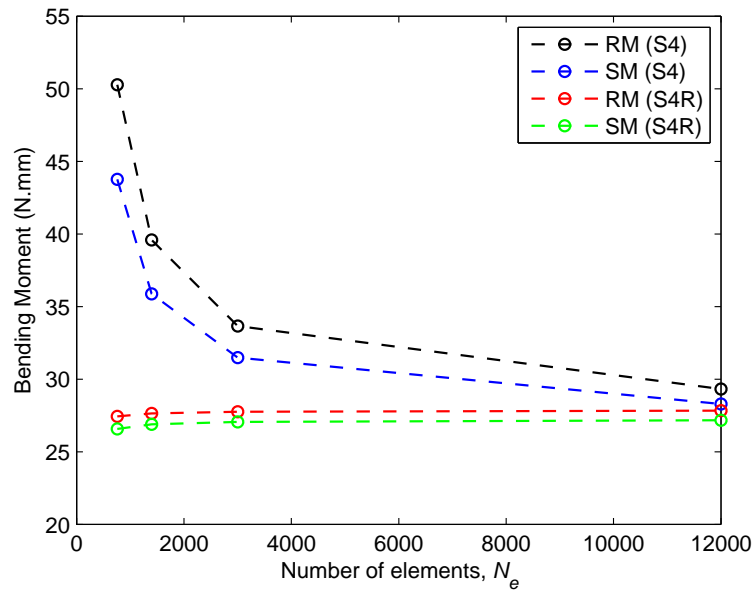


Figure 4.11: Mesh convergence for reaction and section internal moment for shell elements with full integration (S4) and reduced (S4R) integration

Coarse meshes with full integration exhibit mesh-locking, thereby over-estimating the internal bending moment. The reduced integration element converges significantly faster than the full integration element. There is a 2.2% difference in bending moment for the S4R element between 760 and 12,000 elements, while the S4 element shows a 55% difference. Furthermore, the run times for the S4R element are shorter compared to the S4 element, as shown in Table-4.2, although the simplicity of the analysis allows short run times in general, even for the full integration element.

The anticlastic deflections are also considered in this study, and it is found that the percentage difference between the theoretical predictions and the Abaqus results is no more than 1.6%, independent of the mesh fineness for both the S4 and S4R elements.

In conclusion, the S4R element is superior for this model, and is therefore used throughout. The exact number of elements in the model is geometry dependant in the numerous simulations for various laminate dimensions. Between 2000 and 4000 elements, corresponding to 20 or 40 elements across the width of the laminate are used. This provides sufficient accuracy with the simulation run time never exceeding 120 seconds.

#### 4.2.4 Abaqus Limitations

The model used in this analysis has certain limitations that can potentially affect the results, the main limitation being the section definition of the composite layup. Abaqus does not provide an option for woven-fabric composites; instead, the laminae are all unidirectional. The closest approximation to the woven-fabric laminates used in this work is to specify a symmetric unidirectional layup of alternating orientations, i.e.  $[(\pm 45)_2]_S$ . However, the behaviour of laminates of this orientation is highly dominated by shear, for which there is expected to be a significant difference between woven-fabric and unidirectional laminae. Figure-4.12 provides evidence of this with large discontinuities in strain between lamina. It is important to note the  $x$ -axis scale difference between Figure-4.12(a) and Figure-4.12(b); the shear strain,  $LE_{12}$ , is almost three orders of magnitude larger than the normal strain,  $LE_{11}$ . This confirms that shear is the dominant strain. The seemingly large discontinuities in Figure-4.12(b) are a result of the shear in each lamina being in the opposite direction to the adjacent laminae. Upon closer inspection, it can be seen that the magnitude of the shear strain across subsequent laminae is continuous, but of opposite sign. This shear strain distribution is expected to look entirely different for a woven fabric laminate, since there is interaction between the interwoven fibre tows of perpendicular orientation.

A common method in Abaqus for modelling reinforced concrete is to use rebar layers. It is possible to apply this to a woven composite analysis, where a rebar layer is specified within each lamina, with the rebar “fibres” being oriented perpendicular to the lamina orientation. However, this is also limited because it does not take into account the interaction of the two layers. Many authors have modelled the properties of woven fabrics, although most of the research has been conducted at the microlevel

Table 4.2: Convergence study details and simulation run times.

Mesh	Coarse	Medium	Fine	Finest
$N_e$	760	1,400	3,000	12,000
Element size (mm)	4	3	2	1
Run Time, S4 (s)	80	126	235	988
Run Time, S4R (s)	48	54	100	362

by modelling repeating unit cells of overlapping fibre tows. The overall behaviour of the laminate is of interest here, so modelling at the microlevel is impractical. The only alternative is to modify the stiffness matrices in Abaqus. Raju and Wang [38] present modified CLT models for various weave patterns. These models can be used in the FEM to better predict the behaviour of woven composites. This is outside the scope of this thesis and has been recommended as essential for future development of this work in Chapter-6.

Alternatively, a user-defined material can be created in Abaqus where the material properties of woven composites are input directly, including Poisson ratios of greater than 0.5. This is worth considering as a viable alternative to using Abaqus' composite section option in future work.

Another important piece of information obtained from Figure-4.12(b) is the maximum principal strain, overlaid to show the similar magnitude relative to the shear strain, which is expected. Furthermore, the point of zero principal strain coincides with the point of zero shear strain. This indicates the location of the neutral axis of the cross-section.

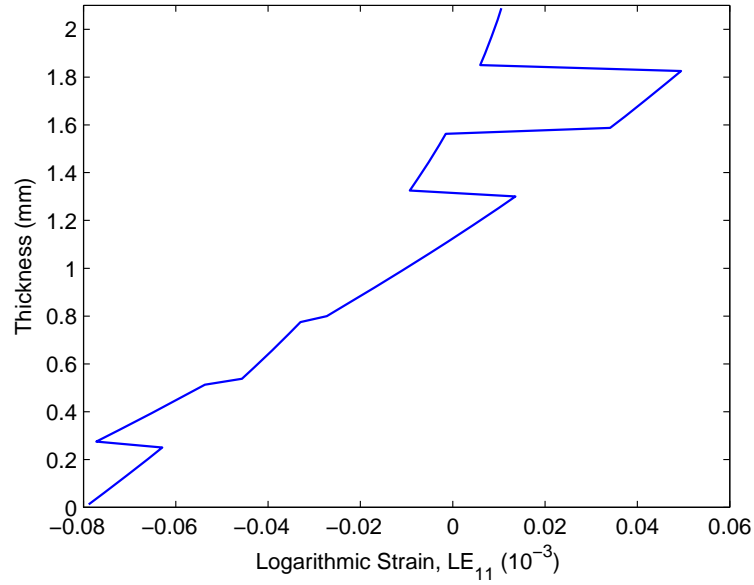
### 4.3 Increase in Bending Stiffness Due to Anticlastic Effects

The anticlastic effect can result in a significant change in the geometry of the cross section of the laminate. Therefore, the second moment of area of the cross section increases as the laminate undergoes some curvature in the longitudinal direction. During bending, the convex surface experiences a tensile stress while the concave surface is in compression, which is very well known for bending of plates and beams. In the case of a  $[\pm 45]$  carbon-fibre reinforced elastomer, the longitudinal elastic modulus is non-linear as shown in Section-3.3.3. However, this non-linearity is most prominent for relatively large strains, where the fibre orientations begin to change significantly without failure, possible due to the high strain capability of the matrix material. In the case of bending, it is assumed that the strains are small enough that the elastic modulus is constant. Therefore, the change in bending stiffness,  $EI$ , of the plate is assumed to be solely dependent on the second moment of area,  $I$ , which is discussed in subsequent sections. The elastic modulus in this case is the effective extensional stiffness of the laminate in the longitudinal direction,  $E_x$ . The second moment of area is calculated with respect to the  $y$ -axis.

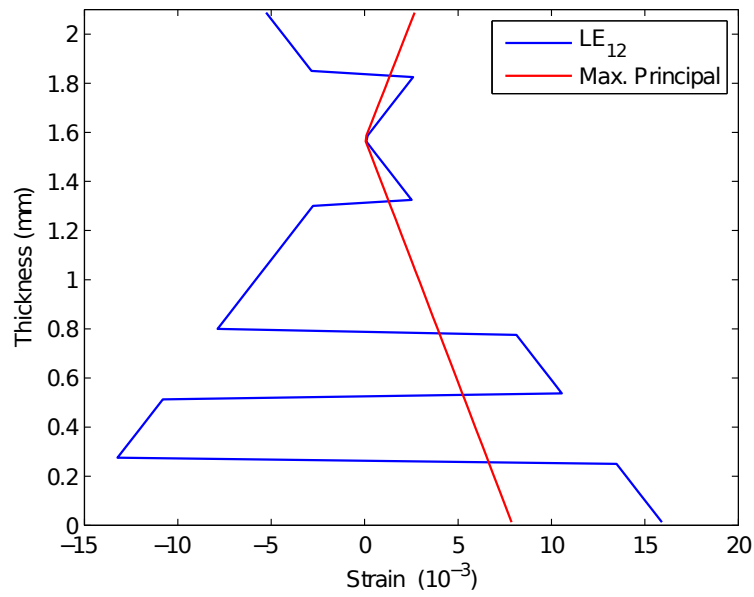
#### 4.3.1 Bending Moment

Hyer and Bhavani [20] derive an expression for the longitudinal moment,  $M_x$ , for a given longitudinal radius of curvature,  $R_x$ . However, the expression presented in their work yields highly inaccurate results, compared to the FE results for the applied moment. It is assumed that the expression is incorrectly presented since the authors experimentally validate their model, so their moment model is not used in this work, whereas their anticlastic deflection model is used, as it has been shown to provide accurate predictions. According to Hyer and Bhavani, the applied moment is given by

$$M_x = \frac{-h^2 b \mu}{8\alpha R_x A_{22}^*} - 2 \left( \frac{D_{12} h \alpha \gamma}{b} + \frac{D_{22} b}{R_x} \right), \quad (4.13)$$



(a)  $x$ -direction normal strain



(b) Shear strain with superimposed maximum principal strain

Figure 4.12: Abaqus output for through-thickness logarithmic strains of a  $[(\pm 45)_2]_S$  elastomeric laminate at the integration points (five per lamina).



where

$$\begin{aligned}\mu &= [2(C_2^2 - C_1^2)(\sinh 2\alpha + \sin 2\alpha) + 4\alpha(C_2^2 - C_1^2) \\ &\quad + (C_2^2 - C_1^2 + 2C_1C_2) \cosh 2\alpha \sin 2\alpha \\ &\quad + (C_2^2 + C_1^2 - 2C_1C_2) \sinh 2\alpha \cos 2\alpha], \\ \gamma &= (C_1 + C_2) \sinh \alpha \cos \alpha + (C_1 - C_2) \cosh \alpha \sin \alpha.\end{aligned}\tag{4.14}$$

Equation-4.13 and Equation-4.14 are modified from the lengthy equations obtained in [20] by deleting terms that equate to zero in this analysis as well as modifying the variable names to match those defined in this work. Hyer and Bhavani account for initial radii of curvature,  $R_{x_0}$  and  $R_{y_0}$ , which are assumed to be infinitely large here; these parameters are in the denominator in a number of terms thereby reducing those terms to zero.

In this current work, the laminate is approximated as a homogeneous material with constant elastic modulus and a large Poisson ratio, close to unity. Therefore, the bending stiffness of the laminate can be approximated using the elementary beam theory equation

$$EI = \frac{M}{\kappa},\tag{4.15}$$

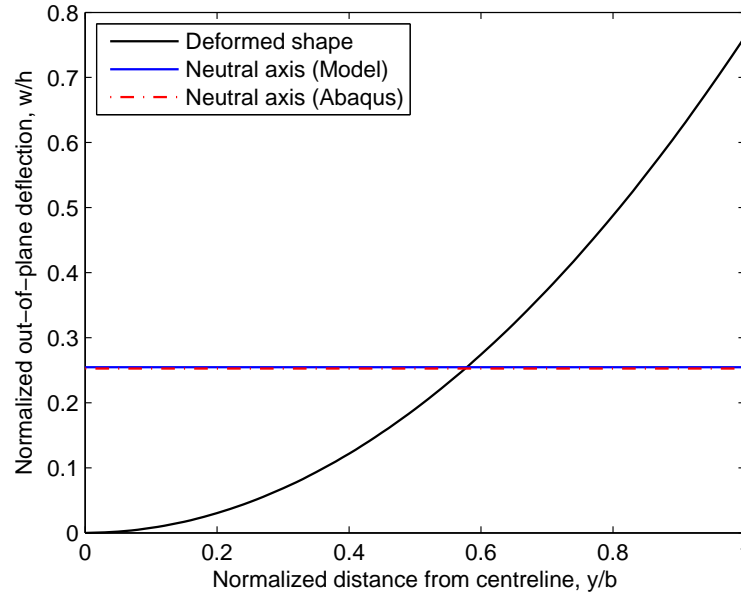
where  $M$  is the internal bending moment and  $\kappa$  is the curvature of the beam; for pure bending of a beam with uniform cross section,  $\kappa$  is constant. So long as the  $M$  and  $\kappa$  are known (these can be measured experimentally or extracted from the FEM), the bending stiffness can be obtained and compared with theoretical predictions.

### 4.3.2 Shift of the Cross Section Neutral Axis

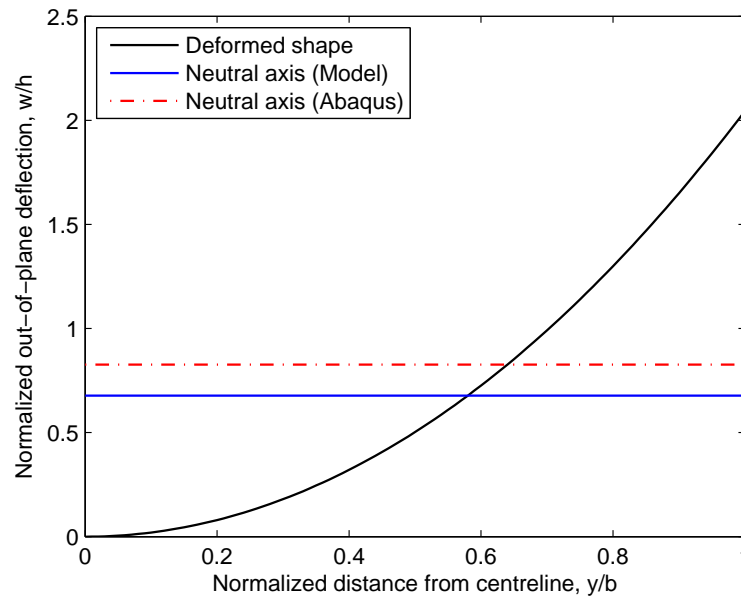
Despite the laminate in this instance being initially straight, some of the curvatures experienced are large enough for it to be considered a curved beam. In a curved beam, the neutral axis is normally shifted toward the concave side of the beam, however the neutral axis in the composite laminate moves toward the convex side due to the anticlastic effect. This is most prominent in wider laminates, as shown in Figure-4.13.

The discrepancy in the neutral axis location increases with increasing curvature so the maximum curvature evaluated is presented here. To the best knowledge of the author, this discrepancy between FE and theory has not previously been characterized. It is found that the neutral axis distance is a linear function, with respect to the longitudinal curvature of the laminate. Figure-4.14 shows this relationship, comparing the Abaqus results with the model predictions. Fitting a first order polynomial to each of the data sets reveals that the curve passes through, or at least close to, the origin in all cases, which is expected since the neutral axis does not shift for zero applied curvature. Figure-4.14(a) shows that for narrow laminates, the results from Abaqus and the model coincide, independent of curvature. The same relationship is exhibited for even narrower laminates. Wider laminates exhibit a large discrepancy for the neutral axis shift, which may be a consequence of transition to wide-beam anticlastic behaviour.

Another explanation for a shift in the actual neutral axis is that the compressive and tensile elastic moduli may not be equal. As introduced in Section-3.3.3, elastomeric composites have been shown to have a lower compressive modulus than that in tension. As a result, the neutral axis shifts to maintain equilibrium of forces and moments, and since the concave side is in compression, the neutral axis shifts

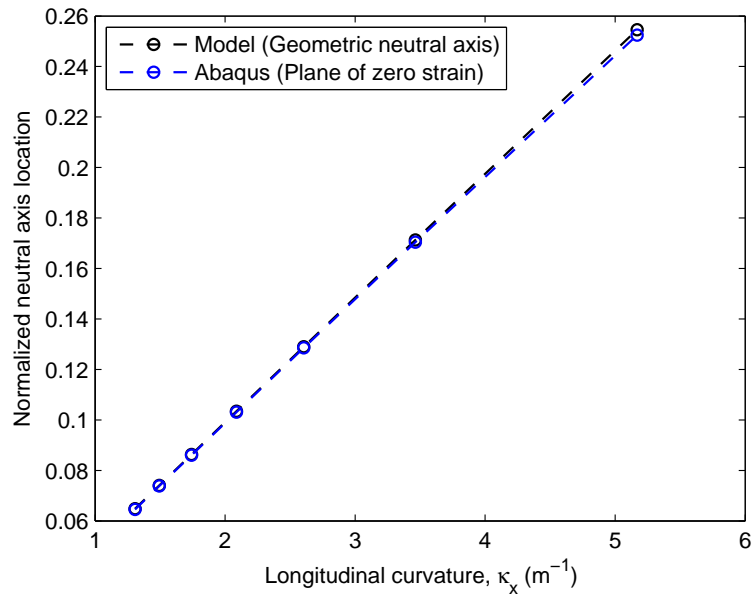


(a) Laminate width = 50mm,  $\kappa_x = 5.17 \text{ m}^{-1}$

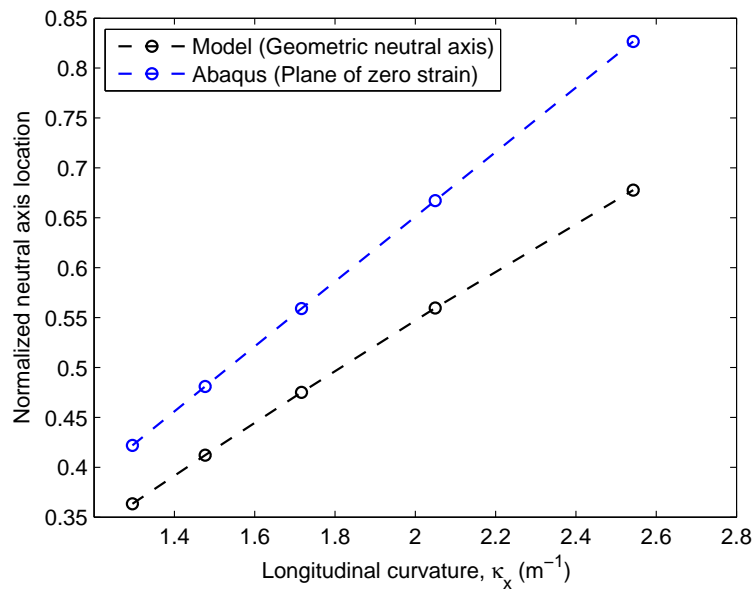


(b) Laminate width = 120mm,  $\kappa_x = 2.54 \text{ m}^{-1}$

Figure 4.13: Neutral axis comparison between Abaqus (plane of zero strain) and the model (geometric neutral axis) for 50 mm and 120 mm wide  $[(\pm 45)_2]_S$  laminates.



(a) Laminate width = 50mm



(b) Laminate width = 120mm

Figure 4.14: Comparison of neutral axis location for increasing longitudinal curvature for 50 mm and 120 mm wide  $[(\pm 45)_2]_S$  laminates. The neutral axis shift is normalized with respect to the laminate thickness (2.1 mm), where zero on the vertical axis is the mid-plane of the laminate.

towards the convex side. However, this explanation is only valid if the material properties are modelled as such. In experiments this is certainly true, but in an analytical or FE model, where the material properties are constant, this will not be the case. In this work, the neutral axis shift is first noticed in the finite element model (seen in Figure-4.12(b)), which makes this phenomenon all the more interesting since the different elastic moduli are not modelled in Abaqus.

### 4.3.3 Determination of the Second Moment of Area

Provided the thickness of the laminate is relatively small such that  $t \ll 2b$ , the anticlastic bending has a significant effect on the second moment of area of the laminate cross-section. Furthermore, the increase in bending stiffness is non-linear as the curvature increases. The integral for calculating the second moment of area of a section in the  $y - z$  plane, as depicted in Figure-4.15, is given as

$$\begin{aligned} I_y &= \int_A z^2 dA \\ &= \int_z \int_y z^2 dy dz. \end{aligned} \quad (4.16)$$

Supposing the width,  $l$ , of the elemental area is defined in terms of  $z$  as shown in Figure-4.15(b), the calculation of the second moment of area becomes simplified. Fenner and Reddy [15] define the second moment of area of the section as

$$I_y = \int_{z_1}^{z_2} z^2 l(z) dz. \quad (4.17)$$

The section in this work is discretized in  $y$  instead of  $z$ , so  $l$  is now a function of  $y$  (see Equation-4.8), and the integral is modified accordingly. The limits become  $y_1$  and  $y_2$ , and the variable of integration is substituted according to the relation

$$\begin{aligned} z &= f(y), \\ dz &= f'(y) dy, \\ &= \phi(y) dy, \end{aligned} \quad (4.18)$$

where,  $\phi(y)$  is the slope of cross-section. The element width is defined as

$$l(y) = \frac{h}{\sin \phi(y)}. \quad (4.19)$$

Thus, the integral now becomes

$$I_y = 2h \int_0^b \frac{[w(y)]^2 \phi(y)}{\sin(\phi(y))} dy. \quad (4.20)$$

The integral is multiplied by two because  $I_y$  is calculated with  $y \in [0, b]$  since the cross section is symmetric about the  $z$ -axis. Due to the complexity of the integral, especially since  $w$  and  $\phi$  are functions of trigonometric and hyperbolic functions, the closed form solution cannot be determined. The integral is therefore calculated numerically for the cross-section using the trapezoidal method.

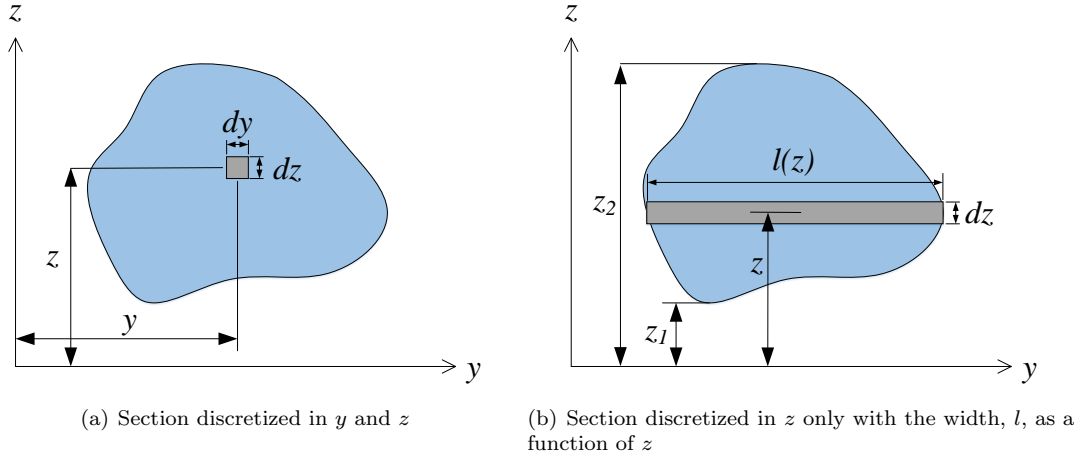


Figure 4.15: Elemental area for an arbitrary cross section for determination of the second moment of area.

### 4.3.4 Bending Moment Verification and Increase in Bending Stiffness

#### Abaqus Verification

For the purpose of verifying the bending moment model, the material properties of the laminate do not need to match the experimental results in Chapter-3. However, there needs to be consistency between the FEM and analytical model material characterization. The material properties in this analysis are defined as described in Section-3.3.5 to achieve an effective elastic modulus of 38 MPa, and are listed in Table-4.3.

Figure-4.16 through Figure-4.18 show the results for 2.1 mm thick  $[(\pm 45)_2]_S$  laminates for widths of 30 mm, 50 mm and 120 mm, respectively. These widths correspond to three data sets obtained through experiments. The purpose of this is to assess the accuracy of the model, with respect to Abaqus, for subsequent comparison with the experimental results. The results here show that the model over-predicts the bending stiffness of the laminate for narrow laminates ( $\leq 30$  mm width). The model correlates well with the FE results for wider laminates ( $\geq 50$  mm width) as seen in Figure-4.17. However, the 50 mm and 120 mm results show that the model is more accurate for smaller curvatures, while the results begin to diverge for larger curvatures.

As the width of the laminate increases, higher-order polynomials are required to model the trend of the FE results accurately, as seen in Figure-4.19 through Figure-4.21 for the 1 mm thick laminate. These trend lines are only applicable over the range of curvatures shown here, and should not be used

Table 4.3: Material specifications of carbon fibre, elastomer, and lamina with a fibre volume fraction of 0.5, for use in the bending moment verification of 1 mm thick,  $[\pm 45]_S$  laminates.

Material	Carbon Fibre	Elastomer	Lamina ( $v_f = 0.5$ )
$E_1$ (GPa)	230	0.015	115
$E_2$ (GPa)	–	–	0.029
$\nu_{12}$	0.27	0.49	0.38
$G_{12}$ (GPa)	50	0.005	0.0096

for predicting bending moments outside this range. They are for the purpose of demonstrating that the bending stiffness is not constant. The non-linearity of the results shows that there is an increase in the bending stiffness of the laminate for increasing curvature, as expected. For wider laminates, the prediction of bending moment from the analytical model diverges from the FE solution. This is likely due to the transition from narrow- to wide-beam theory for the anticlastic effect. The bending stiffness of the laminate is no longer purely a function of the second moment of area, since additional stiffness is introduced due to the anticlastic curvature being constrained.

The applicability of the analytical model depends on the expected curvatures for a given application. As long as the curvatures are not excessively large, the bending stiffness can be predicted with suitable accuracy.

### Increase in Bending Stiffness

Figure-4.22 and Figure-4.23 show the increase in bending stiffness due to anticlastic bending. Based on the analytical model, the increase in bending stiffness is greater for thinner laminates than for thicker laminates, for the same dimensions and curvature. For example, the bending stiffness of a 40 mm wide, 1 mm thick laminate increases by a factor of 5 for  $\kappa_x=10 \text{ m}^{-1}$ , while only a factor of 2 for the 2 mm laminate. This is due to the thicker laminate exhibiting smaller anticlastic deflections, in addition to its zero-curvature bending stiffness being significantly larger (by a factor of 8).

The increase in bending stiffness is larger for wider laminates, which is to be expected as the deflections are larger compared to narrower laminates. However, for very wide laminates (>60 mm) exposed to large curvatures, the bending stiffness begins to plateau, as seen in Figure-4.23. This is due to the wide-beam theory coming into effect. As the curvature increases, the central region of the laminate flattens, thus the rate of increase in second moment of area reduces. These large curvatures are impractical as it is found that the laminate is damaged (due to fibre tow buckling - see Section-4.4.3) long before these curvatures are obtained, and the laminate bending stiffness reduces after buckling occurs.

Other laminate layups have lesser increase in bending stiffness since the anticlastic effect is maximized with this  $[\pm 45]$  layup.  $(EI)_0$  increases rapidly as the orientation approaches  $0^\circ$ , so the morphing capability is significantly impaired. Conversely, if the layup approaches  $90^\circ$ ,  $EI_0$  becomes extremely small and the laminate is too flexible;  $E$  approaches the low elastic modulus of the elastomer. Either of these scenarios reduce the Poisson ratio of the laminate, compared to the  $[\pm 45]$  layup. Certain applications may require a larger or smaller  $EI_0$  with acceptable limitations on curvature and bending stiffness increase. The characterization of this bending stiffness increase provides a simple yet accurate method for predicting the bending behaviour of elastomeric composites.

### 4.3.5 Effects on Bending Stiffness Due to Dual-Matrix Interaction

The preliminary experimental investigation discussed in Section-4.1.3 shows that the interaction between the rigid and flexible regions causes a perceived stiffness increase in the flexible region, close to the interface. A finite element analysis is conducted to determine the distance from the interface at which the flexible region is no longer affected by the rigid region. The rigid region is assumed to be a fixed boundary condition, and modelled as such in the FEM. An encastre (all degrees of freedom constrained) boundary condition is applied to the same edge shown in Figure-4.8. The anticlastic deflections are compared at increasing distances from the fixed edge. The distance at which the deflections match

the theoretical predictions is considered to be the point where the flexible region is unaffected by the dual-matrix interaction. Table-4.4 provides the results of this analysis. The analysis is conducted for four geometries, that is, widths of 10 mm and 20 mm each with layups of  $[\pm 45]_S$  and  $[(\pm 45)_2]_S$ . A range of curvatures for each geometry is applied to assess whether the distance is independent of curvature. It is found that there is a negligible difference for increasing curvature.

Table-4.4 shows that the ratio of the distance to the width increases slightly as the width increases. Conversely, this ratio reduces for thicker laminates. This is because the thicker laminates exhibit smaller anticlastic deflections compared to thin laminates, so the anticlastic bending is less constrained. Based on this analysis, as long as the length of the section is greater than 2.5 times the width, the anticlastic effect is unconstrained at the midpoint of the section. However, the behaviour of the section is still affected by the interaction at its ends, but the impact of this diminishes as the length is increased and/or slits are made in the section.

Table 4.4: Dual-matrix interaction effects for different laminates

Layup	$[\pm 45]_S$		$[(\pm 45)_2]_S$	
Width (mm)	10	20	10	20
Distance (mm)	24	50	20	48
Distance/Width	2.4	2.5	2	2.4

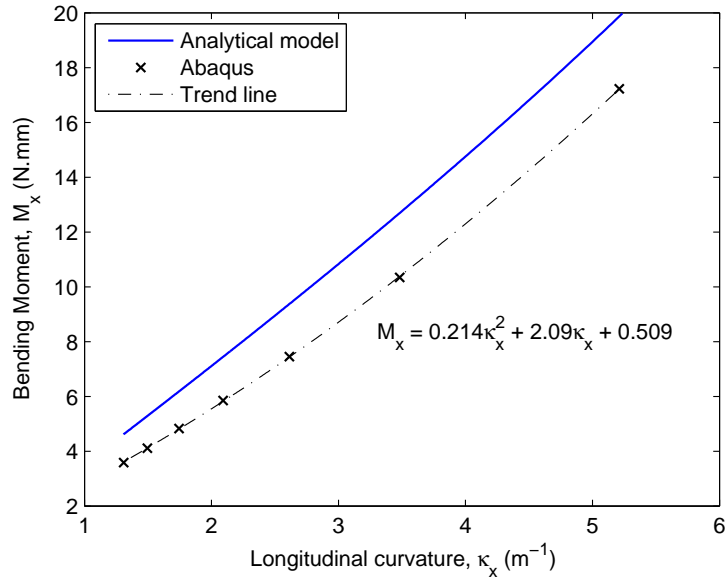


Figure 4.16: Applied bending moment required for increasing longitudinal curvature of a 30 mm wide, 2.1 mm thick laminate, with a  $[(\pm 45)_2]_S$  layup.

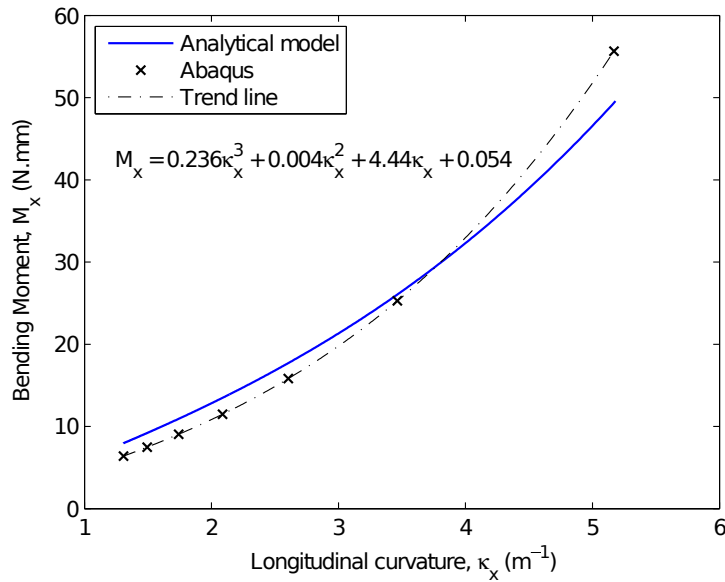


Figure 4.17: Applied bending moment required for increasing longitudinal curvature of a 50 mm wide, 2.1 mm thick laminate, with a  $[(\pm 45)_2]_S$  layup.



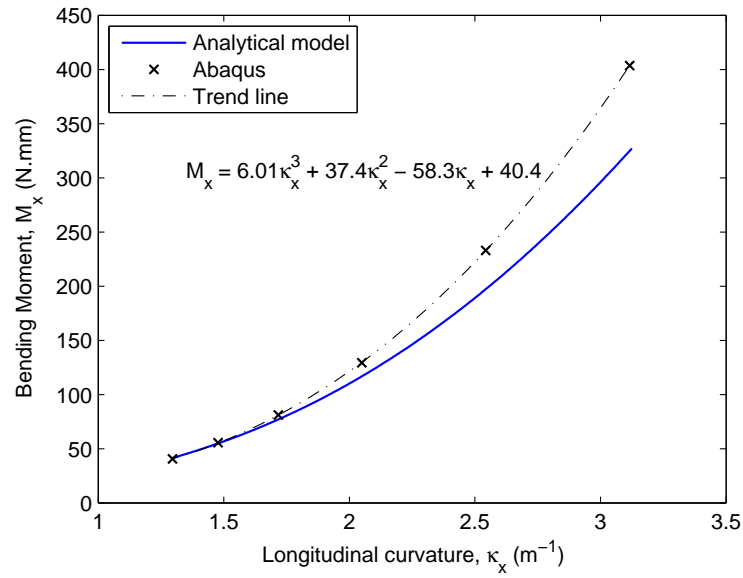


Figure 4.18: Applied bending moment required for increasing longitudinal curvature of a 120 mm wide, 2.1 mm thick laminate, with a  $[(\pm 45)_2]_S$  layup.

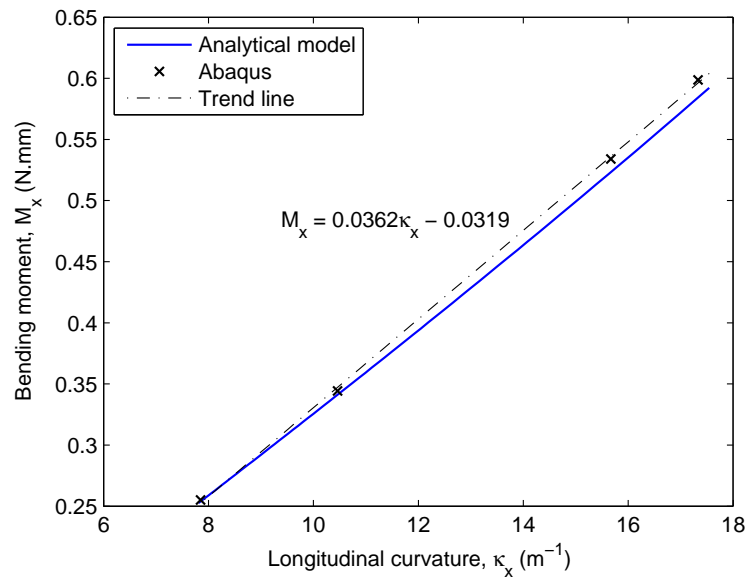


Figure 4.19: Applied bending moment required for increasing longitudinal curvature of a 10 mm wide, 1 mm thick laminate, with a  $[(\pm 45)_2]_S$  layup.

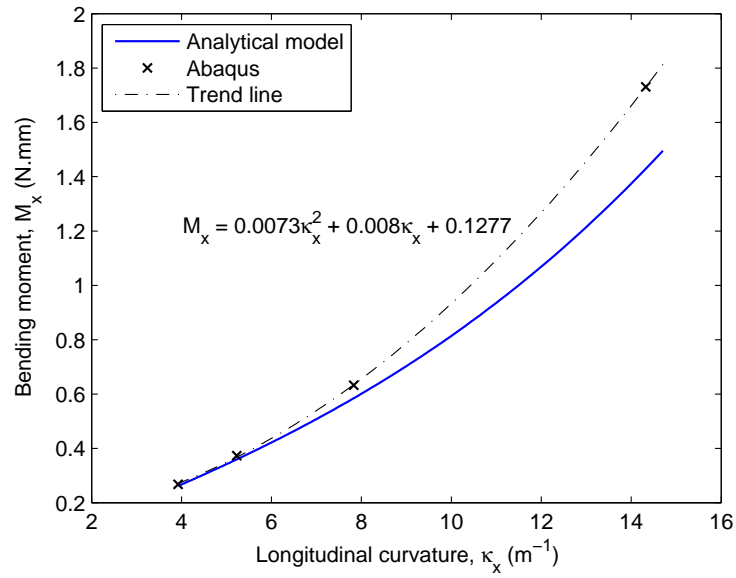


Figure 4.20: Applied bending moment required for increasing longitudinal curvature of a 20 mm wide, 1 mm thick laminate, with a  $[\pm 45]_S$  layup.

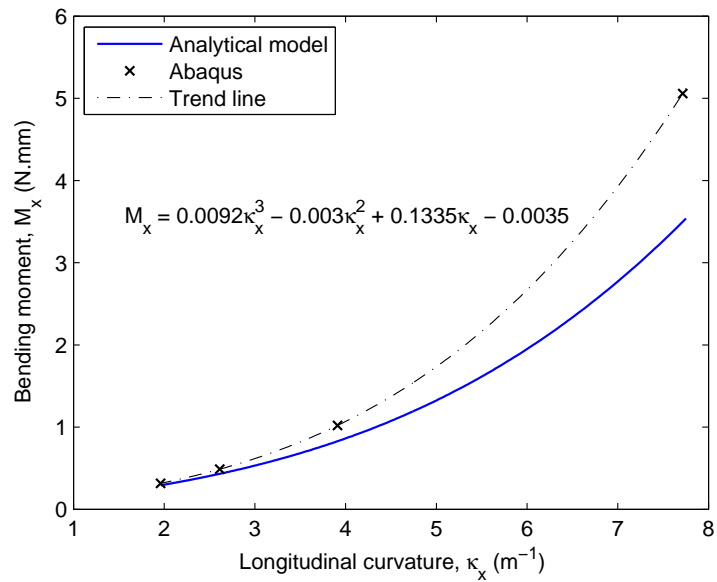


Figure 4.21: Applied bending moment required for increasing longitudinal curvature of a 40 mm wide, 1 mm thick laminate, with a  $[\pm 45]_S$  layup.

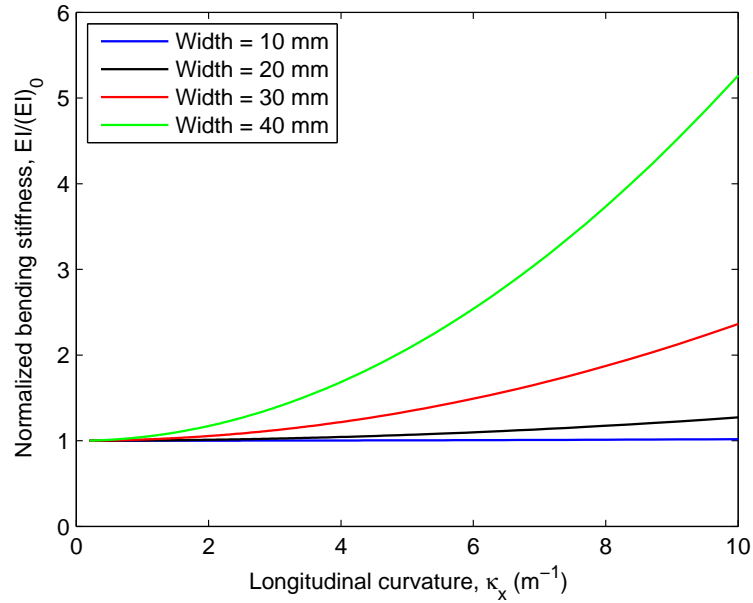


Figure 4.22: Normalized bending stiffness for increasing longitudinal curvature for 1 mm thick,  $[\pm 45]_S$  laminates of different widths. Wider laminates exhibit significant increase in bending stiffness compared to narrow laminates.

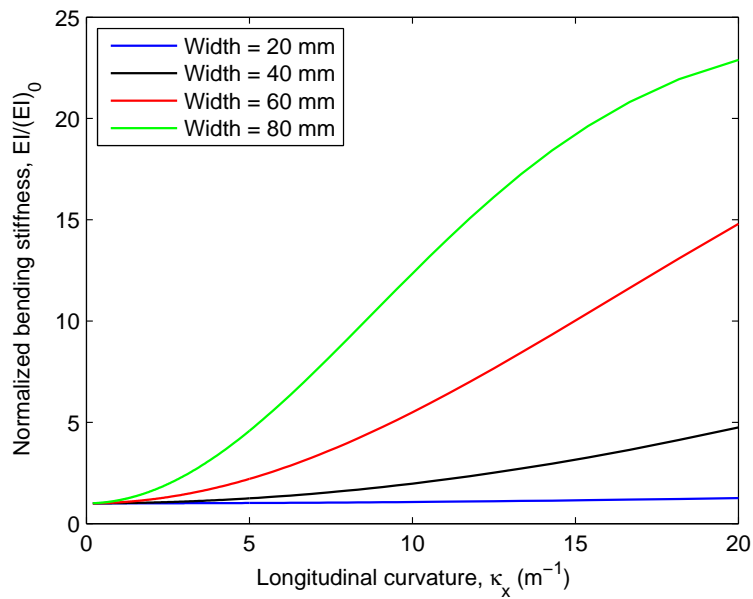


Figure 4.23: Normalized bending stiffness for increasing longitudinal curvature for 2.1 mm thick,  $[(\pm 45)_2]_S$  laminates of different widths. Wider laminates exhibit significant increase in bending stiffness compared to narrow laminates.

## 4.4 Experiments

Four-point bending tests are conducted on a  $[(\pm 45F)_8]$ , carbon fibre/elastomer laminate to validate two theories. First, the anticlastic displacement is experimentally determined and compared to the theoretical model. Second, the relationship between the curvature and applied moment is also investigated for comparison. Only a 2.1 mm thick laminate is tested because thinner laminates exhibit impractically high compliance. Thicker laminates are also ruled out due to manufacturing constraints; the short gel time of the elastomer results in a non-uniform laminate since the bottom layer gels before the top layer has been applied.

The laminate width is decremented for each subsequent test to gather as much information as possible about the behaviour of the laminate for different widths. This setup enables the collection of a large data set without having to manufacture multiple samples. The stresses and strains encountered in the laminate during the experiments are sufficiently low (calculations are conducted in Section-4.4.2) for the residual effects to be considered negligible, thereby justifying the use of the same laminate for all the experiments. The laminate widths that are investigated are 100, 80, 70, 60, 50, 40, and 30 millimetres.

### 4.4.1 Experimental Setup

Use of the MTS setup to conduct the four-point bending experiments is impractical, since the 100 kN load cell has a resolution of 10 N, which is too large for the expected loads. Using the same bending rig, an alternate experiment is designed and is shown in Figure-4.24. The camera captures the anticlastic curvature of the test sample.

The radius of curvature of the laminate is calculated using the output from the laser distance sensor. The test sample is assumed to have a constant curvature as a result of the four-point setup. The radius is determined from the equation

$$R_x = \frac{H}{2} + \frac{W^2}{8H}, \quad (4.21)$$

where  $H$  and  $W$  are defined in Figure-4.25. The assumption of a constant radius is an approximation, given that the horizontal components of the reaction force,  $F_R$ , as well as the distributed weight of the laminate,  $q$ , induce a moment. The moment induced in the laminate by the horizontal force is negligible compared to the moment due to the vertical load, so it is acceptable to ignore its contribution. The mass of the laminate is taken into account when calculating the applied moment. The masses used for the applied force,  $F$ , are comprised of various combinations of 45g, 24g, 11g, and 5g mass pieces.

The applied moment at the centre of the test sample is given by

$$M_{app} = Fd + \frac{q}{2} \left( d^2 - \frac{W^2}{4} \right), \quad (4.22)$$

where the parameters are defined in Figure-4.25. Pictures are also taken from the side of the sample (same view as in Figure-4.25) to experimentally obtain the value of  $d$ , since it decreases as the deflection increases.

The masses are placed inside a container, which is hung from the end of the laminate using wire to ensure that the force acts downward. The container is secured to the laminate by a bolt with an oversized washer to distribute the load as much as possible. Even though the load application is relatively concentrated, St. Venant's principle states that further away from the point of load application, the load

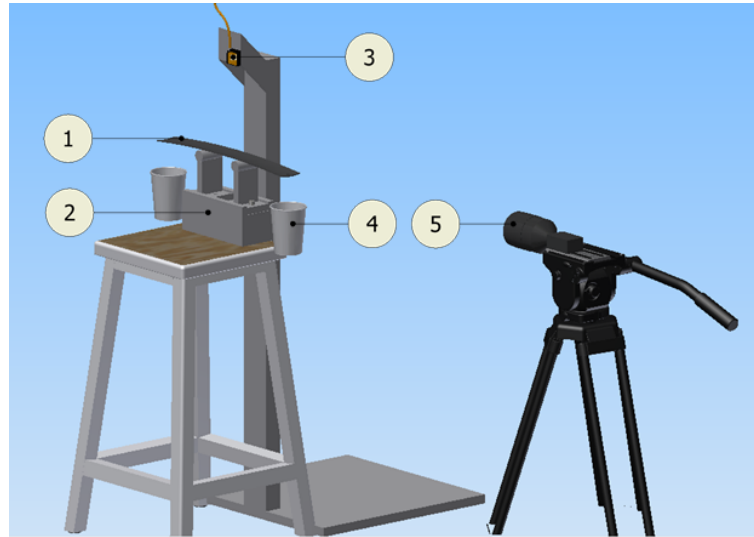


Figure 4.24: Experimental setup for four-point bending tests of elastomeric laminates. 1 - test sample, 2 - four-point bending rig, 3 - laser distance sensor for curvature measurement, 4 - mass bucket, 5 - HD camera for photographing the anticlastic curvature.

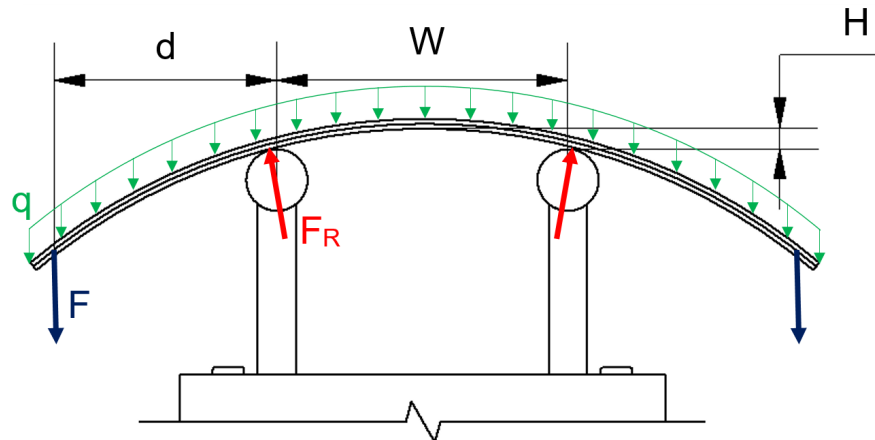


Figure 4.25: Schematic showing the loading on the test sample during experiments.  $F$  is the applied load,  $F_R$  the roller reaction, and  $q$  the distributed loading of the sample's weight.

can be assumed statically equivalent to a uniformly applied moment, as in this case.

## 4.4.2 Results and Discussion

For the purpose of this discussion, only the results from the narrow 30 mm and 40 mm laminates, as well as the wide 80 mm and 100 mm laminates, are presented here. This is to show the comparison of the analytical model accuracy for wide and narrow laminates. The anticlastic effects are first discussed, followed by the bending moment results.

### Anticlastic Curvature

The photographs of the anticlastic curvature are processed using the open source image processing software, ScanIt. The coordinates of the laminate's top surface are extracted and normalized with respect to the laminate thickness and width. The anticlastic deflection comparison between the theory and experiments for narrow laminates is shown in Figure-4.26. The theory demonstrates good correlation for narrow laminates, under-predicting the anticlastic edge deflections by less than 10% for larger curvatures (i.e. smaller radii of curvature).

The theoretical and experimental results for wide laminates are presented in Figure-4.27. It is seen that the theoretical model shows good correlation only for larger radii of curvature. As the radius decreases, the experimental results display an earlier transition to wide beam theory than predicted. The theoretical model suggests a more consistent curvature in the cross section, whereas the test sample shows a flattening close to the centre of the laminate, which is characteristic of wide beam theory as previously discussed in Chapter-2. The disagreement in the results is more pronounced for the 100 mm sample than for the 80 mm sample, but both show evidence of flattening at the centre of the laminate.

### Bending Moment

The bending moment predictions of the analytical model have been shown to correlate well with the finite element results. To validate these results the bending moment applied to the samples is plotted for increasing curvature, and compared with the analytical model.

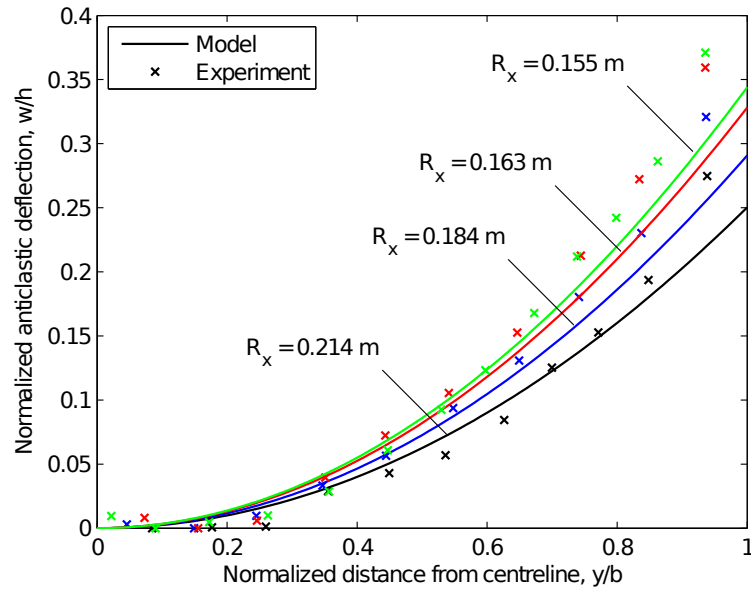
To ensure that the sample used in the experiment is not damaged in each test, and can therefore be used in subsequent tests, the bending stress is determined. The maximum bending stress encountered in the laminate is calculated using the equation

$$\sigma_x = \frac{Mz}{I_y}, \quad (4.23)$$

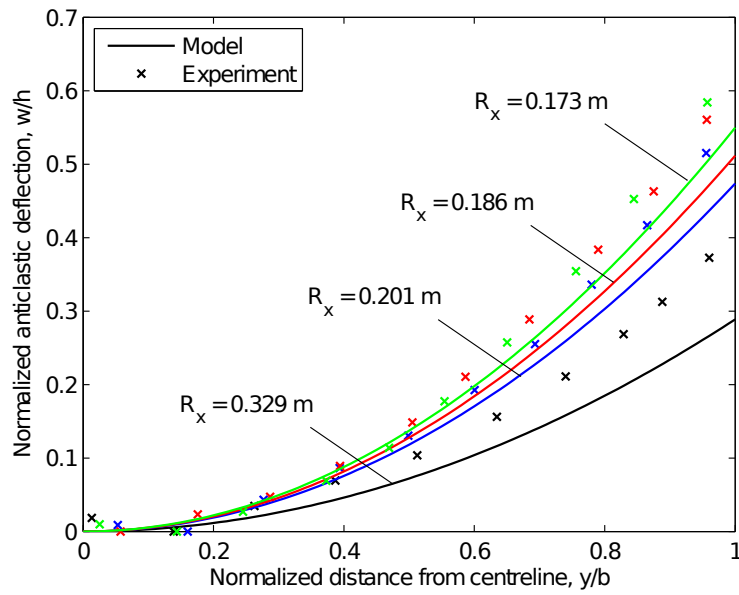
where  $z$  is the distance from the neutral axis to the furthest point in the cross section. Applying this expression to the most heavily loaded test for each sample width, the maximum bending stress is found to be 3.70 MPa, which is small enough to prevent any plastic deformation in the laminate during testing.

The results from the experiments are given in Figure-4.28 and Figure-4.29. For both narrow and wide laminates, the model significantly underestimates the bending stiffness of the samples. The reasons for this are discussed in the next section on CLT limitations. As a result, the analytical model is not suitable for predicting the bending stiffness of woven-fabric laminates.

The experiments confirm an increase in bending stiffness for increasing curvature. The experimental results are approximated to second-order polynomials to demonstrate this non-linearity. The results in

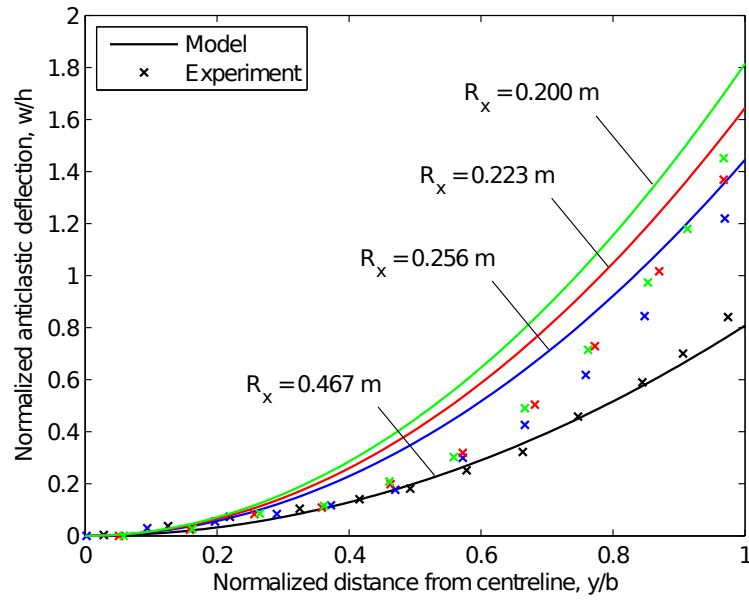


(a) Laminate width = 30 mm

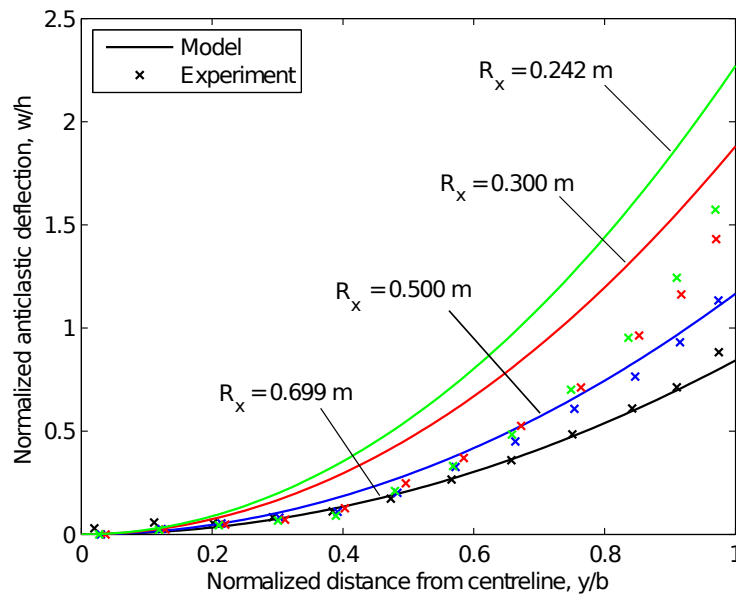


(b) Laminate width = 40 mm

Figure 4.26: Anticlastic curvature comparison between analytical model and experimental data for narrow laminates. The centreline is the longitudinal line running down the centre of the length of the laminate.



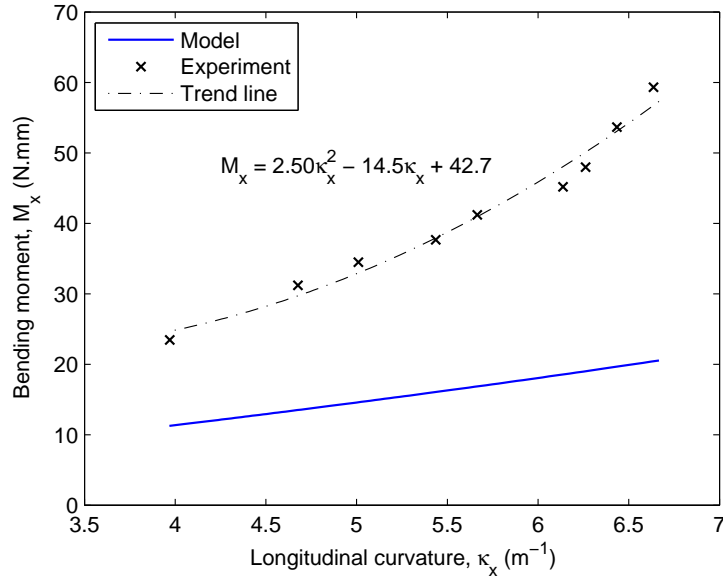
(a) Laminate width = 80 mm



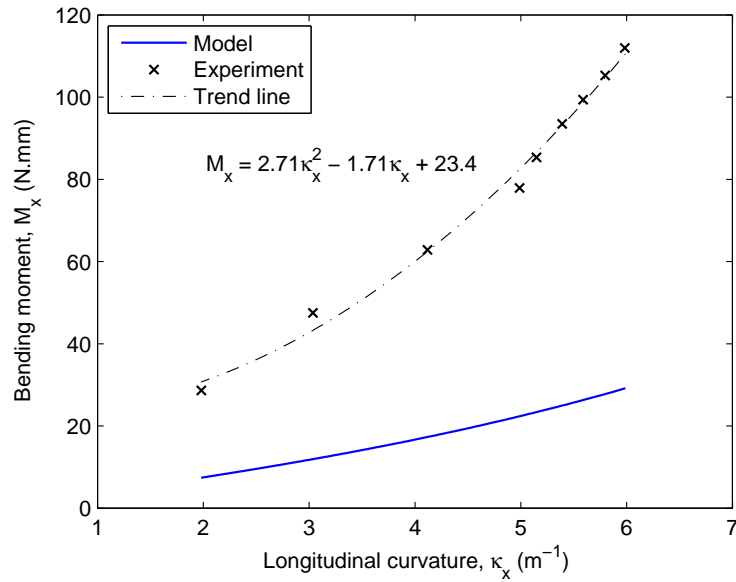
(b) Laminate width = 100 mm

Figure 4.27: Anticlastic curvature comparison between analytical model and experimental data for wider laminates. The centreline is the longitudinal line running down the centre of the length of the laminate.



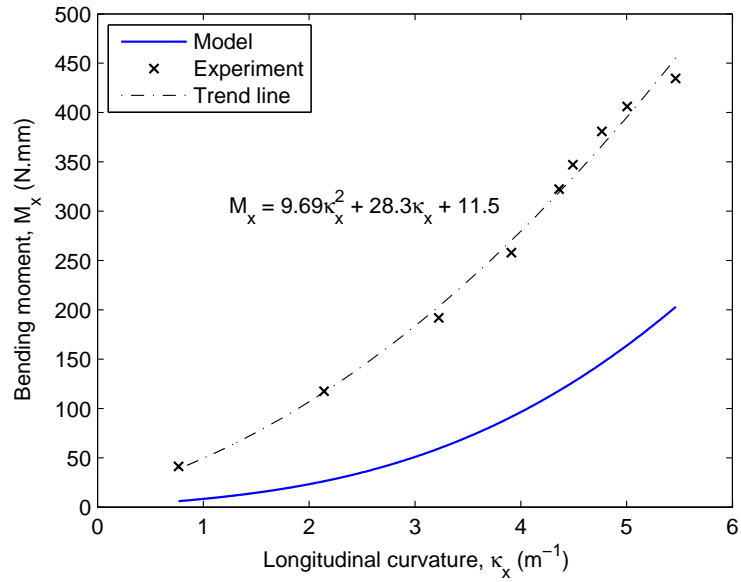


(a) Laminate width = 30 mm

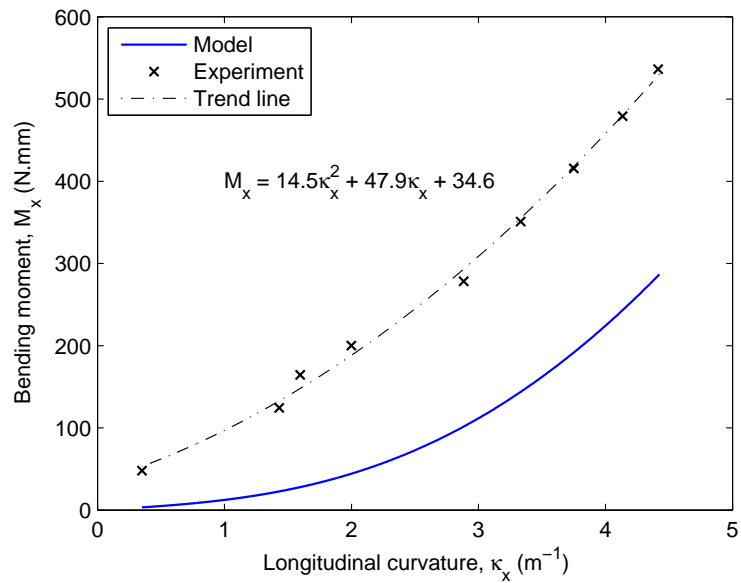


(b) Laminate width = 40 mm

Figure 4.28: Bending moment for increasing longitudinal curvature for narrow laminates with  $[(\pm 45F)_8]$  layout. The analytical model predictions are shown, displaying a large underestimation of the bending stiffness.



(a) Laminate width = 80 mm



(b) Laminate width = 100 mm

Figure 4.29: Bending moment for increasing longitudinal curvature for wide laminates with  $[(\pm 45F)_8]$  layup. The analytical model predictions here also underestimate the bending stiffness.

Figure-4.29 for wide laminates show a better correlation (in terms of curve gradient) compared to narrow laminates, which predict a near linear relationship for these relatively low curvatures.

In Section-4.3.2, a neutral axis discrepancy between the FE and analytical models is shown for wider laminates experiencing curvatures as small as  $2.5 \text{ m}^{-1}$  (see Figure-4.13(b)). If this shift is indicative of reality, then it is possible that the bending stiffness is higher than predicted, which is seen in the experimental results. However, there is insufficient evidence to suggest that this neutral axis shift occurs, since it is difficult to quantify in experiments.

The neutral axis does shift due to the difference in tensile and compressive moduli, but this would result in a lower bending stiffness as compared to a uniform elastic modulus. Thus, even if it were possible to measure the neutral axis location, it would be difficult to determine which phenomenon has the greatest impact on the neutral axis shift.

### Classical Lamination Theory Limitations

Despite CLT providing sufficiently accurate predictions for the behaviour of unidirectional laminates, it does not accurately model the laminae interactions for such laminates, let alone woven laminates. CLT models each lamina as a uniform distribution of fibres and resin and does not account for interlaminar shear effects, which are particularly influential in the bending behaviour of  $[\pm 45]$  laminates. This is particularly evident in Figure-4.12 in the shear discontinuities, although the analytical model correlates well with the unidirectional FE analysis, suggesting that CLT is a reasonable approximation.

However, a problem arises with the experimental results which show a large discrepancy with the predictions. The error can be attributed to the lack of accuracy for woven laminates. This can be best explained by considering the shear behaviour of the two  $[\pm 45]$  laminates under an applied bending moment. Assuming no interlaminar effects, the fibres in unidirectional laminae are free to rotate due to shear. Fibres in woven laminae, on the other hand, are constrained by the perpendicular interwoven fibres. The fibres in the  $+45$  direction can no longer rotate freely since they are being resisted by the  $-45$  fibres, and vice versa. As a result, the lamina will have greater stiffness than predicted.

Now reintroducing interlaminar effects, the stiffness is further increased due to the aforementioned rotation being additionally constrained. CLT accounts for neither of these, so it is expected for the laminate in reality to exhibit significantly higher stiffness, which is seen here in the experimental results.

In Section-4.1.2, it is shown that an epoxy laminate transitions to wide-beam anticlastic bending theory far earlier than for an elastomeric laminate. The epoxy laminate has a significantly larger elastic modulus, which supports the hypothesis that woven laminates have higher bending stiffness since the transition to wide-beam theory occurs in the experiments (see Figure-4.27) despite the theory suggesting otherwise.

### 4.4.3 Fibre Tow Buckling

It is found that for large curvatures of the elastomer region of the laminate, the fibre tows undergo buckling on the surface as shown in Figure-4.30. This poses a design challenge for dual-matrix laminates because it imposes limitations on the allowable curvature. Fibre tow buckling is more prevalent in  $[0/90]$  laminates when some of the fibres are aligned with the direction of applied stress.

Ahmadi *et al.* [1] model an individual fibre tow as a beam on elastic foundation where this foundation has the properties of the elastomer material. This enables the authors to predict the buckling load of the



Figure 4.30: Fibre-tow buckling of a  $[(0/90F)_8]$  elastomeric laminate.

laminate. This research is not further investigated by the author of this work, although it is worthwhile to consider the implications of this phenomenon on the design of dual-matrix laminates. Fibre-tow buckling is not as much of a concern for narrow  $[\pm 45]$  laminates which do not encounter it, even for relatively large curvatures. It becomes a problem with wider laminates when the anticlastic curvature is constrained and the strain energy in the laminate exceeds the minimum for which matrix failure occurs, resulting in buckling of the tows. Regardless, wider elastomeric laminates are not as suitable for providing the increased flexibility required in morphing applications, as compared to narrow laminates. Therefore, fibre tow buckling is not a concern here but it does require careful consideration when investigating larger deformations and/or wide laminate behaviour.

## 4.5 Large Deflection Modelling of a Beam

### 4.5.1 Introduction

Euler-Bernoulli beam theory is an extensively studied and well understood theory of the deflection of beams under various types of loads. This theory, however, is based on the assumption of small deflections and hence the deflection does not affect the internal moment in the beam. In reality, the translation and/or rotation of the applied load with the deflection of the beam results in a change in the internal moment. In beams with relatively high bending stiffness this change is negligible, but this is not true for compliant beams where large deflections are encountered. The literature reveals two techniques used to compute the large deflection of beams. Firstly, an integral approach utilizing an elliptic integral technique can be used to solve the complex integrals associated with this problem [8]. The second approach is to solve the problem numerically. While more time intensive, the numerical approach is easier to implement and provides highly accurate results. The work of Nallathambi *et al.* [31] has proved useful in deriving a model for a cantilevered beam with a follower load.

In a four-point bending test, the reactions at the supports are normal to the contact point between the beam and the support. In this case, the support reaction acts as a follower load, meaning that the reaction force remains normal to the surface of the beam. This must be accounted for in the internal bending moment expression for the beam. The following section describes the formulation of the internal bending moment expression for a straight cantilevered beam with a follower load. The derivation is based on the aforementioned work by Nallathambi *et al.*, with slight modification.

### 4.5.2 Derivation of the Large Deflection Governing Equation

Figure-4.31 shows a visual representation of a beam encountering large deflection under a follower load. The internal moment in the beam is given by

$$M(s) = P_y(L - u_L - x(s)) + P_x(v_L - y(s)), \quad (4.24)$$

where  $s$  is the arc length of the beam at a given point,  $L$  is the length of the beam, and  $u_L$  and  $v_L$  are the free-end displacements in the  $x$  and  $y$  directions respectively. The coordinates at any point along

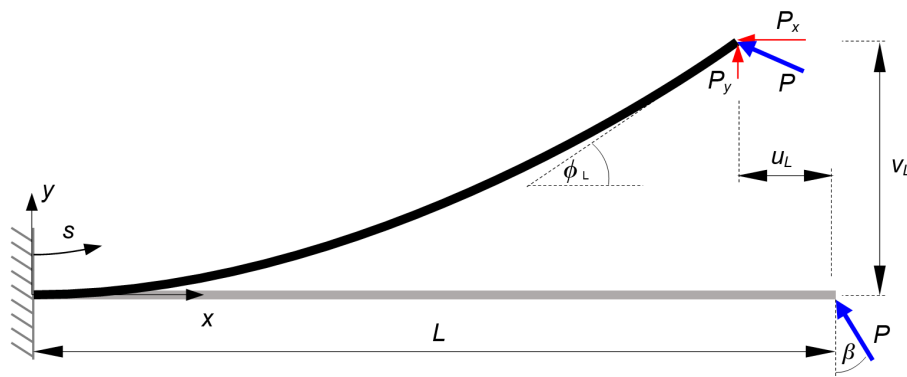


Figure 4.31: Straight cantilevered beam with an inclined follower load undergoing large deflection, where the assumptions in Euler-Bernoulli beam theory no longer apply.

the beam are determined by the expressions

$$\begin{aligned} x(s) &= \int_0^s \cos \phi(s) ds, \quad \text{and} \\ y(s) &= \int_0^s \sin \phi(s) ds, \end{aligned} \quad (4.25)$$

which are modified from [31]. Differentiating (4.24) yields

$$\frac{dM}{ds} = -P_y \frac{dx}{ds} - P_x \frac{dy}{ds} \quad (4.26)$$

$$= -P_y \cos \phi(s) - P_x \sin \phi(s). \quad (4.27)$$

The load components are related to the applied load by

$$P_x = P \sin(\phi_L + \beta) \quad (4.28)$$

$$P_y = P \cos(\phi_L + \beta)$$

where  $\beta$  is the inclined angle of the applied load, as defined previously. The well known definition of the curvature of a beam is given by

$$\kappa = \frac{M}{EI}, \quad (4.29)$$

which can be differentiated and substituted with (4.28), yielding

$$\frac{d\kappa}{ds} = \frac{d^2\phi}{ds^2} = \frac{1}{EI} \frac{dM}{ds} \quad (4.30)$$

$$= -\frac{P}{EI} \cos(\phi(s) - \phi_L - \beta), \quad (4.31)$$

where the cosine term is obtained from manipulation of (4.27) using trigonometric identities. This second-order differential equation is the governing equation for the deflection of the beam. This equation can be integrated numerically to determine the deflection and is detailed in the next section.

### 4.5.3 Determination of the Beam Deflection

The numerical integration of this second-order non-linear ordinary differential equation (ODE) is performed using the fourth-order Runge-Kutta (RK4) technique. This procedure can be found in Appendix-A.

The governing equation can be solved in one of two ways using the RK4 method. It can be integrated from the free end to the fixed end or vice versa. Integrating from the fixed end to the free end allows one to impose the zero-slope boundary condition directly but the fixed end curvature and free-end slope need to be assumed. Nallathambi *et al.* describe this as a two-point shooting technique. Integrating from the free end (one-point shooting technique) eliminates the need to assume a curvature since the curvature at the free end is known; it is zero unless an applied moment is introduced for which the induced curvature can be calculated directly. The boundary conditions for a cantilevered beam at the fixed-end are

$$\phi(0) = v(0) = 0. \quad (4.32)$$

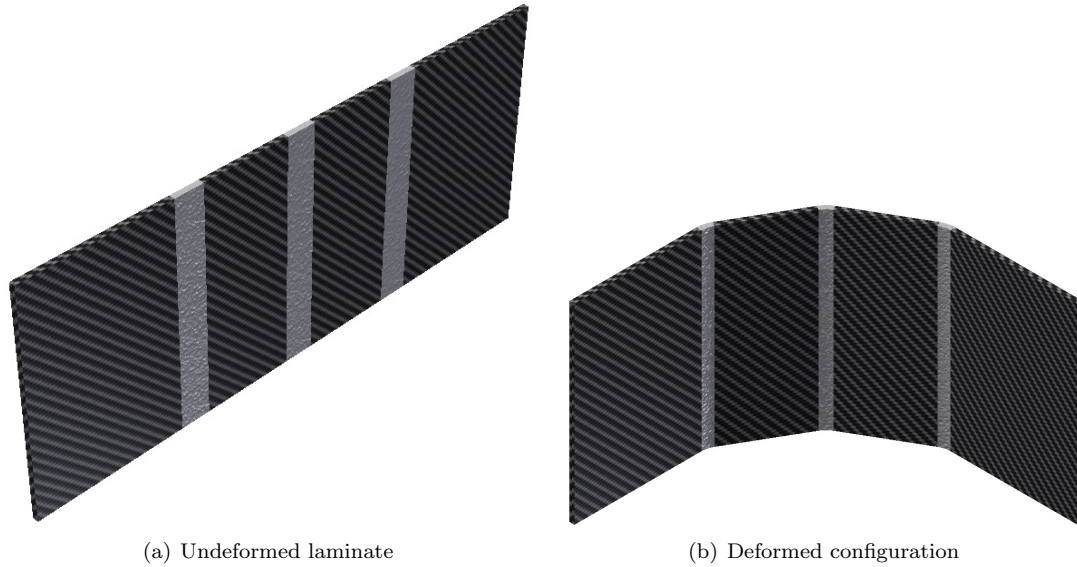


Figure 4.32: CAD representation of a dual-matrix laminate with three elastomeric matrix regions (light gray) with rigid epoxy resin elsewhere.

In order to determine the deflected shape of the beam, a free-end slope is initially assumed and the RK4 method is conducted. This method is solved iteratively until the fixed-end slope is zero. The free-end slope is incremented/decremented until a solution is obtained within a specified accuracy. The magnitude of the increment/decrement value is reduced when the fixed-end slope passes through zero and the direction of incrementation is reversed. This model is implemented in a MATLAB script.

#### 4.5.4 Large Deflection Modelling of a Beam with Flexible Regions

This model can be used to determine the deflection of a composite beam with distinct sections along its length of varying cross-section and/or material properties (see example in Figure-4.32). The motivation behind obtaining such a model is for the modelling of a dual-matrix fibre-composite laminate for application in morphing structures.

The above model is implemented by applying it to each distinct section of the beam and altering the boundary conditions at the free end accordingly. The following assumptions are made for the model:

1. Each section of the beam, considered in isolation, behaves as a cantilevered beam.
2. The slope and displacement at the interface between adjacent sections are continuous.

The analysis first begins at the free-end of the beam and as mentioned in assumption-1, the end that attaches to the next section is assumed to be “fixed”. This assumption is suitable since the load rotates with the end of the beam. After calculating the deflected shape of the section, the internal moment at the “fixed”-end can be determined. The same model is applied to the next section except that the moment at the “free”-end is no longer zero. The moment obtained at this location results in a non-zero curvature which is relayed to the model, and the same method is used to calculate the deformed shape. It is important to note that the applied force is still acting at the end of each section but, due to the rotation of the load, it is no longer perpendicular; the force is inclined at an angle,  $\beta$  (see Figure-4.31).

This process is repeated through all sections of the beam until the true fixed-end of the entire beam is reached. At this stage, the data for each section has been stored separately. Applying the condition that the slope and deflection at the joints between subsequent sections are continuous (as per assumption-2), the “free”-end slope and deflection of the first section are added to the values from the next section and so on.

#### 4.5.5 Model Verification

The large-deflection model is verified using Abaqus with 2D beam elements on a wire geometry with a specified beam cross-section. The cross-section dimensions and material properties are given in Table-4.5. The model exhibits highly accurate results, even for large free-end deflections as seen in Figure-4.33. The maximum load displayed for this model is 14 N due to the FE simulation encountering convergence issues for larger deflections, because the displacement corrections required to satisfy the force and moment equilibrium equations are larger than the displacement increment. Therefore, the simulation time increment required to achieve equilibrium becomes impractically small. Nonetheless, the results are sufficient to show the high accuracy of the model, with respect to the FEM. The 2D FEM does not account for Poisson ratios so the anticlastic effects are not modelled. This is not indicative of reality, thus the anticlastic model needs to be incorporated into the large-deflection beam model.

#### 4.5.6 Incorporating the Anticlastic Bending Model

Thus far, the large deflection model has assumed different but constant bending stiffness for each section. Knowing that this is not the case for sections exhibiting large anticlastic curvatures, it is imperative to incorporate the anticlastic bending model. Assuming that the curvature of the rigid section is small, which is a valid assumption for the dual-matrix laminate, this model only needs to be incorporated in the flexible region.

Due to the dual-matrix interaction (see Section-4.3.5) not being fully characterized, the bending behaviour of the dual-matrix laminate is modelled as distinct sections with no interaction, as a first approximation. Assuming that the flexible region length is longer than two and half times its width (which can also be achieved by creating slits), this is a reasonable approximation.

Provided that the length of the flexible hinge is relatively small compared to the rigid section, the curvature in the flexible region is constant. The initial calculated curvature at the “free”-end is obtained as before but now it is passed through a loop which calculates the new  $I$  value for that curvature. The initial curvature is an over-estimation so the new value for the curvature is less than the initial. This loop is repeated until the curvature is within a specified accuracy, and then the curvature is forwarded to the RK4 function. If the flexible region is long enough such that the curvature is not constant, this loop can be placed inside the RK4 function. In this case, a new curvature has to be calculated at every increment along the length of the beam, so the computation time increases substantially. The large-deflection model can be tailored to suit a specific application, where the user can trade-off the desired accuracy and computational cost.



Table 4.5: Beam cross section and material properties for Abaqus verification of large-deflection beam model.

Parameter	Value
Width (mm)	40
Thickness (mm)	2
Second Moment of Area (mm <sup>4</sup> )	26.67
$E_{rigid}$ (GPa)	35
$E_{flexible}$ (GPa)	0.5

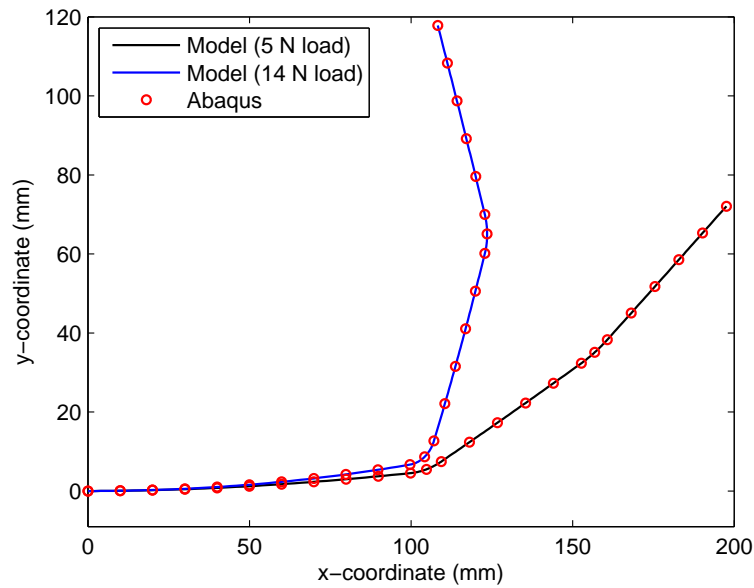


Figure 4.33: Large-deflection beam model verification using Abaqus FEA for 5 N and 14 N follower tip loads, showing close correlation of the results.

# Chapter 5

## Applications

### 5.1 Composite Meal-Tray Table

The meal-tray table in a commercial aircraft is a very simple design, which has served its purpose well for many years. However, this part is often relatively heavy, and since there are a large number of them on board an aircraft, the cumulative weight of the tray tables is substantial. This presents an opportunity to save weight on the interior design of the aircraft, by designing a tray table which is light and strong. In addition, this application is an ideal opportunity to demonstrate the morphing capability of a dual-matrix laminate, before the technology progresses to critical aircraft components.

Upon presentation of the dual-matrix technology to Bombardier Aerospace, the interior design team requested a lightweight morphing tray table. Figure-5.1 is a conceptual design, provided by Bombardier Aerospace, of the envisaged tray table. Ideally, the tray table would deploy upon some passenger input and then remain in the horizontal position without a mechanical stop for a variety of objects on the table, ranging from a lightweight meal-tray to a heavy laptop, but this is difficult to achieve.

The dual-matrix stiffness tailoring of the composite laminate is useful for achieving a reduced stiffness in the effective “hinge”. Further tailoring of the stiffness, such that the stiffness of that section increases as the curvature increases, is not particularly easy. Section-4.3 describes the phenomenon whereby the bending stiffness increases as the curvature increases but this increase is insufficient to be of use in this particular application.

#### 5.1.1 Design and Analysis

##### Requirements

As requested by Bombardier Aerospace, the tray table must:

- support a load of 5 kg (heaviest laptop on the market).
- remain horizontal even with a reclined seat-back.
- accommodate beverages (this requirement is not addressed for the prototype, but it can be introduced later on with ease).
- be heat resistant to hot meals placed on the table.

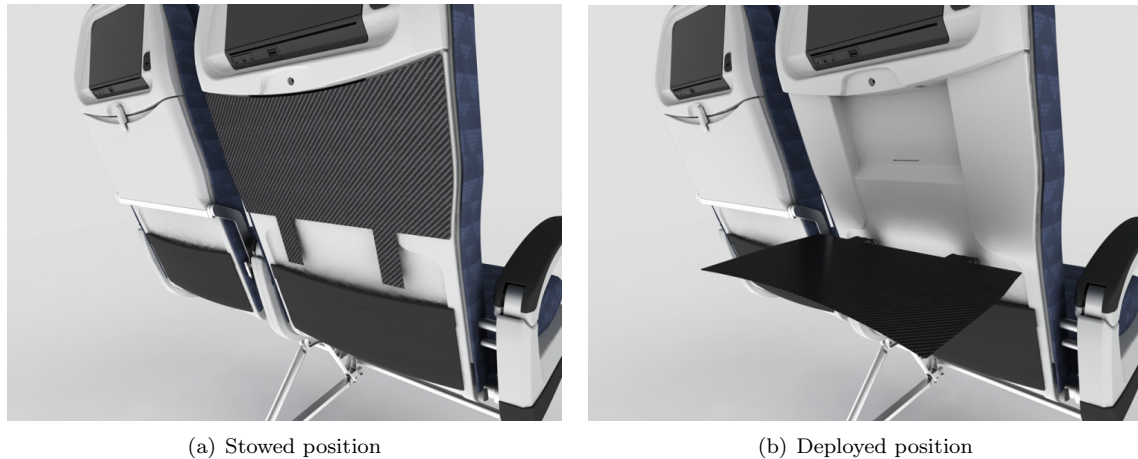


Figure 5.1: Bombardier conceptual drawing of morphing composite tray table. The current tray table design in service is shown on the left seat.

- be lightweight.

The first two requirements are related in that the table must support a heavy load, but it must also remain horizontal, even when there is no load on the table, yielding the need for a mechanical stop. This functionality would ideally be included in the dual-matrix hinge itself, but the technology is not advanced enough to achieve this. As a result, the tray table prototype is designed to remain horizontal under its own weight, and any additional load placed on the tray table is supported by the mechanical stop.

### Hinge Design

The designer has the flexibility to include one or multiple hinges in the design in order to achieve the required deflection. This is dependent on the aircraft requirements, for example the Bombardier Q400 aircraft has arm rests (to which the tray table would attach) that are near vertical, meaning that the hinge has to allow for almost  $90^\circ$  deflection. One hinge is not ideal because it requires a relatively long tray table to extend to the passenger.

In order to achieve a smooth transition from the near-vertical armrest mounting point, a double hinge design is required, that is, two regions of flexible matrix material in each hinge. These regions can be tailored separately to achieve different curvatures for a given load. The large deflection model derived in Section-4.5 is used to determine the necessary parameters of the hinges to achieve the required deflection for the tray table. The lower hinge transmits a greater bending moment than does the upper hinge, so the lower hinge requires a larger bending stiffness and/or shorter length so that the curvature in the hinge does not cause tray table to droop too low. Thus, one slit in the lower hinge and three slits in the upper hinge (i.e. split into two and four sections respectively) are used in the large deflection model. This model assumes that the elastic moduli of the adjacent regions are independent, which has shown not to be the case for dual-matrix laminates. However, the model is suitable for a first approximation; the predicted deflections are larger than the actual deflections, thus providing a conservative solution. Figure-5.2 shows the deflection of the tray table prototype for an end-load of 1 N. This is the equivalent load per hinge for the tray table's own weight, calculated as 410 g (using a density of  $1.3 \text{ g/cm}^3$ ). To

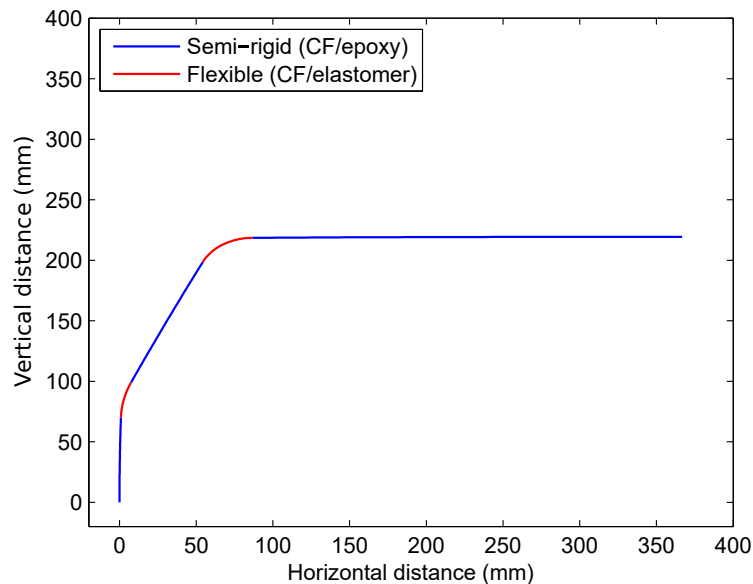


Figure 5.2: Tray table prototype predicted deflection under its own weight ( $\pm 410$  g), which is an equivalent end load of approximately 1 N.

Table 5.1: Section and material properties for large deflection modelling of the tray table prototype.

Section	CF/epoxy (Table)	CF/epoxy (Hinge)	CF/elastomer (Hinge)
Layup	[[0/90F] <sub>10</sub> ]	[[ $\pm 45$ F] <sub>8</sub> ]	[[ $\pm 45$ F] <sub>8</sub> ]
Width (mm)	238 <sup>1</sup>	50	50
Thickness (mm)	2	2.1	2.1
$E_{eff}$ (GPa)	45.3	11.9	0.117
Second Moment of Area (mm <sup>4</sup> )	159	38.6	Variable

achieve this deflection for the 1 N load, the lower hinge length is specified as 12 mm and the upper hinge 20 mm. The section properties for the different regions used in the large deflection model are given in Table-5.1.

Again, this model is idealized and there are necessary assumptions made to simplify the model. The results from this analysis provide a starting point for the fabrication of the actual tray table prototype. The lengths of the two hinges are increased to account for the dual-matrix interaction. The prototype is fabricated with hinge lengths of 30 mm and 35 mm for the lower and upper hinges respectively.

### Mechanical Stop

Three concepts have been generated to address this design requirement. Two of the concepts are moving mechanical mechanisms (see Figure-5.3(a) and Figure-5.3(b)). One has a fixed-length rod that runs in a slider on the tray table; the rod makes contact with the end of the slider when the tray table is horizontal. The other concept is a piston mechanism, for which the length of the piston can be designed to make contact with the end of the cylinder, thereby securing the tray table in the horizontal position. Even though it is desirable to have a system which eliminates the need for moving mechanical components,

<sup>1</sup>Half the actual width of the table since each double hinge supports half the load

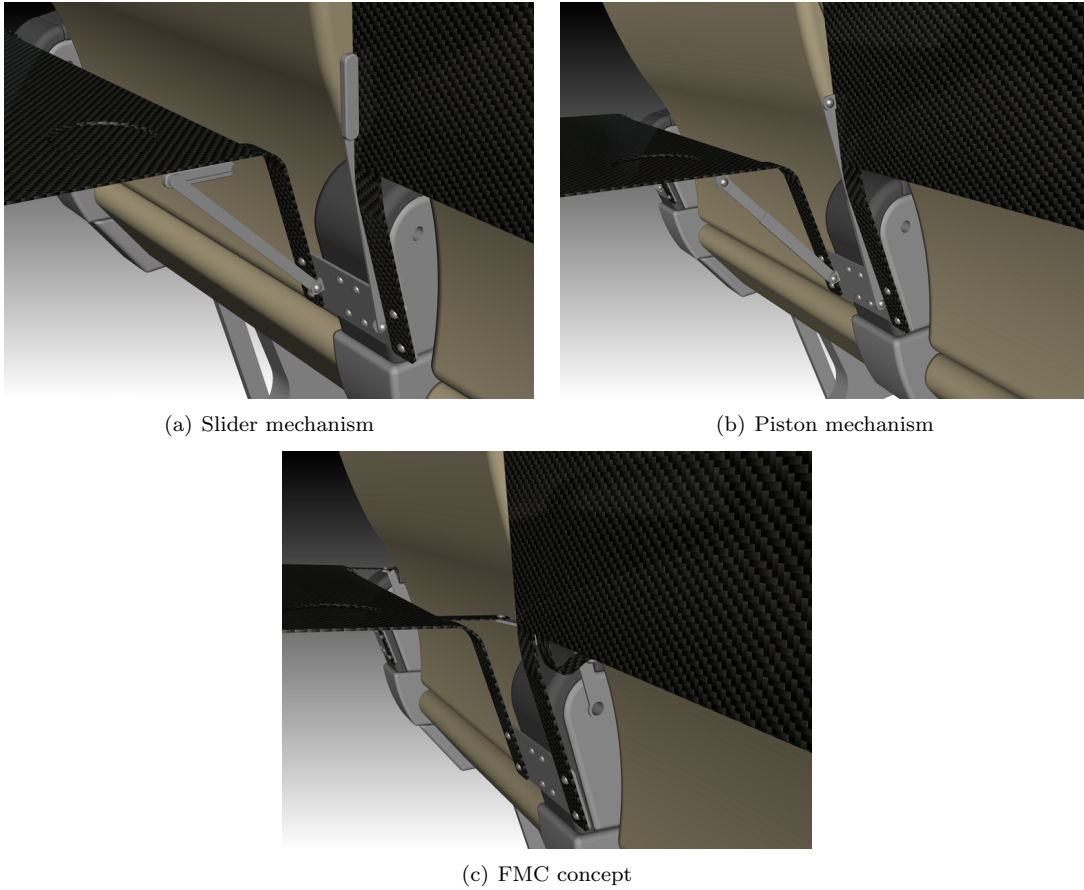


Figure 5.3: Various mechanical stop concepts to prevent deflection of the tray table beyond the horizontal. The dual-matrix hinges do not provide sufficient stiffness to stop the tray table from deflecting further when a load is applied to the table.

these concepts can support large tray table loads. Figure-5.3(c) shows a concept which utilizes a flexible matrix composite (FMC) laminate as the locking mechanism. The laminate folds in the stowed position (without damage due to high strain capability) and is elongated in the deployed position, as shown. Since composites are particularly strong in tension, the laminate can be thin to achieve high curvatures while still being able to provide effective resistance to tensile loads.

The slider mechanism concept is chosen for the prototype due to its relative simplicity and ease of manufacturing. The slider component is mounted at the bottom of the hinge (see Figure-5.8(a)) to make the mechanism as low-profile as possible.

The critical buckling load of the pinned-pinned hollow tube is given by the Euler buckling equation

$$P_{cr} = \frac{\pi^2 EI}{L^2}, \quad (5.1)$$

where the second moment of area is given by

$$I = \frac{\pi}{4}(r_o^4 - r_i^4), \quad (5.2)$$

where  $r_o$  and  $r_i$  are the outer and inner radii respectively. The material is 6061 aluminum with a modulus

of elasticity of 68.9 GPa [27]. The rod is sized assuming a worst-case 5 kg load,  $P$ . Figure-5.4 shows the free body diagram of the system, where the edge of the first hinge is assumed to be a pinned boundary condition. The maximum expected force in the rod is 430 N. Using this as an initial estimate for the critical buckling load, the most suitable tubing is 1/4" outer diameter and 0.18" inner diameter (6.350 mm and 4.572 mm respectively). The length of the rod is 280 mm, yielding a buckling load of 506 N. The safety factor is 1.2, which is low for a component that is subjected to human loading. Therefore, a larger diameter rod should be retrofitted to ensure that the rod does not buckle. However, the mechanical stop is designed to fail first so as to protect the expensive, and difficult to replace, composite tray table.

### 5.1.2 Prototype Fabrication

The manufacturing of the prototype is done in two parts. First, the double hinge system is fabricated using the technique outlined in Section-3.2. Two hinges are made, one for either side as shown in Figure-5.5.

There is an additional section of uncured woven fabric to allow for overlapping when the table section is manufactured (this is the second part of the fabrication process which is shown in Figure-5.6).

There are two reasons for the two-part fabrication process, namely, ease of manufacture and stiffness tailoring. Separate fabrication of the two hinges and table allows for easier integration of the three individual components since alignment is done in the final stage. More importantly, the table can have a different layup orientation compared to the hinges, thus achieving variable stiffness between the regions. The hinge section is a  $[(\pm 45F)_8]$  layup to minimize the bending stiffness, while the table itself requires a much larger bending stiffness (i.e.  $[(0/90F)_{10}]$ ). This could also be achieved by variable angle tows (see Section-2.2.5), however this fabrication technique requires outsourcing so a discontinuous orientation layup between the sections is preferred, although there is an overlap as shown in Figure-5.6 to ensure effective load transfer. The overlap layup is demonstrated in Figure-5.7. This layup maximizes the contact area, while minimizing the thickness of the overlap due to the cutouts as shown in Figure-5.6(b). The layup depicted here is the reverse order of the tray table, i.e. the bottom layer shown here is the top of the tray table. The laminate is fabricated this way to ensure that the top of the tray table is flat. In addition, a better surface finish is achieved by using release agent instead of a peel ply (see Section-3.2).

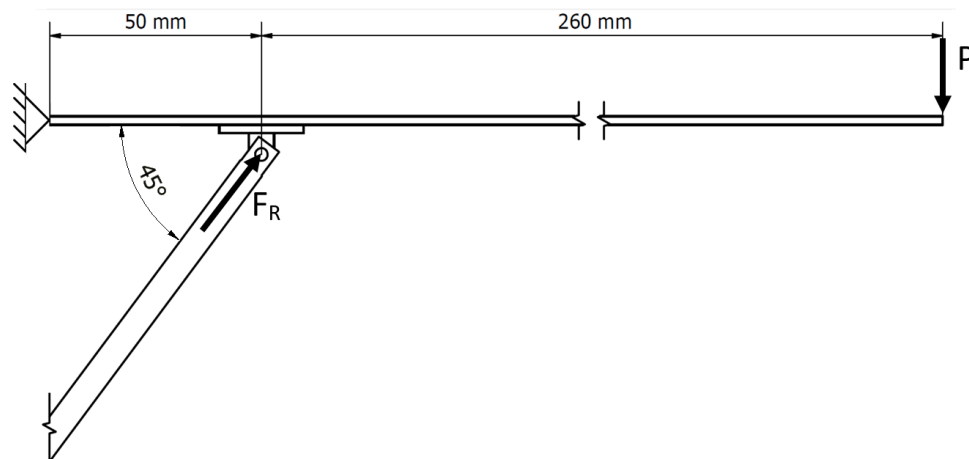


Figure 5.4: Free body diagram for sliding mechanical stop

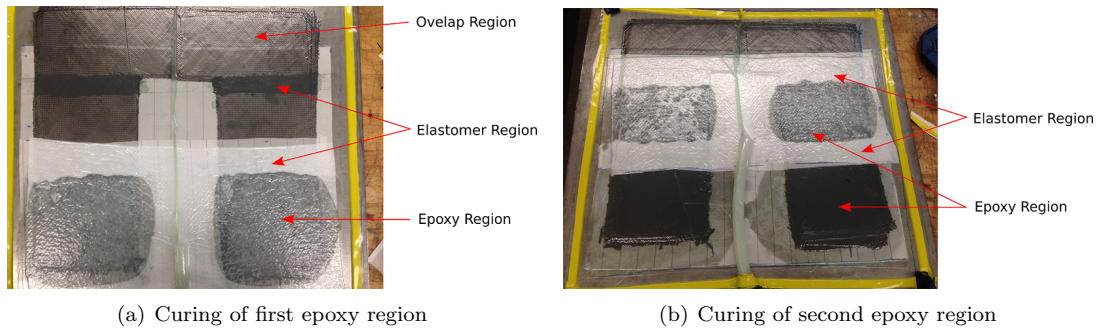


Figure 5.5: Vacuum bag curing of epoxy regions of the double hinge. The elastomer regions are previously cured using the same procedure.

Two issues are encountered during fabrication of the hinges. First, it is found that the elastomer resin in the bottom ply extends outside the intended boundary, whereas for the top ply it remains within the boundaries. Similarly, the epoxy resin also spreads over a part of the elastomer region, which is undesirable since the epoxy layer stiffens the flexible region. Techniques for preventing this are being investigated, such as breather ply isolation. In this technique, the breather ply is isolated to the exact enclosed region being cured, so that the rest of the laminate outside the boundaries is not penetrated, due to the vacuum seal.

The final prototype assembly is shown in Figure-5.8. The tray table is mounted to a rigid wooden frame to simulate a seat attachment. The hinges are twice as wide as they are long, so it is expected that the effective stiffness of the hinges will be similar to that of the epoxy region, as seen in Section-4.1.3. Therefore, it is predetermined that the hinges require slits to tailor their bending stiffness. As discussed in Section-4.3.5, the anticlastic effect is unconstrained only when the width is at most one half of the length. It is advantageous to begin with a hinge that is too wide so that the bending stiffness can be tailored progressively by cutting more slits. In this specific application, the bending stiffness of each hinge is tailored separately. This is necessary because the lower hinge transmits a larger bending moment than the upper hinge. In addition, the upper hinge is designed for a larger curvature to achieve the most ergonomic height of the tray table. Figure-5.9 shows the double hinge where three slits have been cut in the upper hinge and one is cut into the lower hinge. The difference in hinge curvature is clearly seen here.

### 5.1.3 Prototype Testing

The morphing tray table operation is demonstrated successfully. When the latch is released, the table deploys as expected under its own weight and comes to rest in the horizontal position. A 1 kg weight is placed on the tray and it is comfortably supported as seen in Figure-5.8(b). The limitation with this design is an unconstrained degree of freedom, due to the double hinge. Under an applied load, the table extends outward and drops down slightly, but the table remains horizontal during this translation.

The structural components themselves are designed to withstand a much higher load than 1 kg, but the lack of rigidity in the structure precludes testing of the table at higher loads. The most practical solution to this problem is one hinge instead of two, but this is potentially limiting since the double hinge allows the tray table to extend further outward toward the passenger, making it more ergonomic. This also prevents the fully-reclined seat in front from making contact with the table.



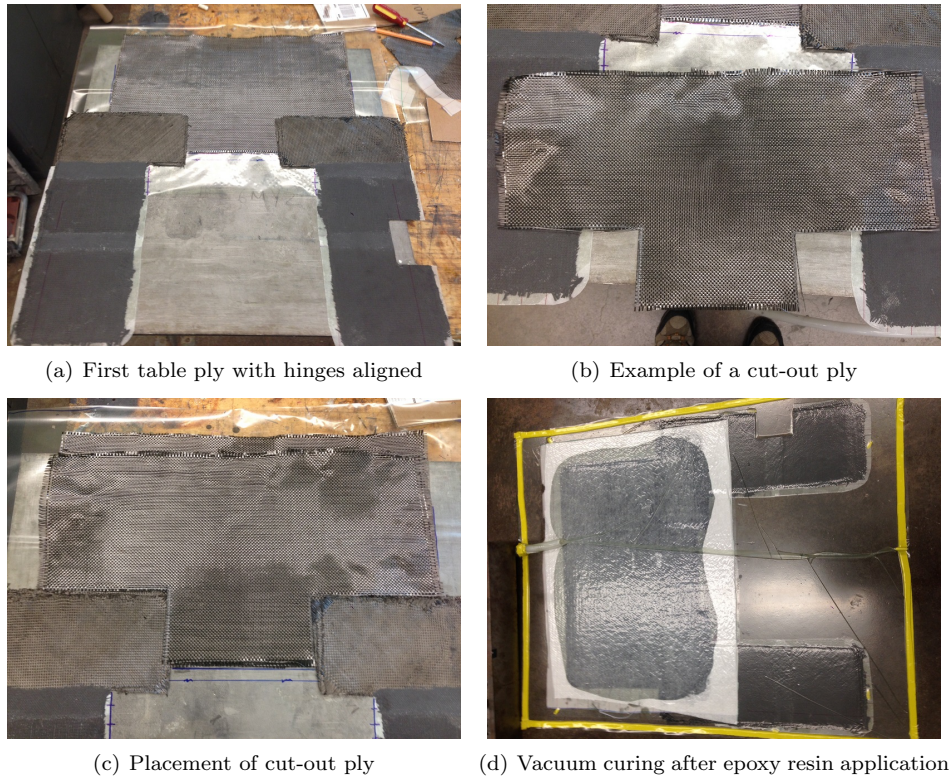


Figure 5.6: Final tray table fabrication process, incorporating the hinges into the overall structure. The laminate is initially over-sized so that the final cutting can be done more accurately.

## 5.2 Alternate Applications

Other applications of this technology have not been investigated extensively, but this section suggests potential applications that may benefit from stiffness tailored dual-matrix composite structures. The ultimate objective here is to provide materials that are beneficial for morphing of critical aircraft components such as flaps and control surfaces. However, this technology is still maturing and requires significant research before being implemented in such applications.

Another application, which is perhaps more relevant for the small increase in bending stiffness due to anticlastic bending, is structural applications in space where high precision may be required, while the loads are relatively small. The accurate modelling of a dual-matrix composite would be useful in high precision applications, such as flexible robotic manipulators, to ensure that the end-point of a beam (perhaps a manipulator) is tracked accurately.

The design flexibility provided by the numerous variables (thickness, orientation, material, geometry, etc.) allows for a wide range of applicability for this technology.



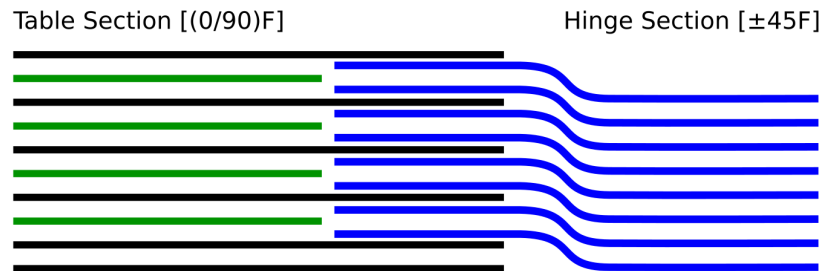


Figure 5.7: Layup of the overlap section. The black lines represent the rectangular table plies, the green lines represent the cut-out table plies and the blue lines represent the hinge plies



(a) Stowed position



(b) Deployed position

Figure 5.8: Tray table final prototype assembly with 1 kg weight as a demonstration.

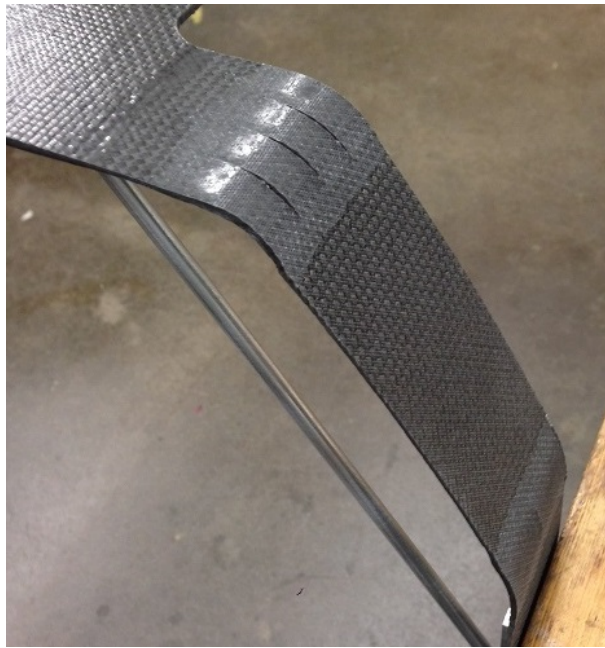


Figure 5.9: Prototype double hinge showing three slits in upper hinge and 1 slit in lower hinge for stiffness tailoring

# Chapter 6

## Conclusions

This thesis investigates tailoring the bending stiffness of dual-matrix composites. The dual-matrix laminate investigated here is comprised of an elastomeric region and an epoxy region. The local bending stiffness of the elastomeric region is significantly lower than that of the epoxy region. This has allowed for stiffness tailoring, using predetermined isolated sections of each matrix material, to achieve varied bending stiffness in the laminate. This technology is utilized in a morphing composite tray table for Bombardier Aerospace aircraft. A prototype was manufactured and demonstrated to behave as intended.

The relative novelty of this technology required the characterization of the composite material properties. First, the material properties of different layups of epoxy and elastomer resin laminates were determined experimentally. It was found that the carbon-fibre/epoxy laminate had a uniaxial tensile stiffness of three orders of magnitude larger than that of the carbon-fibre/elastomer laminate, for a  $[\pm 45_n]$  layup. The elastic modulus values obtained from the experimental testing were larger than those predicted by classical lamination theory (CLT), due to CLT assuming unidirectional laminae and neglecting interlamina effects, while the actual laminate was fabricated from woven-fabric carbon fibre. Obtaining the compressive properties of the flat elastomeric laminates was unsuccessful with the available experimental setup, due to buckling of the samples.

A novel technique was developed for the fabrication of dual-matrix laminates using polyurethane elastomer resin and epoxy resin as the matrix materials. The technique took advantage of the quick gel time of the elastomer resin, by first curing the elastomeric region(s). The elastomer remained reasonably isolated to the location of application, even during vacuum curing. The cured elastomeric resin acted as a dam during curing of the epoxy regions, helping to prevent overlap of the resins. Manufacturing difficulties were encountered for thicker elastomeric laminates ( $\geq 8$  plies), as well as for woven fabric patterns other than plain weave. It was found that the resin began to gel before the last few plies were added, and the resin did not penetrate the fabric, resulting in voids in the laminate. This problem was remedied by ensuring that the hand lay up process was performed quickly and/or by placing the resin in a freezer before mixing to increase the gel time. It was also found that the epoxy resin slightly overlapped the elastomeric region in the dual-matrix laminates. Techniques for preventing this are suggested for future work.

In this work, it has been shown that the relative stiffnesses are not only a function of the matrix material properties, but also a function of the laminate geometry. A 100 mm wide dual-matrix laminate was fabricated to assess the quality of the manufacturing process, and coincidentally it was found that

a narrow 10 mm wide strip of the laminate demonstrated a reduced stiffness (per unit width) in the elastomeric region, compared to a 20 mm wide strip of the same original laminate. This provided evidence of interaction effects between the two regions. This was briefly investigated in a preliminary experiment, where slits were cut in the elastomeric region of the dual-matrix laminate, thereby making the laminate narrower (same overall width as before the slits were made). It was determined, through FEA, that the length of the elastomeric region was required to be a minimum of two and a half times its width for these effects to have negligible impact on the behaviour of the laminate.

Using the anticlastic deflection model derived by Hyer and Bhavani [20], the anticlastic bending of composites has been modelled and verified with Abaqus FEA. The model accurately predicted the deflection of the cross-section for an applied longitudinal curvature, having higher accuracy for flexible matrix composites than for epoxy resin composites. The change in cross-section shape resulted in an increased second moment of area, and as a result, increased the bending stiffness of the laminate. This increase was investigated, and the results showed that the increase was greatest for laminates with large width and small thickness. It was also seen that, for large curvatures of wider laminates, the bending stiffness began to plateau, due to the cross section deflection transitioning to wide-beam anticlastic behaviour.

The derived analytical model correlated closely with Abaqus, but the experimental results displayed a large discrepancy, with the analytical model under-predicting the bending stiffness. However, the analytical predictions for the anticlastic deflection of the cross-section correlated well with the experimental results. Wider laminates under large curvatures showed the greatest discrepancy. The reason for these discrepancies was narrowed down to the composite layup. The analytical model and FE model specify a layup of unidirectional plies, whereas woven fabric was used in the experiments. The woven-fabric composites have increased shear stiffness, due to the woven laminae shear properties differing from that of unidirectional laminae. The FEA revealed that the bending stress and strain were highly dominated by shear for a  $[\pm 45_n]$  layup. Therefore, differences in the shear behaviour had a significant impact on the bending stiffness of the laminate.

A model for beams undergoing large deflections was derived, using fourth-order Runge-Kutta numerical integration, to predict the deflection of a beam comprised of adjacent flexible and semi-rigid regions. The predicted deflections were verified with Abaqus, exhibiting highly accurate deflection results. The anticlastic bending model was incorporated into the large deflection model, but dual-matrix interactions at the interfaces were ignored, as a first approximation.

The aircraft applications of this work are numerous, from non-critical cabin components (e.g. flexible composite hinges) to higher risk components such as control surfaces. This work was applied to cabin interiors, specifically a morphing composite meal-tray table. The dual-matrix fabrication process developed in this work was used to construct a tray table prototype, and the prototype was demonstrated to deflect as expected. The structure was designed to support a load of 10 kg on the centre of the tray table, using a mechanical stop to maintain a horizontal surface. A double-hinge design (two elastomeric regions in series, separated by an epoxy region) was used, which resulted in an extra degree of freedom in the system, thereby limiting the testing to a 1 kg load, even though the components themselves were designed to sustain the full 10 kg load.

## 6.1 Recommendations

Modelling the bending stiffness of elastomeric laminates with improved accuracy requires the material properties to be completely characterized, both in tension and compression. As seen in this work, compressive testing of elastomeric laminates is challenging, due to buckling resulting from low bending stiffness. The compressive properties can be obtained by fabricating elastomeric carbon-fibre tubes, instead of laminates. The circular cross section significantly increases the bending stiffness (by a factor of more than 60 for the same cross sectional area and thickness), therefore the buckling load will be substantially larger, allowing the compressive modulus to be obtained.

The suppression of the anticlastic curvature due to the interaction between adjacent epoxy and elastomeric regions has been investigated briefly, but further detailed analysis and characterization is required to improve the accuracy of the derived large deflection model. This can be achieved by modelling the transitional behaviour of the elastomeric matrix in the region close to the matrix interface. This would only be necessary in cases where the length of the region is less than three widths of the cross-section.

Since the strains and stresses encountered in the elastomeric laminates were relatively small, the reduction in stiffness of the  $[\pm 45_n]$  elastomeric region, due to bilinearity (see Figure-3.9(b)), was not taken into account. In applications where higher stresses and strains are expected, this reduction in stiffness would significantly affect behaviour of the laminate, and thus should be considered.

The main limitation of this work is the specification of material properties in the analytical model and Abaqus, which do not accurately represent woven-fabric composites. Therefore, it is recommended to investigate alternative methods of accurately representing the laminates. Three potential methods in Abaqus are: the addition of a rebar layer within the unidirectional lamina, specifying the material properties in different directions in the *Engineering Constants* material option, or providing the orthotropic parameters (the Abaqus manual provides the formulae for determining these parameters).

The ideal morphing composite tray table would be unaided by an external mechanical stop, and the composite structure itself be all encompassing, providing the deformation and locking features. Achieving this is challenging without some kind of locking mechanism (this could be made of composites too), as it requires an almost instantaneous increase in bending stiffness at the tray table's horizontal position. For the purpose of the prototype, the mechanical stop is sufficient for proof-of-concept, but it is recommended for future design iterations to design an alternative low-profile locking mechanism.

# Bibliography

- [1] H. Ahmadi, C. A. Steeves, and C. Daraio. Mechanical characterization of elastic laminates for dual-matrix composites. Master's thesis, Swiss Federal Institute of Technology (ETH Zurich), 2016.
- [2] Airbus. *Qatar Airways A350 XWB – factsheet*, December 2014.
- [3] K. L. Alderson, V. R. Simkins, V. L. Coenen, P. J. Davies, A. Alderson, and K. E. Evans. How to make auxetic fibre reinforced composites. *Physica Status Solidi (B) Basic Research*, 242(3):509–518, 2005.
- [4] D. G. Ashwell. The anticlastic curvature of rectangular beams and plates. *J. Royal Aeronaut. Soc.*, 54, 1950.
- [5] S. Barbarino, O. Bilgen, R. M. Ajaj, M. I. Friswell, and D. J. Inman. A review of morphing aircraft. *Journal of Intelligent Material Systems and Structures*, 22(June):823–877, 2011.
- [6] Boeing. *787 Aircraft Rescue and Firefighting – Composite Structure*, April 2013.
- [7] C. R. Bowen, H. A. Kim, and A. I. T. Salo. Active composites based on bistable laminates. In *ICMAT Symposia Proceedings*, volume 75, pages 140–144, Singapore, 2014. Elsevier B.V.
- [8] L. Chen. An integral approach for large deflection cantilever beams. *International Journal of Non-Linear Mechanics*, 45(3):301–305, 2010.
- [9] F. Dai, B. Zhang, and S. Du. A novel bistable hybrid composite laminate. *International Conferences on Composite Materials {ICCM}*, 2009.
- [10] S. Daynes, S. J. Nall, K. D. Potter, P. Margaritis, P. H. Mellor, and P. M. Weaver. Bistable composite flap for an airfoil. *Journal of Aircraft*, 47(1):334–338, 2010.
- [11] S. Daynes and P. M. Weaver. Stiffness tailoring using prestress in adaptive composite structures. *Composite Structures*, 106:282–287, 2013.
- [12] S. Daynes, P. M. Weaver, and J. A. Trevarthen. A morphing composite air inlet with multiple stable shapes. *Journal of Intelligent Material Systems and Structures*, 22:961–973, 2011.
- [13] S. L. dos Santos e Lucato, J. Wang, P. Maxwell, R. M. McMeeking, and A. G. Evans. Design and demonstration of a high authority shape morphing structure. *International Journal of Solids and Structures*, 41:3521–3543, 2004.
- [14] E. Eckstein, A. Pirrera, and P. M. Weaver. Multi-mode morphing using initially curved composite plates. *Composite Structures*, 109:240–245, 2014.

- [15] R. T. Fenner and J. N. Reddy. *Mechanics of Solids and Structures*, pages 642–645. CRC Press, 2nd edition, 2012.
- [16] FlexSys. At last, a shape-morphing aircraft wing is here - no flaps. Web Page, 2015. Available from: <http://www.flxsys.com/gallery>.
- [17] Air Transport Action Group. Facts and figures. Web Page, 2016. Available from: <http://www.atag.org/facts-and-figures.html>.
- [18] R. C. Hibbeler. *Mechanics of Materials*, chapter 6. Pearson Prentice Hall, eighth edition, 2011.
- [19] E. M. P. Huvener, F. van Herwijnen, F. Soetens, and H. Hofmeyer. Mechanical shear properties of adhesives. In *Glass Performance Days*, pages 367–370, 2007.
- [20] M. W. Hyer and P. C. Bhavani. Suppression of anticlastic curvature in isotropic and composite plates. *International Journal of Solids and Structures*, 20(6):553–570, 1984.
- [21] I. M. Jiménez. *High-strain composites and dual-matrix composite structures*. PhD thesis, California Institute of Technology, 2014.
- [22] M. T. Kikuta. Mechanical properties of candidate materials for morphing wings. Master’s thesis, Department of Mechanical Engineering, Virginia Polytechnic Institute and State University, 2003.
- [23] S. Kota and J. A. Hetrick. United States Patent - 7384016 B2, 2008.
- [24] X. Lachenal, P. M. Weaver, and S. Daynes. Multi-stable composite twisting structure for morphing applications. *Proceedings of the Royal Society A: Mathematical, Physical and Engineering Sciences*, 468:1230–1251, 2012.
- [25] J. Lee, J. Ryu, H. Lee, and M. Cho. Saddle-shaped, bistable morphing panel with shape memory alloy spring actuator. *Smart Materials and Structures*, 23:074013, 2014.
- [26] I. Maqueda, S. Pellegrino, and J. M. Mejia-Ariza. Characterization of a high strain composite material. In *53rd AIAA Structures, Structural Dynamics, and Materials Conference, AIAA*, 2012.
- [27] MatWeb. Aluminum 6061-O. Web Page, 2016. Available from: <http://www.matweb.com/>.
- [28] J. Mejia-Ariza, K. Guidanean, T. W. Murphey, and A. Biskner. Mechanical characterization of l’garde elastomeric resin composite materials. *51st AIAA/ASME/ASCE/AHS/ASC Structures, Structural Dynamics, and Materials Conference*, pages 1–11, 2010.
- [29] B. Mizrahi, C. F. Stefanescu, C. Yang, M. W. Lawlor, D. Ko, R. Langer, and D. S. Kohane. Elasticity and safety of alkoxyethyl cyanoacrylate tissue adhesives. *Acta Biomaterialia*, 7(8):3150–3157, 2011.
- [30] G. Murray, F. Gandhi, and C. Bakis. Flexible matrix composite skins for one-dimensional wing morphing. *Journal of Intelligent Material Systems and Structures*, 21:1771–1781, 2010.
- [31] A. K. Nallathambi, C. Lakshmana Rao, and S. M. Srinivasan. Large deflection of constant curvature cantilever beam under follower load. *International Journal of Mechanical Sciences*, 52(3):440–445, 2010.

- [32] R. R. Naslain. SiC-matrix composites: Nonbrittle ceramics for thermo-structural application. *International Journal of Applied Ceramic Technology*, 2:75–84, 2005.
- [33] G. Norris. Flexsys-built morphing flap tested to higher deflections. *Aviation Week & Space Technology*, pages 27–29, 2015.
- [34] K. R. Olympio and F. Gandhi. Zero- $\nu$  cellular honeycomb flexible skins for one-dimensional wing morphing. *48th AIAA/ASME/ASCE/AHS/ASC Structures, Structural Dynamics and Materials Conference*, 2007.
- [35] A. S. Panesar and P. M. Weaver. Optimisation of blended bistable laminates for a morphing flap. *Composite Structures*, 94(10):3092–3105, 2012.
- [36] Y. C. Pao. Simple bending analysis of laminated plates by large-deflection theory. *Journal of Composite Materials*, 4(3):380–389, 1970.
- [37] R. J. Pomeroy. The effect of anticlastic bending on the curvature of beams. *International Journal of Solids and Structures*, 6(2):277–285, 1970.
- [38] I. S. Raju and J. T. Wang. Classical laminate theory models for woven fabric composites. *Journal of Composites Technology & Research*, 16(4):289–303, 1994.
- [39] M. Sakovsky, I. Maqueda, C. Karl, and S. Pellegrino. Dual-matrix composite wideband antenna structures for cubesats. *AIAA SciTech*, pages 1–26, 2015.
- [40] M. R. Schultz. A concept for airfoil-like active bistable twisting structures. *Journal of Intelligent Material Systems and Structures*, 19:157–169, 2007.
- [41] C. Thill, J. Etches, I. Bond, K. Potter, and P. M. Weaver. Morphing skins. *Aeronautical Journal*, 112(3216):117–139, 2008.
- [42] J. F. Wang, R. H. Wagoner, D. K. Matlock, and F. Barlat. Anticlastic curvature in draw-bend springback. *International Journal of Solids and Structures*, 42(5-6):1287–1307, 2005.
- [43] K. Wong. Laboratory 4: Solving ordinary differential equations with Runge-Kutta methods. pages 1–13, 2009. Available from: <https://www.yumpu.com/en/document/view/8662759/solving-ordinary-differential-equations-with-runge-kutta-methods>.
- [44] T. Yokozeki, S. I. Takeda, T. Ogasawara, and T. Ishikawa. Mechanical properties of corrugated composites for candidate materials of flexible wing structures. *Composites Part A: Applied Science and Manufacturing*, 37:1578–1586, 2006.



# Appendices

## Appendix A

# Fourth-Order Runge-Kutta Numerical Integration

The governing equation derived in Section-4.5.2 can be expressed in the form

$$\ddot{\phi} + \frac{P}{EI} \cos(\phi - \beta - \phi_L) = 0 \quad (\text{A.1})$$

where, as before,  $\beta$  and  $\phi_L$  are constants and  $\ddot{\phi}$  represents the second derivative of  $\phi$  with respect to  $s$ .

A modified form of the fourth-order Runge-Kutta method is employed for the second-order ODE. First define the relations

$$\kappa = \frac{d\phi}{ds} \quad (\text{A.2})$$

and

$$\frac{d\kappa}{ds} = \ddot{\phi} = F(s, \phi). \quad (\text{A.3})$$

Rearranging (A.2) and (A.3) one obtains

$$d\phi = \kappa ds \quad (\text{A.4})$$

and

$$d\kappa = F(s, \phi) ds \quad (\text{A.5})$$

where,

$$F(s, \phi) = -\frac{P}{EI} \cos(\phi(s) + \beta - \phi_L). \quad (\text{A.6})$$

It is also necessary to define two variables,  $d\phi_n$  and  $d\kappa_n$  which are variables necessary to implement the four steps of the RK4 method outlined here. This method is obtained from the work of Wong [43] and manipulated for application to a second-order ODE.

Step 1:

$$\begin{aligned} d\phi_1 &= h\kappa(s) \\ d\kappa_1 &= hF(s, \phi(s)) \end{aligned} \quad (\text{A.7})$$

Step 2:

$$\begin{aligned} d\phi_2 &= h \left( \kappa(s) + \frac{1}{2}d\kappa_1 \right) \\ d\kappa_2 &= hF \left( s + \frac{h}{2}, \phi(s) + \frac{1}{2}d\phi_1 \right) \end{aligned} \tag{A.8}$$

Step 3:

$$\begin{aligned} d\phi_3 &= h \left( \kappa(s) + \frac{1}{2}d\kappa_2 \right) \\ d\kappa_3 &= hF \left( s + \frac{h}{2}, \phi(s) + \frac{1}{2}d\phi_2 \right) \end{aligned} \tag{A.9}$$

Step 4:

$$\begin{aligned} d\phi_4 &= h(\kappa(s) + d\kappa_3) \\ d\kappa_4 &= hF(s + h, \phi(s) + d\phi_3) \end{aligned} \tag{A.10}$$

Finally, the steps are combined using the equations

$$\begin{aligned} d\phi &= \frac{1}{6}(d\phi_1 + 2d\phi_2 + 2d\phi_3 + d\phi_4) \\ d\kappa &= \frac{1}{6}(d\kappa_1 + 2d\kappa_2 + 2d\kappa_3 + d\kappa_4). \end{aligned} \tag{A.11}$$

Now,

$$\begin{aligned} \phi(s + h) &= \phi(s) + d\phi \\ \kappa(s + h) &= \kappa(s) + d\kappa. \end{aligned} \tag{A.12}$$

This process is repeated with the new value of  $s$  until the end of the beam is reached. The value of  $h$  depends on the required accuracy and/or time constraints. For simple problems, a small value for  $h$  provides accurate results without being too time consuming.

## Appendix B

# Test Apparatus Specifications

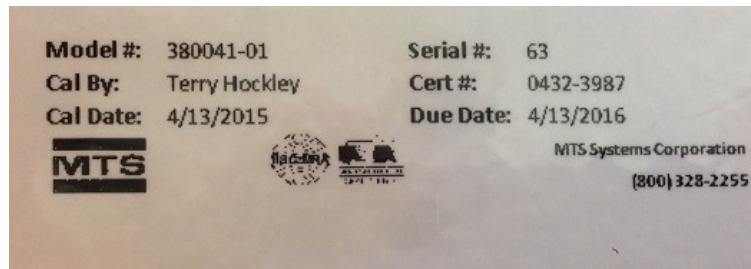


Figure B.1: MTS 880 Material Test System calibration details



Figure B.2: Electronic Instrument Research LE-05 laser extensometer details



Figure B.3: Wyoming Test Fixtures Inc. compression test fixture details